

**Remotely sensed detection and
characterization of agricultural large-scale
land acquisitions in Senegal**

Yasmine NGADI

MSc Thesis



Supervisors

Responsible Professor: Dr. Ir.

Ron van Lammeren

Supervisor: Dr. Ir. Sytze de Bruin

Thesis Defense: July 2020, TUD

ACKNOWLEDGMENTS

I would like to thank my supervisor, Dr Ir. De Bruin, for accepting to supervise this thesis, for providing guidance and feedback throughout this project. I would also deeply thanks V. Lebourgeois and A. Bégué of the UMR TETIS (CIRAD) for their always availability, support, and for providing me with computational and data resources, indispensable to this study. Finally I am very grateful with my family for their huge patience, encouragements and for making this thesis possible.

ABSTRACT

Large-scale land acquisitions (LSLAs) for agricultural sector have grown significantly in the past decade, and are mostly prevalent in developing countries. Because LSLAs are not without negative effects on the environment and local communities, and because information about them is scarce and difficult to obtain, systems allowing LSLAs detection, characterization and monitoring in space and time are needed. With the increasing availability of global satellite data products, technological development in cloud computing, image and data mining analysis, remote sensing has evolved to an interesting tool for the detection and characterization of changes in land use systems.

This study presents a novel approach to generically detect and characterize LSLAs at regional spatial extents. In order to capture and analyse the full range of land use spectral and spatial signatures related to agricultural LSLAs, this study is based on a 2-level data driven approach (Self-Organizing Maps followed by a clustering algorithm), consisting of two phases: 1) land use/land cover change detection at regional scale within dense temporal stacks of vegetation indices (MODIS-NDVI, 250m) and 2), discrimination of different land use/land cover classes using a set of spectral vegetation indices, textural features and shape metrics computed from landscape-extracted objects (Landsat-8, 30m). Evaluation of the methodology is performed against a ground truth database on LSLAs in Senegal.

Results obtained during this exploratory research, are promising and provide some insights in agricultural LSLAs in the northern half of Senegal. With a very limited number of discriminative features (consisting of two Vegetation Indices and two textural features), detection of agricultural LSLAs is possible. Recommendations are given for enhancement of the generalization performance of the unsupervised classifier.

TABLE OF CONTENTS

Acknowledgments	2
Abstract.....	3
Table of Figures	8
List of Tables.....	9
1 Introduction	10
1.1 Research problem.....	10
1.2 Research objective	11
1.2.1 Scope	11
1.2.2 Relevance.....	11
1.2.3 Research objectives and questions.....	11
2 Theoretical background	12
2.1 What are large-scale land acquisitions?	12
2.1.1 Definition.....	12
2.1.2 Agricultural LSLAs spatio-temporal characteristics.....	14
2.2 Remote sensing for land use system monitoring	15
2.2.1 Introduction	15
2.2.2 Satellite Image Time Series (SITS) analysis	16
2.2.3 Image analysis	19
2.2.4 Classification.....	22
2.3 Key findings and opportunities	22
3 Data and methods.....	23
3.1 Study area.....	25
3.2 Regional-scale change detection	25
3.2.1 MODIS NDVI 16-day composite collection 6 data.....	25
3.2.2 Change detection algorithms: BFAST01 and BFAST	26
3.2.3 Selection of a unique breakpoint.....	29
3.2.4 Change map clustering.....	30
3.3 Object-based Landscape analysis approach.....	32
3.3.1 Landsat-8.....	32

3.3.2	Object-based extracted features: vegetation indices, landscape and textural metrics	33
3.3.3	Image segmentation using the Watershed algorithm	35
3.4	Unsupervised classification	38
3.4.1	Input dataset	39
3.4.2	The Self-Organizing Map (SOM)	39
3.4.3	Hierarchical clustering	41
3.5	Evaluation	42
3.5.1	Senegal national ground LSLA database	42
3.5.2	Methods applied for evaluation	43
4	Results	44
4.1	Land use/land cover change detection based on MODIS	44
4.1.1	MODIS NDVI pixels masking using BFAST01	44
4.1.2	BFAST changes detection	46
4.1.3	MODIS-based date of change map segmentation	48
4.1.4	Key findings of the processes including MODIS NDVI change detection and image segmentation	50
4.2	Landscape features extraction based on Landsat8 images	50
4.2.1	Landsat8 images segmentation	50
4.3	Unsupervised classification	52
4.3.1	SOM training	52
4.3.2	SOM hierarchical clustering	54
4.4	Evaluation	55
4.4.1	Inter and intra-cluster variability	55
4.4.2	Accuracy, precision and recall	56
4.4.3	Visual evaluation	58
5	Discussion of results	60
5.1.1	Land use/land cover change detection based on MODIS	60
5.1.2	Landscape features extraction based on Landsat8 images	61
5.1.3	Unsupervised classification	62
5.1.4	Evaluation of the classifiers discriminatory power and insights in agricultural LSLAs	63
5.2	Significance and reflection about the results	64

6	Conclusions and recommendations	65
6.1	Main findings.....	65
6.2	Reference to research questions/objectives.....	66
6.3	Recommendations.....	67
7	References	69
8	Appendices	77
Appendix A	Type of NDVI trend shift experienced.....	77
Appendix B	Unsupervised classifiers: {d.= 0.2, wind.= 5x5, no shape metric}	78
B. 1	Component planes, distance map and clustered SOM.....	78
Appendix C	Unsupervised classifiers: {d=0.2, wind.= 10x10, no shape metric}	79
C. 1	Component planes, distance map and clustered SOM.....	79
Appendix D	Unsupervised classifiers: {dist.= 0.2, wind.= 15x15, no shape metric}	80
D. 1	Component planes, distance map and clustered SOM.....	80
Appendix E	Unsupervised classifiers: {d.=0.6, wind. =5x5, no shape metric}	81
E. 1	Component planes, distance map and clustered SOM.....	81
Appendix F	Unsupervised classifiers: {dist.=0.6, wind. =10x10, no shape metric}	82
F. 1	Component planes, distance map and clustered SOM.....	82
Appendix G	Unsupervised classifiers: {d.=0.6, wind. =15x15, no shape metric}	83
G. 1	Component planes, distance map and clustered SOM.....	83
Appendix H	Unsupervised classifiers: {d.=0.2, wind. =5x5, shape metric}.....	84
H. 1	Component planes, distance map and clustered SOM.....	84
Appendix I	Unsupervised classifiers: {d.=0.2, wind. =10x10, shape metric}.....	85
I. 1	Component planes, distance map and clustered SOM.....	85
Appendix J	Unsupervised classifiers: {d.=0.2, wind. =15x15, shape metric}.....	86
J. 1	Component planes, distance map and clustered SOM.....	86
Appendix K	Unsupervised classifiers: {d.=0.6, wind. =5x5, shape metric}.....	87
K. 1	Component planes, distance map and clustered SOM.....	87
Appendix L	Unsupervised classifiers: {d.=0.6, wind.=10x10, shape metric}.....	88
L. 1	Component planes, distance map and clustered SOM.....	88
Appendix M	Unsupervised classifiers: {d.=0.6, wind. =15x15, shape metric}.....	89
M. 1	Component planes, distance map and clustered SOM.....	89

TABLE OF FIGURES

Figure 1: Cropping land use system components	14
Figure 2: Flowchart of the methodology.....	24
Figure 3: BFAST01 and BFAST detected breakpoints in MODIS 2000-2018 NDVI time series	28
Figure 4: BFAST breakpoints detection within MODIS 2000-2018 NDVI time series.....	30
Figure 5: Delimitation of MODIS date of change map clusters edges.....	31
Figure 6: Example of input Landsat 8 images used for the segmentation process.....	37
Figure 7: Image segmentation process steps applied on Landsat 8 images.	38
Figure 8: Self-Organizing Map (SOM) training process.....	40
Figure 9: Date of change map as detected by BFAST01	45
Figure 10: BFAST date of change map for the northern half of Senegal	47
Figure 11: Closer views on the BFAST date of change map (Northern Senegal).....	47
Figure 12: Delineation of MODIS date of change map clusters and map segmentation	49
Figure 13: Example of extracted landscape objects from Landsat 8 images	51
Figure 14: Illustration of the SOM maps.....	53
Figure 15: Plot of the Silhouette average values for different SOM partitions ($k = \{2, 3, \dots, 20\}$).....	54
Figure 16: Clustered SOM.....	55
Figure 17: Clustered SOM Silhouette analysis.....	56
Figure 18: Distribution (%) of the classified Landsat object (raster)	58
Figure 19: Closer views to different Landsat 8 classified objects	59

LIST OF TABLES

Table 1: Estimate farm sizes of selected regions of the world	13
Table 2: Statistics on LSLAs in ISRA/CIRAD database.....	42
Table 3: Number of potentially detectable LSLAs.....	46
Table 4: Spatial statistics on the clusters extracted from the MODIS-based date of change map	49
Table 5: SOMs parameter settings	52
Table 6: Unsupervised classifiers overall performance	57

1 INTRODUCTION

1.1 RESEARCH PROBLEM

Large scale land acquisitions (LSLAs), often referred as “land grabbing”, refers to the purchase, lease, concession, or occupation of large pieces of land by individuals, states or companies (domestic or foreign) for agricultural purposes (food crop, fodder crop, biofuel), logging, tourism, conservation, mining, urban expansion or large infrastructural works (Batterbury et al., 2018; Kaag et al., 2014). This study deals with agricultural LSLAs, the most common type of LSLAs, principally driven by the food crisis and the demand for biofuels. Given the availability of favourable biophysical resources and the lack of strong land tenure regulations, those large-scale land investments are mostly prevalent in developing countries, with almost 75% of LSLAs located in the sub Saharan Africa (representing around 50 million hectares) (Batterbury et al., 2018; Kaag et al., 2014; Messerli et al., 2014; Osabuohien, 2014; Sparks, 2012). Because land grabbing is not without negative effects on the environment and local communities, and because information about them is scarce and difficult to obtain, (Batterbury et al., 2018; Kaag et al., 2014), systems allowing LSLAs detection, characterization and monitoring in space and time (installation, abandonment, etc.) are needed.

With the increasing availability of global satellite data products, technological development in cloud computing, image and data mining analysis, remote sensing has evolved to an interesting tool for the detection and characterization of changes in land use systems. Its repetitive coverage at short intervals and consistent image quality, combined with the free-of-cost availability of dense temporal series of satellite images (SITS), have explained their wide use in land use and land cover (LULC) change detection studies (Arvor et al., 2012; Leroux et al., 2017; Wardlow et al., 2007). Land use systems such as LSLAs are however more difficult to detect. Because (agricultural) LSLAs are the manifestation of complex human-environment dynamics in a given place, they are not directly observable from remote sensing images (Kuemmerle et al., 2013). While their detection is often impossible based on land cover observations only (there is no one-to-one relation between land cover and functionality), these land use systems may however be inferred from observable activities, structural elements in the landscape (e.g. presence of pivot irrigation systems) or spatio-temporal characteristics at different scales (Hentze et al., 2017; Jain et al., 2013; Steeg et al., 2010; Verburg et al., 2009).

This research aims to explore the potential of remote sensing data to detect and characterize agricultural LSLAs at different scales. The challenge here is to relate the radiometric signal (value, spatial pattern and dynamic), which is sensitive to the biophysical properties of the surface, to the land use system in place. In this research, remote sensing indicators and methods are reviewed and a conceptual approach is proposed and tested on a set of study sites in Senegal.

1.2 RESEARCH OBJECTIVE

1.2.1 Scope

Because most of the studies attempting to map cropland fields have relied on site-specific predefined ground truth data, there is a current need of developing generic and unsupervised approaches not to only map cropland fields, but also to detect land use system changes (Bey et al., 2020; Graesser et al., 2017; Stefanski et al., 2014; Timmermans, 2018; Watkins et al., 2019b; Yan et al., 2014).

This study builds on a previous exploratory study, performed in partnership in ISRA and CIRAD, which tested two time series change detection algorithms (namely BFAST01 and BFAST) in their ability to automatically detect agricultural LSLAs in Senegal (Ngadi, 2020). While both algorithms have proven their ability in detecting abrupt changes related to agricultural LSLAs' installation, they differ in their precision and computational efficiency. More specifically, the difference between both algorithms lies in the regression model applied and in the number of breakpoints found. While BFAST relies on a season-trend model and finds the optimum number of breakpoints that minimizes the residual sum of squares of the regression model, BFAST01 does not perform any season-trend decomposition and selects the best linear model between a model with 0 and a model assuming a single breakpoint. The latter makes BFAST01 almost ten times faster than BFAST, which is hardly applicable at regional scales. However, the drawback with BFAST01 is that because it detects only one breakpoint (the strongest one), it is not always related to anthropogenic changes but may also be related to climatological events, leading to 'false positives'. That is why much work has still to be done in order to implement an effective approach based on change detection algorithms, to automatically detect LSLAs.

This thesis aims to fill the gap by exploiting the best of both algorithms in their ability to detect agricultural LSLAs. Both algorithms will be used in combination with an object-based image analysis and unsupervised classifier in order to detect and characterize agricultural LSLAs.

1.2.2 Relevance

The importance of this topic is twofold:

- 1- As the ability of developing countries to reduce poverty and hunger is strongly linked to agriculture, the quantification and monitoring of phenomenon such as LSLA is particularly important due to the various impacts it has on local communities.
- 2- In the context of Global Changes and with the increasing availability of remote sensing data at different spatial and temporal resolutions, the development of an automatic approach to detect and monitor on a near-real time basis LULC changes is highly needed.

1.2.3 Research objectives and questions

This thesis **aims to explore the potential of remote sensing data to detect and characterize agricultural LSLAs at different scales**. This goal is subdivided into the two sub-objectives below:

Sub-objective 1: Detect potential agricultural LSLAs' installation automatically at regional scale using change detection algorithms and medium resolution satellite (MODIS 250m) temporal series

- RQ 1.1: Which method allows discriminating climate-induced breakpoints in MODIS NDVI time series from “anthropogenic” ones?

Sub-objective 2: Discriminate detected potential agricultural LSLAs from other spatial processes (e.g.: agglomerated smallholder farms, LSLAs for conservation purposes...) using higher resolution satellite imagery (Landsat 8)

- RQ 2.1: Which spatio-temporal characteristics of agricultural LSLAs are transferrable to indicators and spatial metrics that can be derived from satellite imagery?
- RQ 2.2: Do the metrics of question 2.1 allow distinction between different type of agricultural LSLAs and environments?
- RQ 2.3: Is the proposed methodology suitable for automatically discriminate agricultural LSLAs at regional scale?

2 THEORETICAL BACKGROUND

2.1 WHAT ARE LARGE-SCALE LAND ACQUISITIONS?

2.1.1 Definition

Large scale land acquisitions (LSLAs), often referred as “land grabbing”, refers to the purchase, lease, concession, or occupation of large pieces of land by individuals, states or companies (domestic or foreign) for agricultural purposes (food crop, fodder crop, biofuel), logging, tourism, conservation, mining, urban expansion or large infrastructural works (Batterbury et al., 2018; Kaag et al., 2014). If we consider the negative effects that LSLAs often have on the environment and local communities (Batterbury et al., 2018; Kaag et al., 2014), a broader definition would be the one suggested by Baker-Smith & Attila (2016), who defined land grabbing as: “[...] the control (whether through ownership, lease, concession, contracts, quotas, or general power) of larger than locally-typical amounts of land by any person or entity (public or private, foreign or domestic) via any means (‘legal’ or ‘illegal’) for purposes of speculation, extraction, resource control or commodification at the expense of peasant farmers, agroecology, land stewardship, food sovereignty and human rights.”. The reported negative effects, added to the often lack of centralized, digital and up-to-date records within governments, explain the lack of transparency surrounding most of the deals (even if largely legal). This lack of transparency combined to the speed and scale of the expansion seen during this last decade, make monitoring and quantification of LSLAs a very difficult task, which is illustrated by discrepancies between published numbers (Baker-Smith et al., 2016; Batterbury et al., 2018; Schoneveld, 2011). As an example, while Oxfam (2011) estimated the land under

acquisition in Africa to about 34 million hectares, the Oakland Institute in 2009 alone estimated it to about 60 million (Batterbury et al., 2018). In any event, even if no one knows exactly how much land is involved, it can be taken for granted that the area involved is huge and growing (Kaag et al., 2014; Lazarus, 2014).

This study deals with agricultural LSLAs, the most common type of LSLAs, which are principally driven by the food crisis and the demand for biofuels. According to Oxfam (2011), 37% of total LSLAs would be dedicated to food production, while 35% would be dedicated to crop production for biofuel (Kaag et al., 2014). Given the availability of favourable biophysical resources and the lack of strong land tenure regulations, those investments are mostly prevalent in developed countries (Batterbury et al., 2018; Kaag et al., 2014; Messerli et al., 2014; Osabuohien, 2014; Sparks, 2012). More precisely, almost 75% of LSLAs would be located in the sub Saharan Africa (representing around 50 million hectares) (Sparks, 2012).

Agricultural LSLAs have been defined as the “taking possession of and/or controlling a scale of land for commercial/industrial agricultural production that is disproportionate in size in comparison to the average land holding in a region” (FIAN, 2010). While the FAO suggested LSLAs involve more than 1000 ha in a single deal (Batterbury et al., 2018), other authors as FIAN (2010) or Baker-Smith & Attila (2016) suggested to take into account the average land holding in the region (see **Table 1**). As an example, in Africa where 69 % of farms are smaller than 2 ha, a land deal above 5 hectares may already be considered as an agricultural LSLA (Bey et al., 2020). In European countries such as Romania, land investments are considered as LSLAs when the area contracted is equal or above 50 ha, as farms exceeding 50 ha represent less than 1% of the total national holdings (Baker-Smith et al., 2016). Most single land deals however, involve several hundred or a few thousand hectares at a time, with some exceptions that encompass areas that are several orders of magnitude larger (Cotula, 2012). It is interesting to note that besides single land acquisitions, LSLA may also take form of a conglomerate of smaller acquisitions involving various actors (Kaag et al., 2014).

Table 1: Estimate farm sizes of selected regions of the world (source: Debats et al. 2016)

World region	Average farm size (hectares)
Africa	1.6
Asia	1.6
Western Europe	27.0
Latin America and Caribbean	67.0
North America	121.0

Agricultural LSLAs are not directly observable from remote sensing images. In order to detect and analyse agricultural LSLAs by remote sensing, agricultural LSLAs’ spatio-temporal characteristics need to be determined first.

2.1.2 Agricultural LSLAs spatio-temporal characteristics

Agricultural LSLAs, as any agricultural land use systems (ALUS), are spatially and temporally described by three components: crop succession (crop rotation and fallowing), cropping pattern (single tree crop planting pattern, sequential cropping, and intercropping/agroforestry), and cropping techniques (irrigation, soil tillage, harvest and post-harvest practices, crop varieties, and agro-ecological infrastructures) (Bégué et al., 2018; see figure 1).

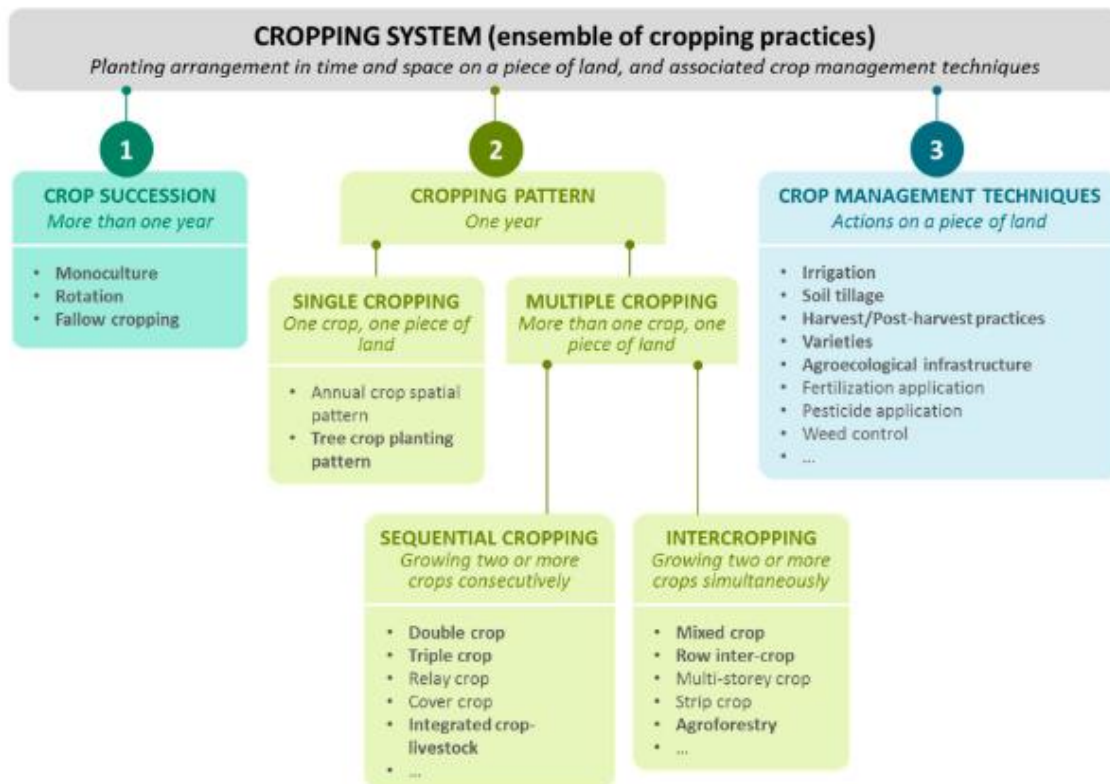


Figure 1: Cropping land use system components (Source: Bégué et al. 2018)

As one can see in **figure 1**, ALUS encompass a wide variety of spatial and temporal patterns. However, most agricultural LSLAs share some typical characteristics.

Firstly, agricultural LSLAs are highly dynamic land use systems, **characterized by rapid transformations at vast spatial scales**, with frequent changes occurring in their operational status (planned, started, cancelled, etc.), areal extent (implementations usually begin on a smaller scale than the one under contract) and usage (Cotula, 2012; Kaag et al., 2014; Lazarus, 2014; Messerli et al., 2014). As a consequence, any technique **able to detect land cover abrupt changes, occurring fast at vast spatial scales**, may work as a first filter to detect agricultural LSLAs installations at large spatial scales.

Small and large-scale agriculture do not only differ in terms of area of land cultivated but also in terms of agricultural intensification. While smallholder agriculture often relies on family labour, surface water and rainwater, and low levels of inputs (land area, technology,

mechanization, agrochemicals...), large-scale agriculture tends to use high levels of the same inputs leading to the practice of an **intensive agriculture** (Debats et al., 2016; Kuemmerle et al., 2013; Ozdogan et al., 2010; Stefanski et al., 2014). Agricultural LSLAs often involve investment in irrigation and monoculture crops which dominate most land under acquisition (Batterbury et al., 2018). As a result, irrigated fields are not scattered across the landscape but they are very often located close to water resources such as rivers, ponds, reservoirs or lakes (Vogels et al., 2019a). A recent survey of 220 investors in Mozambique revealed that 83% involved some form of mechanization, 90% applied agricultural inputs and 52% were fully irrigated (Bey et al., 2020). In comparison, at the African scale where most of the farmers are smallholder farmers, only 6.4% of the total cultivated areas are under irrigation (Frenken, 2005). In addition, agricultural LSLAs generally involve fertile soils, in low-density areas with sufficient or good irrigation potential, preferably with good road access. With the saturation of fertile soils and the technological advances, more marginal and vulnerable areas are also being targeted. Methodologies able to quantify land use intensity may then be helpful in detecting agricultural LSLAs at regional/local scales.

As aforementioned, smallholder and large-scale agriculture differ in the degree of mechanization applied, which lead to spatial differences. As a result of the low degree of mechanization, smallholder agriculture usually produce multiple crop types (by intercropping or by mixed cropping) (Vogels et al., 2019a), leading to complex and fragmented landscapes (Debats et al., 2016). Large-scale agriculture at the opposite, produce less fragmented landscapes, with more “geometrical” and homogeneous spatial patterns. As a consequence, methodologies able to compute landscape metrics at higher spatial resolution may then be useful to discriminate agricultural LSLAs from smallholder agriculture.

In conclusion, detection and characterization of agricultural LSLAs may benefit from combinations of one or more methodologies capable of 1) detecting land cover/land use changes, 2) quantifying crop field-sizes and qualifying land use patterns, and 3) quantifying agriculture intensity. A review of the most commonly remote-sensing analysis techniques applied to land use and land cover (LULC) studies, with key related works aiming to characterize and monitor agricultural land use systems, is presented in the next section.

2.2 REMOTE SENSING FOR LAND USE SYSTEM MONITORING

2.2.1 Introduction

The increasing scale, pace, and intensity of climatic and anthropogenic environmental transformations, enhance the need of **land use system mapping at different scales** (Bégué et al., 2015; Brown et al., 2007; Wardlow et al., 2007). While land cover addresses the description of the land surface in terms of soil and vegetation layers, land use system (LUS), such as the one represented by LSLA, is defined as a coupled human-environment system in which land use and land management are described in time and space (Bégué et al., 2015; Kuemmerle et al., 2013). Timely and consistent monitoring of land use systems at different scales is needed

to better understand the role and response of regional practices in relation to various environmental issues, and for better decisions with respect to food security.

Even though land cover changes over time such as deforestation due to agricultural expansion have been widely studied (Graesser et al., 2018), progress has been less rapid in monitoring land use systems such as LSLAs. According to Bégué et al. (2018), less than 10% on the publications of remote sensing and agriculture focus on cropping systems. Furthermore, high variability in agricultural practices (see **figure 1**)/environmental conditions (reflected in spectral response and spatial patterns), explains why most of the studies are performed at local scales. Due to this wide range of heterogeneity, ALUS are usually inferred from observable activities, such as structural elements in the landscape (e.g. presence of pivot irrigation systems) and spatio-temporal characteristics at different scales. Still, because of their complexity, methodological approaches often rely on local knowledge for interpretation, time and cost-expensive ground-based data and models (Debats et al., 2016; Hentze et al., 2017; Jain et al., 2013; Steeg et al., 2010; Stefanski et al., 2014; Verburg et al., 2009).

As mentioned above, remote sensing provides crucial spectral and spatio-temporal information on LULC in the form of ever-increasing satellite image time series (SITS) and images. Different analysis techniques allowing extraction of unique vegetation phenological (seasonal vegetation variation) profiles, detection of abrupt/gradual changes and characterization of landscape elements arrangement are needed in order to discriminate ALUS types. Some of these techniques are presented in the next two sub-sections of section 2.2. While sub-section 2.2.2 is dedicated to SITS analysis, sub-section 2.2.3 focuses on image analysis. The last sub-section is dedicated to image classification techniques allowing to classify pixels or groups of pixels (objects) into different thematic classes. Because this thesis aims to rely as less as possible on supervised techniques needing often local-specific ground truth data, sub-section 2.2.4 focus on unsupervised classification techniques.

2.2.2 Satellite Image Time Series (SITS) analysis

a) Agricultural land use system characterization

The study of vegetation indices (VIs) temporal dynamics allow monitoring of the seasonal vegetation variation (phenology). The latter, combined with expert knowledge of the local to regional agricultural practices, has allowed to identify major agricultural land use system (ALUS) types and some agricultural land use practices such as: harvesting, irrigation (rainfed vs irrigated crops), multiple cropping, and fallowing frequency (Bégué et al., 2018; Bellón et al., 2017; Chen et al., 2018b; Kuemmerle et al., 2013; Wardlow et al., 2007). SITS have recently been useful in quantifying land use intensity, which is of particular interest to this study.

Land use intensity mapping is challenging. As highlighted by Kuemmerle et al. (2013), land use intensity is a complex and multidimensional phenomenon, not directly observed through remote sensing. Cropping intensity, defined as the number of crops per year in a unit cropland area, is one of the major factors of agriculture intensification. While studies on vegetation or productivity trend alone are not enough to detect land use intensity, methodologies based on crop phenologies extracted from high temporal-resolution datasets like MODIS, give good

results on large crop fields, with individual farm plots spanning ten to fifteen MODIS pixels (Jain et al., 2013). Among the different studies attempting to characterize agricultural land use, studies aiming to detect irrigated agriculture are gaining popularity (Hentze et al., 2017; Ozdogan et al., 2010; Vogels et al., 2019a; b). Irrigated fields are usually more productive and active than rainfed agriculture, leading to differences in biomass and greenness remotely-sensed indices. In order to identify irrigated agriculture, methods mostly rely on temporal profiles and multi-temporal features of spectral indices (range, maximum...) in the visible, near-infrared bands and derived spectral features (NDVI being the most common), but also on SAR and metrics about the geometry and topology of croplands (Li et al., 2016; Vogels et al., 2019; Vogels et al., 2019). This is how, based on MODIS NDVI time series analysis and a change detection algorithm (BFAST), Hentze et al. (2017) were able to identify changes in cropping patterns (from/to irrigated farming) in Zimbabwe after a land reform. In addition to NDVI, different studies recommend the use of irrigation indices such as the NGI (Normalized Green Index) and the EGI (Excess Greenness Index), derived from the Greenness Index (GI), the Evaporative Fraction (ETRF) and the NDVI, in irrigation assessment (Ozdogan et al., 2010; Pun, 2019). Others such as Thenkabail et al. (2007) showed that some MODIS original spectral bands, especially band 5 (1240 nm) provided a good degree of discrimination between rainfed and irrigated areas (Bégué et al., 2018). Because separation of multiple vegetation types and spectral patterns at a regional scale is challenging, most of the studies have been conducted at local scale. However, coarse-spatial resolution satellite imagery (i.e. NOAA-AVHRR 1.1 km, SPOT-VGT 1.15km) with daily temporal resolutions, and medium-spatial resolution such as MODIS 250m are commonly used to characterize cropping systems in agricultural areas with relatively large fields (Bégué et al., 2018; Vintrou et al., 2012b; Wardlow et al., 2007).

Among the analysis techniques commonly applied to SITS, one can find Fourier harmonic analysis useful in identifying frequencies in time series from which multiple (sequential) cropping is inferred, fast Fourier transformation (FFT), wavelet techniques (Galford et al., 2008), principal component analysis (Bellón et al., 2017), change detection analysis and decision trees (Thenkabail et al., 2007). Techniques such as Fourier or wavelet analysis provide a new representation of image time series but are based on a dimension reduction which implies a loss of information (Bégué et al., 2018). To address this issue, new techniques based on shape matching (e.g. Dynamic Time Warping approaches with temporal weights) are being used. While successful, results are less satisfactory in highly fragmented and mixed cropping systems (Thenkabail et al., 2007).

b) LULC trends and change detection

In addition to land surface characterization, SITS have also been used to detect, estimate and characterize land surface changes and their drivers, which may be useful in detecting agricultural LSLAs installation. Changes in SITS may be gradual or abrupt, and may happen in the trend and/or seasonal component of the time series.

While the trend component represents long-term changes in the time series signal, the seasonal factor relates to the periodic fluctuations of constant length (Almeida, 2017). Changes observed within a time series may therefore be a combination of seasonal and trend changes,

which need to be differentiated from noise that originates from remnant geometric errors, atmospheric scatter and cloud effects (Verbesselt et al., 2010a). It is commonly accepted that gradual trend changes are related to inter-annual climate variability and other processes such as land management or land degradation, while abrupt trend changes indicate ecosystem disturbances such as deforestation, urbanization, floods or fires (Verbesselt et al., 2010a). In contrast, changes in the seasonal component are driven by annual climatic interactions (Verbesselt et al., 2010b). In western Sahel, where precipitation is very often the constraining factor on vegetation productivity, seasonal changes are mostly driven by rainfall variability. Because seasonal variations may mask underlying trend changes, seasonal variation in complete temporal series need to be accounted for.

During the last decades, studies attempting to detect and estimate VIs trend changes have mostly applied linear regression analysis on annual aggregated time series. The temporal aggregation has been found to be useful in minimizing lag effects (as the growing season may be shifted by 1 or 2 months between different regions, time series temporal aggregations over periods longer than the growing season ensure to take into consideration the whole growing season), minimizing the seasonal cycle from temporal series, and remediating serial autocorrelation (De Jong et al., 2012; Forkel et al., 2013). For that, different techniques have been used, such as: the use of specific periods within a year (e.g. growing season), the temporal aggregation of time series data, and the normalization of reflectance values per land cover type (Verbesselt et al., 2010a). Correlation of VIs with different factors (climate, anthropogenic...) is then usually performed to identify major LUCC drivers (Leroux et al., 2017; Liu et al., 2015). In that respect, a simple and widely used approach is the RESTREND (RESidual and TREND) analysis which analyses the residuals obtained from the linear regression between the vegetation index and one climatic variable over time (Evans et al., 2004). While shown to be effective, this technique requires the existence of a stable linear regression over the time series being analysed, with no changes in the directionality of the trend in the residuals (Angel et al., 2018; De Jong et al., 2012; Jamali et al., 2014; Wessels et al., 2012). Because such precondition is unlikely to be fulfilled with the ever-increasing length of SITS analysed, methodologies that include structural change detection (presence of breakpoints, i.e. unusual shifts in time series) are needed in order to prevent unreliable results. In addition, because the temporal resolution and time series length are critical in determining the significance of the trend in a statistical test, methodologies that make use of the full temporal resolution time series are preferred over those one performing temporal aggregation (Forkel et al., 2013). This is how different change detection algorithms (e.g. BFAST, BAST01, DBEST (Jamali et al., 2015; Verbesselt et al., 2012)) have been developed and successfully applied in different research context, allowing to detect: vegetation dynamics in Quebec (Fang et al., 2018), clear-cuts and decreases in forest vitality in an area in the south of France (Lambert et al., 2015), drivers of environmental changes in drylands of north-western Ethiopia (Zewdie et al., 2017) and changes in agricultural practices (changes from irrigated agricultural to non-irrigated agricultural land) of different tenure regimes in Zimbabwe (Hentze et al., 2017). Recently, BFAST01 and BFAST (Verbesselt et al., 2010a, 2012) have been tested in an exploratory study attempting to automatically detect LSLAs in Senegal (Ngadi, 2020).

While both algorithms proved their ability in detecting abrupt changes related to agricultural LSLAs' installation (but not only), they differ in their precision and computational efficiency. More specifically, the difference between both algorithms lies in the regression model applied and in the number of breakpoints found. Both algorithms rely on the assessment of deviations from the classic linear regression model. More details can be found in subsection 3.2.2.1.

2.2.3 Image analysis

Because spectral properties of vegetation are not unique to different agricultural land use systems, object-based image analysis has shown to be complementary to the classical temporal pixel-spectra based analysis (Bellón et al., 2017; Bisquert et al., 2015; Lebourgeois et al., 2017). Object-based Image Analysis (OBIA) differ from pixel-based approaches in that they operate on many pixels grouped together in homogeneous objects by image segmentation, allowing to exploit the spatial relationship of data. By accessing objects features, additional information such as spectral descriptive statistics (mean, variance, percentiles, etc.) per bands, or spatial and morphological metrics may be used. OBIA uses information on colour, tone, texture, pattern, shape, shadow, context and size (i.e. structural parameters) to classify the images (Blaschke et al., 2014).

OBIA or GEographic OBIA (GEOBIA, which relies on remote sensing data and generates GIS (Geographic Information Systems)) typically includes image segmentation, edge detection, feature extraction, classification, and change detection (Blaschke, 2010; Hay et al., 2010; Petitjean et al., 2012). The object-based classification approach works well for structured landscapes with high geometric and contextual properties and low heterogeneity inside the objects, as is the case of agricultural LSLAs. This is how the combination of spectral and structural parameters (shape, texture, neighbour) have shown to yield valuable information to map irrigated agriculture (Ozdogan et al., 2010). While mostly applied to high-resolution satellite imagery, few studies have applied this technique on coarse-resolution satellite images (MODIS) in order to map ALUS at regional scale (Bellón et al., 2017; Bisquert et al., 2015).

a) Image segmentation

GEOBIA segmentation techniques seem particularly suitable to the extraction of homogeneous (in terms of spectral and textural information) ALUS types (Bellón et al., 2017; Bisquert et al., 2015). Because object-based methodologies depend strongly on the objects (segments) obtained through segmentation, this process of segmenting an image is a crucial one. As defined by Chen et al. (2018) "Image segmentation is the process of partitioning a digital image into multiple regions (sets of pixels); the pixels in each region have similar attributes. It is often used to separate an image into regions in terms of surfaces, objects, and scenes, especially for object location and boundary extraction." (Chen et al., 2018a).

However, segmentation is an ill-posed problem: there is no unique solution (Hay et al., 2010). Typically, object-based classifiers first over-segment a scene by applying a multi-scale or hierarchical iterative segmentation algorithm. Using a homogeneity criterion, multiple segments are then obtained, in one or more dimensions of the feature space. Compared to single pixels, these segments have additional spectral information (descriptive statistics that

are computed for each segment), but also additional spatial information (Blaschke, 2010). After over-segmentation, the next steps consist in grouping the different segments to a same object following a set of rules, and then label the objects using different approaches (Vintrou et al., 2012a; Yan et al., 2014). Segmentation is still challenging as satellite images contain regions with different texture, varying background and they are often subject to illumination changes or environmental effects (Jabar et al., 2019).

Segmentation techniques are generally divided into 4 classes: point-detection based, edge-detection based, region-detection based and combined (Blaschke, 2010). Commonly used techniques are edge-based and region-based methods. Edge-based methods rely on filters (Sobel and Canny are common examples) to identify discontinuities in images where pixel values change rapidly. Frequent issues are their sensitivity to high-frequency noise which often creates false edges; and their need of context-specific parametrization which, when not optimal, lead to open boundaries. Because of the latter, post-processing and locally-adapted thresholds are applied (Waldner et al., 2019). Region-based algorithms (watershed, region growing, etc.) group neighbouring pixels into objects based on some homogeneity criterion. Compared to edge-based methods, region-based algorithms tend to over-segment fields with high internal variability and under-segment small adjacent fields. In addition, sub-optimal (non- context specific) parametrization may yield to boundary errors (Waldner et al., 2019). Because of the weaknesses of both algorithms, hybrid methods have been proposed (Watkins et al., 2019b).

When applied to agricultural land use changes detection, segmentation techniques have been particularly useful in delineating crop-fields boundaries. Field boundaries extraction is useful to discriminate smallholder agriculture from large-scale agriculture, as field size may be used as a proxy of the degree of mechanization (Stefanski et al., 2014). While their identification in high spatial-resolution images (<10m) can be straightforward when undertaken visually, automation over large areas is challenging. Firstly, traditional per-pixel based methods are not suitable for understanding land use system/landscape patterns (Graesser et al., 2017). Secondly, because at high resolution land cover classes have lower inter-class and higher intra-class spectral variability (Debats et al., 2016), automatic identification of highly variable (spatially and spectrally) agriculture land use systems is difficult. Finally, because upscaling to large extents is usually impractical due the vast amount of data needed, studies have mostly been performed at local to regional scales (Gillanders et al., 2008).

Studies delineating field boundaries based on remote sensing data often include combinations of semi-automated image-processing techniques (e.g. image morphology, edge detection-based segmentation, region detection-based segmentation etc.) and predefined vector data or texture measures (Bey et al., 2020; Debats et al., 2016; Graesser et al., 2018, 2017; Lesiv et al., 2019; Stefanski et al., 2014; Watkins et al., 2019b; Yan et al., 2014). Accurate detection of agricultural boundaries is affected by field size, shape, configuration, and crop type (Graesser et al., 2017). When neighbouring crop fields are of the same species, or are less visually defined (indistinct boundaries between fields, ambiguity with natural vegetation as it often happens with smallholder fields), separation between large-scale agriculture and

smallholder agriculture results very difficult (Debats et al., 2016; Graesser et al., 2017). One way to overcome this limitation is the inclusion of multi-temporal data, which allows to take advantage of the often differentiated phenological profiles between vegetation (Debats et al., 2016; Lebourgeois et al., 2017; Watkins et al., 2019b). Multi-temporal data may take the form of images pairs : one or many in the growing season (Debats et al., 2016; Watkins et al., 2019a), or take the form of different multi-spectral temporal composites (Bey et al., 2020; Graesser et al., 2017), or be the full temporal series (Hentze et al., 2017).

b) Landscape and textural metrics

Landscape metrics refer to indices that quantify the composition and spatial arrangement of elements across a landscape. They are used at patch, class/patch type, and landscape levels (McGarigal, 2001). While some of those metrics quantify the landscape composition (e.g., the relative abundance of classes), others quantify the landscape configuration such as: the position, connectivity of patches types (Bégué et al., 2018). As ALUS heavily impact landscape spatial patterns and create a mosaic of patches, methods that consider the spatial context of pixels and provides information about the landscape's structure and morphology are interesting. For example, Hietala-Koivu (1999) used landscape percentage, mean patch size, patch density, mean shape index and total edge length to differentiate between homogeneous and heterogeneous landscapes (Gillanders et al., 2008). Used in combination with vegetation indices, landscape metrics have allowed to achieve high classification accuracies (Bey et al., 2020; Kuemmerle et al., 2009; Lebourgeois et al., 2017; Vintrou et al., 2012b).

In addition to contextual and spectral features, textural features are also fundamental in image interpretation. Textures have been used in different land use/land cover classification studies in order to improve the accuracy of classification (Kupidura, 2019). While spectral features describe the average tonal variations in various spectral bands, textural features carry information about the spatial distribution of tonal variations of a contiguous set of pixels in a local neighbourhood of an image (Haralick et al., 1973). These features allow to quantify spatial information, and have recently been successfully used in the classification of agricultural lands. In a very recent study, Bey et al. (2020) detected changes between smallholder farms and large-scale farms in Mozambique relying on Landsat-derived textural features. Similarly, Vogels et al. (2019) found that textural variables were the most important ones in discriminating smallholder agriculture from large-scale agriculture in Ethiopia using very high resolution satellite imagery (SPOT6).

More specifically, structural indicators use information on colour, tone, texture, pattern, shape, shadow, context and size (Blaschke et al., 2014). Commonly used indicators are derived from the co-occurrence matrix, auto-correlograms, Markov random fields or frequential analysis (Bégué et al., 2018). While most of the studies used high ($\leq 10\text{m}$) spatial resolution satellite imagery, some have shown that even medium spatial resolution imagery (MODIS) contains textural information useful for crop mapping (Bégué et al., 2015).

2.2.4 Classification

The second step of a GEOBIA consists in the classification of the individual objects extracted through segmentation into thematic classes. Classification of agricultural land use systems at regional to global scales is particularly challenging due to the high intra-class variability driven by regional climatic and environmental differences (Bégué et al., 2018). Classification (object-based, as well as pixel-based) may be supervised or unsupervised, depending on available data and knowledge about the study area. So far, most of the existing classifiers used to discriminate LULC types are supervised (Graesser et al., 2018; Ragettli et al., 2018; Vintrou et al., 2012a). While successful, those classifiers require expert interaction, detailed reference land cover layers, large number of sample training sites, or empirical look-up tables which are often expensive to obtain. In addition, because training data is often site-specific, supervised classifiers are often hardly transferred to large areas (Debats et al., 2016). Some popular supervised parametric algorithms are the Maximum Likelihood Classifier (MLC) and linear Support Vector Machine (SVM). Because of their robustness to outliers and noise, as well as their ability to handle extremely large feature spaces, non-parametric (no assumption is made about the data frequency distribution) classifiers are preferred (Debats et al., 2016). Some popular supervised non-parametric algorithms are Radial Basis Function networks (RBF), nonlinear Support Vector Machines (SVM) and Random Forest (RF)

Unsupervised classifiers (also known as clustering algorithms) are on another hand used to detect groups of pixels or objects sharing similar features based on their spectral and/or spatial information, without the need of any a priori knowledge. Those classifiers are typically used for exploratory data analysis over large areas, in order to capture and analyse the full range of land use signatures (spectral and spatial) of the data. They however require the selection of a number of clusters and a posteriori labelling, which may be hard when used to classify heterogeneous landscapes. In addition, the resulting classification rarely shows a one-to-one relationship with classes derived from ground-truth data (Lathrop et al. 2006; Brown et al. 2012). However, with the fast development in data storage, data mining and remote sensing technologies, studies are opting for unsupervised machine learning techniques to automatically extract field sizes from very high-resolution images. Yan and Roy (2014) developed for the United States a fully automatic methodology using image-processing techniques such as image morphology and segmentation on Landsat imagery. While good results were achieved without the need of third-party data or human intervention, the methodology relied on: large field sizes with a relatively precise geometry (square or round, with well-defined boundaries), static crop field boundaries within the time series acquisition period (5 years), crop fields with a high amplitude NDVI phenology, pixels with consistently high seasonal NDVI (in order to detect cropland from other land covers).

2.3 KEY FINDINGS AND OPPORTUNITIES

Key findings can be drawn from this chapter:

- Combined with an Object-Based Image Analysis (OBIA) approach, multi-temporal Sentinel-2 and Landsat are suitable for individual crop-field detection and delineation;
- Textural indicators have shown to be with NDVI the most important discriminative variables between smallholder and large-scale agriculture.
- Most of the studies attempting to identify crop-fields are based on supervised classifiers that need some in-situ data (e.g. cropland maps) / human intervention hardly transferable to other locations.
- Almost all the studies on land use changes are based on the changes between different cropland maps.
- Detection, characterization (typology) and dynamic (consolidation, expansion) of agricultural land use systems are still missing.

In order to bridge the gap, this thesis aims to explore the power of different spectral, temporal and textural indices in discriminating and characterizing large-scale agriculture at regional scale (in this study Senegal). Because reference data are difficult to obtain for agricultural LSLAs over wide extents, this thesis relies on unsupervised classification methods. The originality lies in the use of change detection algorithms on dense temporal VIs series to first detect pixels with potential agricultural LSLAs installation. More details on the methodological approach and assumptions made in this study are given in the next section.

3 DATA AND METHODS

The methodological approach adopted in this study involves broadly the following steps (detailed in the flowchart presented in **figure 2**):

1. Application of change detection algorithms on medium spatial resolution time series (MODIS NDVI dense temporal series, 250m) in order to detect potential pixels related to agro-industrial activities;
2. For the detected potential locations, extraction of textural/spectral/structural indicators from high resolution satellite imagery (Landsat 8, 30m) in order to discriminate agro-industrial activities from smallholder agriculture/ natural vegetation.
3. Use of the set of extracted features as inputs in an unsupervised clustering algorithm. We expect at this stage to obtain well differentiated clusters, representative of different land use systems.
4. Assessment of results using a ground-truth database.

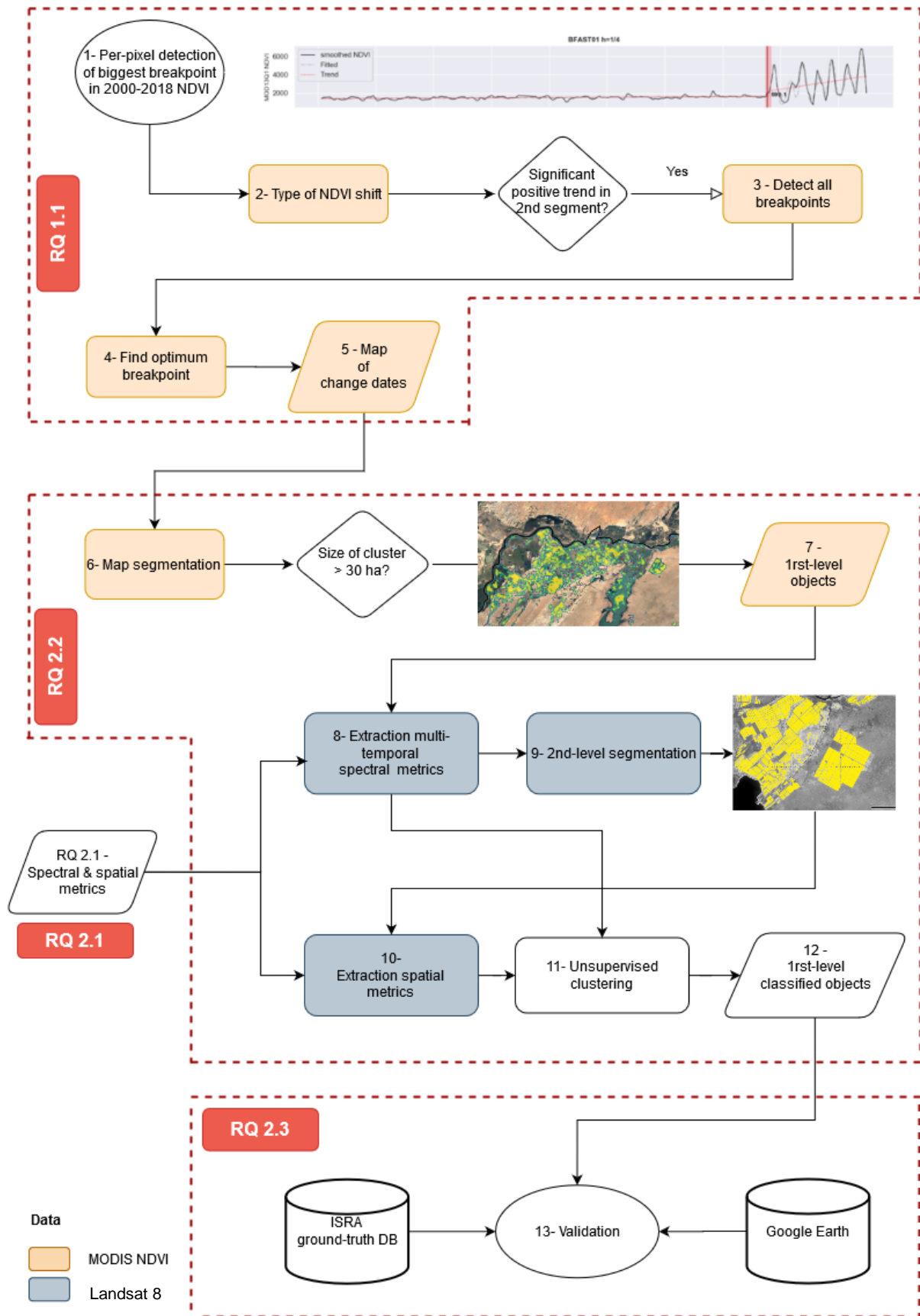


Figure 2: Flowchart of the methodology

3.1 STUDY AREA

Senegal is located in the westernmost Sudano-Sahelian zone and is characterized by an overall low, but highly variable inter- and intra-annual mean annual precipitation that constitutes a key constraint to vegetation growth. The precipitation shows an increasing gradient along the North-South direction. A distinct seasonality is present, with a long dry season and a short rainy/growing season spanning from late June to early October (Abel et al., 2019).

With around 3% of its total arable land (270 908 hectares) declared under contract by foreign investors from 12 countries (~20 concluded deals in 2016) , Senegal is as many African countries concerned by large scale land acquisitions as revealed by the Land Matrix database (Harding et al., 2016)). Because more than 50% of those deals have an area under contract smaller than 5 000 ha, the country is however marginally affected by the so called “mega-deals” (>50 000 ha, only 2 out of 19 in 2016). According to the Land Matrix database, foreign LSLA have accelerated since 2004 (with a peak in 2010-2011), and have experienced a new increase since 2014-2015 (Harding et al., 2016). This situation would have been promoted by the government and supported by several development projects in order to: 1) develop food self-sufficiency, 2) facilitate food exports and income generation for farmers, and 3) improve basic infrastructure in remote rural and less productive areas. Most of the concluded projects are concluded for biofuel production (44%, representing 77% of the area under contract) and food crop (28%, representing 8% of the area under contract). It is important to note that all concluded deals for which former land use is known (representing a minority of the LSLA), have acquired land that was formerly used for smallholder agriculture.

The study area of this research represents the northern half of Senegal. The study area coordinates are as follows (in degrees):

[min. latitude: 14.495, min. longitude: -17,473, max. latitude: 16,639, max. longitude: -12,226]

3.2 REGIONAL-SCALE CHANGE DETECTION

3.2.1 MODIS NDVI 16-day composite collection 6 data

With its global coverage, moderate spatial resolution (250m) and high temporal resolution (1-2 days), the Moderate Resolution Imaging Spectroradiometer (MODIS) sensor allows for the detection of subtle changes in land cover. Because LSLA usually involve mechanized farming with fields' size often larger than 250 m x 250m (usually above 30Ha/ \cong 5 MODIS pixels), the 250 m resolution of MODIS pixels is adequate to detect LSLA processes. **The analysis in this study relies on the changes detected in the temporal series of Normalized Difference Vegetation Index (NDVI)**, which is a spectral ratio index closely linked to vegetation productivity and defined below:

$$NDVI = (NIR - RED) / (NIR + RED) \quad (1)$$

Where NIR and RED are the amount of near infrared and red light reflected by the object and recorded by the sensor. The NDVI is based on the inverse relationship between the absorption

of red energy by chlorophyll and the scattering of the NIR by the mesophyll cells of the leaves. Values range from -1 to +1. The more green and turgescient are the leaves, the closer to 1 is the NDVI. A null value (0.1 is usually considered as a threshold) represents more or less the threshold between the presence and the absence of vegetation (Brown et al., 2007; Horion et al., 2010).

A set of MODIS NDVI 16-day composites at 250m resolution was downloaded for MODIS tile h16v07 (Collection 6) from the NASA Earth Data geoportal (<https://earthdata.nasa.gov/>) for the period 2000-2018. The 16-days composite NDVI product, in which NDVI is combined on a per-pixel basis using a maximum value compositing technique, was chosen in order to reduce NDVI variability due to meteorological distortions like clouds. NDVI data was extracted from each HDF4 file and stacked sequentially to produce the NDVI time series. Low quality NDVI observations (pixel quality flags $\notin [0,1]$) were removed as they affect the inter-annual variability of the NDVI time series. Series were then gap-filled with linear interpolations and smoothed using a Savitzky-Golay filter in order to reduce the noise (polynomial order: 1, window length observations: 3) (Chen et al., 2004). This method performs a least squares regression on a small window of the data, then uses the fitted polynomial to estimate the point in the centre of the window. The window is then shifted forward by one data point and the process repeats. This continues until every point has been optimally adjusted relative to its neighbours.

3.2.2 Change detection algorithms: BFAST01 and BFAST

a) BFAST01 for MODIS pixels first filtering

The first change detection algorithm used in this study and applied over the whole national territory is BFAST01 (BFAST denotes Breaks For Additive and Seasonal Trend; Verbesselt et al., 2012). As explained in the package description, BFAST01 selects a suitable linear model with 0 or with 1 breakpoint, by minimizing the segmented residual sum of squares. Then a selection of different statistical tests (in this study: the Bayesian Information Criterion (*BIC*), one fluctuation test: *OLS-MOSUM* and one F-statistic based test: *supLM*) are performed (p -value < 0.05) to test the null hypothesis of zero breaks, and decisions are aggregated to a single decision (Verbesselt et al., 2012; Zeileis, 2005). In this study, because of time constraints, no season-trend decomposition was performed (`st1="none"`) (see **figure 3**). A set of different values for the `Trim` argument (`Trim = [1/5, 1/7, 1/9]`) was for each pixel tested and the value minimizing the residual sum of square chosen. The `Trim` argument represents the minimal segment size (fraction from total sample size (19 years)) for computation of the F statistics.

This algorithm in addition provides a useful function, namely `bfast01classify`, allowing to analyse for each detected breakpoint the type of change experienced. For this, two sub-functions are used: the `flag_type`, which indicates the type of shift experienced (such as: "monotonic increase with positive break" or "reversal: decrease to increase") and the `flag_significance`, which indicates the trend significance for each of the two segments (Verbesselt et al., 2012). Because BFAST01 is sensitive to changes and has the advantage of being fast but detects many false positive (Ngadi, 2020), this algorithm was used in this study

as a first filter to restrict the number of pixels to which the second change detection algorithm would be applied. Two important assumptions were made: 1- **LSLAs new installations induce detectable changes in NDVI time series trend and/or seasonality** and 2- **LSLAs new installations may be related with significant positive NDVI trends**.

As a consequence, only pixels showing a significant positive NDVI trend in their second segment (after the breakpoint detected) are used for further analysis. The rationale of using trend estimations computed by BFAST01 is that trends computed over time series with structural changes have stated to not be reliable. Because of the latter, we considered that a trend estimated over one portion of the time series (after the breakpoint in this case) should be more reliable than the estimation using the full temporal series.

b) BFAST for change detection

The second change detection algorithm applied in order to detect NDVI changes that may be linked to agricultural LSLAs installation is BFAST (Verbesselt et al., 2010a). The algorithm was run on pixels showing a significant positive NDVI trend in the 2nd segment of their 2000-2018 NDVI time series after the breakpoint detected by BFAST01. In order to increase the area of potential detection of agricultural LSLAs, a circular kernel of 3 pixels radius was applied to each one of the previously selected pixel. Because of time constraints, the study area to which BFAST was applied was limited to exactly the northern half of the country.

BFAST uses a generic approach for detecting and characterizing abrupt changes within trend and seasonal time series components. Iterative decomposition of time series into trend, seasonal and noise components is integrated with methods for detecting changes (Verbesselt et al., 2012). The general mathematical representation of the time series decomposition, usually based on the additive decomposition, is given below:

$$y_t = T_t + S_t + \varepsilon_t, \quad t = 1, 2, \dots, n \quad (2)$$

Where T_t is the trend component, S_t is the seasonal component, and ε_t is the remainder component, all at time t . n represents the number of observations available for the time series. Other commonly employed decompositions methods are the multiplicative, logarithmic, and pseudo-additive ones. Because the season-trend model can be formulated as an Ordinary Least Squares (OLS) regression, breakpoints can be estimated by assessing deviations from the classical linear regression model. When B breakpoints are estimated, $B+1$ segments with constant regression coefficients are yielded, allowing the regression model to be rewritten as a piecewise linear model. The final number of breakpoints is then achieved during an iterative process by minimizing the residual sum of squares of the modified regression model (Almeida, 2017).

An illustrative example of the breakpoints found by BFAST01 and BFAST on one study case is given here below in **figure 3**.

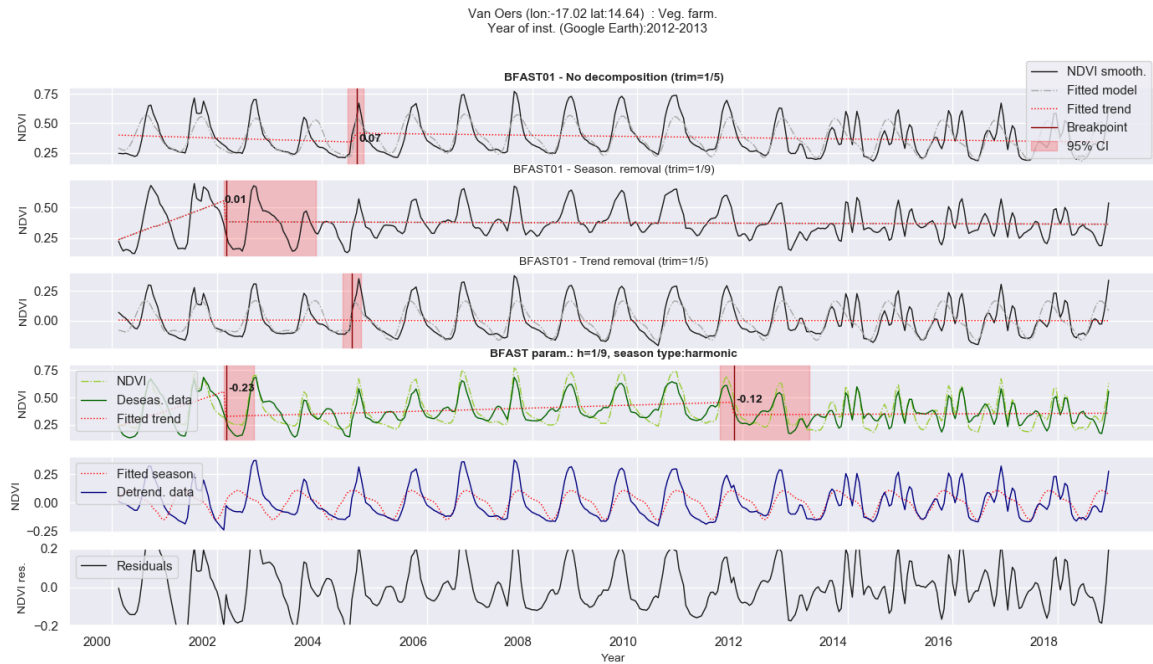


Figure 3: BFASST01 and BFASST detected breakpoints in MODIS 2000-2018 NDVI time series, after optimization of the trim and h parameters (Source: Ngadi, 2020). Detected breakpoints are represented by vertical red lines with red shaded areas indicating the range of the 95% estimated confidence intervals (CI). From up to bottom: 1) BFASST01 detection on the non-decomposed NDVI time series, 2) BFASST01 detection on the trend component (de-seasonalized data - T_t), 3) BFASST01 detection on the seasonal component (detrended data - S_t) 4) BFASST detection on the trend component (in green), 5) BFASST detections on the seasonal component (in blue), 6) time series residuals of the BFASST season-trend model.

The maximum number of breaks is determined by the parameter h (similar to the Trim parameter in BFASST01) which limits the minimal distance between consecutive breakpoints. This parameter, as Trim, represents the minimal segment size (fraction relative to the sample size (19 years)) between potentially detected breaks in the trend model. It prevents that detected breakpoints are solely affected by year-to-year changes and supports the detection of only major breakpoints in the long-term trend (Almeida, 2017; Forkel et al., 2013). Minimal h values suggested in the literature vary between 2-4 years. In this study a set of different values ($h = [1/5, 1/7, 1/8, 1/9]$) corresponding to 3.8, 2.7, 2.4 and 2.1 years respectively) were tested, following the preliminary results obtained in Ngadi et al. (2020). The value minimizing the residual sum of squares was chosen. Given the value for h , the optimal number of breakpoints is determined by minimizing the Bayesian Information Criterion (BIC), which penalizes more heavily complex models, i.e., models with a larger number of breakpoints. The test applied to detect the existence of any abrupt change within temporal series is based on the moving sums (MOSUM) of ordinary least squares (OLS) residuals (OLS-MOSUM, p -value < 0.05) (Zeileis et al., 2002).

Following the results obtained in a previous study that made use of BFASST to detect changes within the seasonal NDVI component over the same study area (Ngadi, 2020), this study focuses on the detection of changes within the NDVI time series trend component.

3.2.3 Selection of a unique breakpoint

In order to obtain one date of change map, a unique breakpoint needs to be selected for pixels where multiple breakpoints are detected by BFAST. To do so, we tested three different metrics that may be associated to changes in time series pattern. Each metric was computed for each segment of the time series delimited by the breakpoints, and correspond for each segment to: the average of the annual number of peaks, the average of the annual maximum NDVI, and the median of the annual 16-day mean NDVI. Those metrics are illustrated in **figure 4**. While the top subplot represents the NDVI 2000-2018 temporal series in green, with the detected breakpoints indicated by vertical red lines, the bottom subplot indicates the values of the three different metric tested for each one of the time series segment. More details can be found in the legend. Our objective here was to select the breakpoint that is most probably related to agricultural LSLAs installations. By default, BFAST selects the breakpoint associated to the highest trend change (highest magnitude value), which corresponds to the first breakpoint (see magnitude values) in **figure 4**.

The bottom subplot of **figure 4** shows however that the biggest change regarding the three computed metrics per segment (namely the number of annual NDVI peaks, the average annual maximum NDVI and the median of the annual 16-day mean NDVI) occurs in the second detected breakpoint (change between the second and third segment). Hence, those metrics seem more sensitive to a change in the time series pattern.

The advantage of using an annual averaged NDVI metric with respect to the annual maximum NDVI, is that not only installations showing a very intense productivity may be detected, but also those with lower (but constant) NDVI throughout the year that may be indicative of the presence of irrigation systems. Therefore, in this study, the median of the annual 16-day mean NDVI was used to select the breakpoint in the MODIS NDVI time series that may be related to agricultural LSLAs. In order to limit the detection of false positives (particularly related to natural vegetation which presents lower NDVI values), a low threshold was applied based on the average annual maximum NDVI.

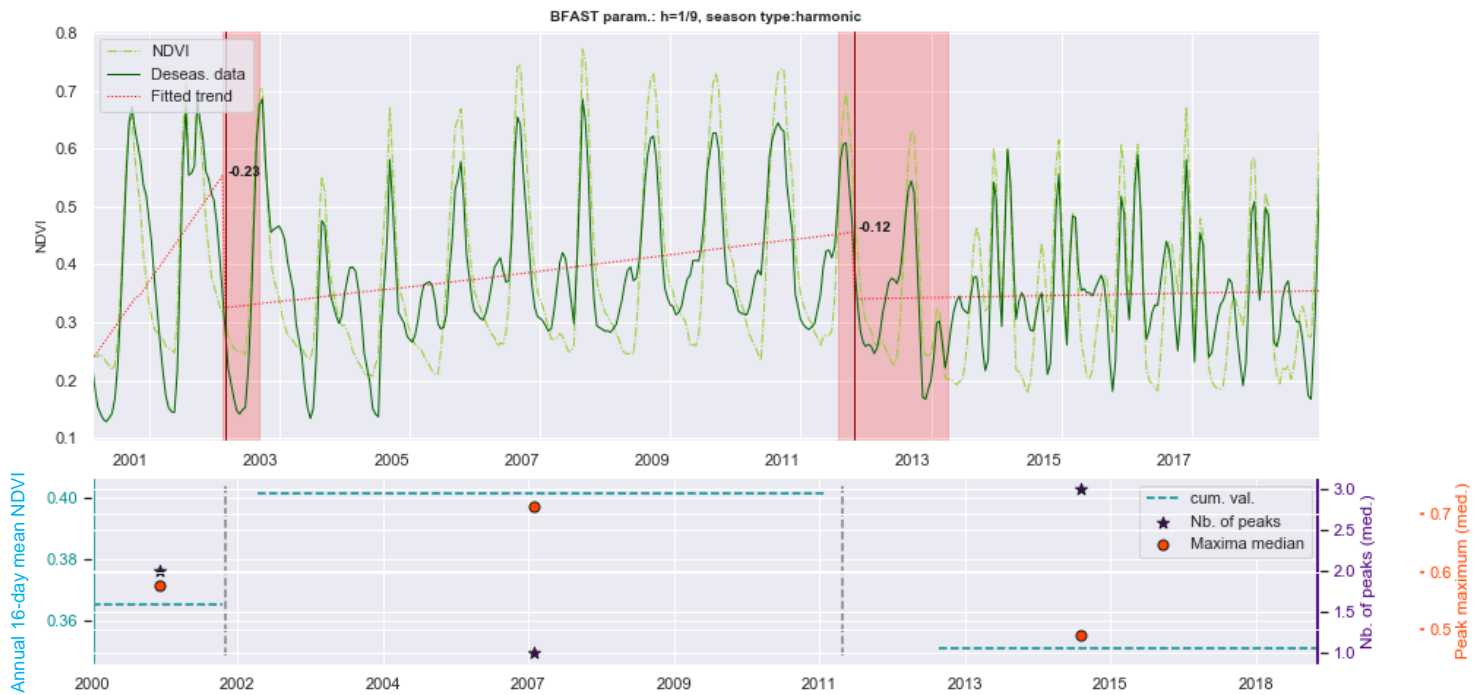


Figure 4: BFAST breakpoints detection within MODIS 2000-2018 NDVI time series (green line on top subplot) on a study case (“Van Oers”). Top subplot: detected breakpoints are represented by vertical red lines with red shaded areas indicating the range of the 95% estimated confidence intervals (CI). NDVI trends in each segment of the time series are represented by dashed red lines. Numbers over the red shaded areas indicate the magnitude of the trend change. Bottom panel: 3 metrics computed for each segment of the temporal series are shown: the median of the annual 16-day mean NDVI (dashed blue horizontal lines), the median number of peaks per year (purple star) and the median of the annual maximum NDVI (red dot).

3.2.4 Change map clustering

a) Clusters edge detection

Once a unique breakpoint per pixel selected, a date of change map was computed and clustered. The change map clustering allowed to find groups of MODIS pixels that underwent similar land-use changes. To identify spatial processes that occurred at similar dates, a moving window of 5×5 pixel size was applied to the change map. During the process, if the difference in date between the windows central’s pixel date P and each one of its 2nd degree neighbours V_i is less than 4 years, +1 is assigned to the central pixel. At the end of the process, values indicating the number of similar neighbours range between 1 and 25, as shown in **figure 5**.

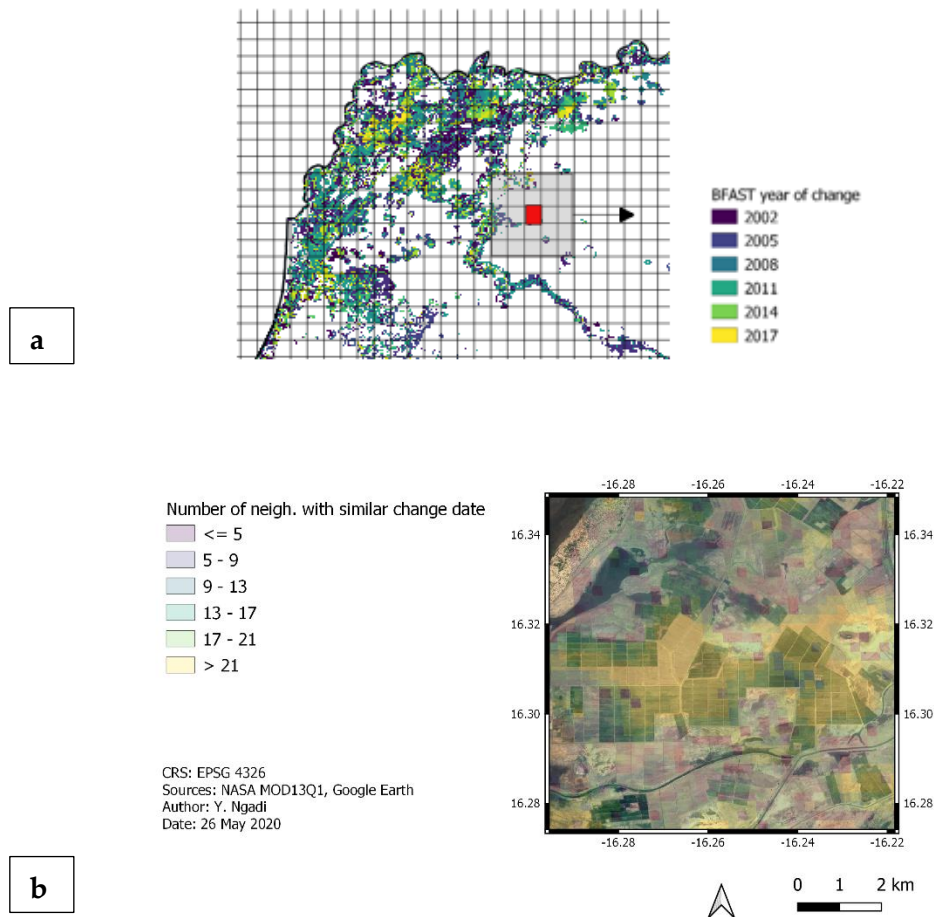


Figure 5: Delimitation of MODIS date of change map clusters edges. a) Illustration of the processing 5x5 rolling window (grey rectangle) over the BFAST date of change map (grid is not at the real scale). The cell in red is the central pixel P , V_i [$i=1, \dots, 24$] the neighbour pixels are represented in grey. b) Illustration of outputs for a small area in the north. The value ranging from 1 to 25 indicates for each pixel the number of neighbours that experience some change in a lapse of time less than 4 years.

b) Map segmentation using the Watershed algorithm

The watershed segmentation is a region-based method that has been successfully used for field boundary delineation (Watkins et al., 2019b; a). As already introduced in sub-section 2.2.3, while edge-based methods exploit variations in the image (edges or discontinuities between pixel values), region-based methods group pixels into objects based on some homogeneity criterion. In the watershed segmentation (Beucher, 1992), the image is considered as a topographic surface, where regions of higher altitude (ridges, or pixels with high intensity) are found that divide regions of local minima (basins). In order to avoid over segmentation, the marker-controlled watershed algorithm makes use of specific seed points (manually or automatically defined markers) from which flooding is simulated. The image partitioning occurs when the flooding level increases to the point where two or more basins merge (creating thus a watershed line). Because each initial marker has a one-to-one

relationship to a specific watershed region, the boundaries of the watershed regions are arranged on the desired indicated ridges, leading to the final segmentation.

In the specific case of the change map segmentation, we applied the marker-based watershed algorithm to the edge map obtained using the 5x5 rolling window as explained in the previous section. Because the values range from 1 to 25, we applied a global threshold to create the markers. Pixels with values below 10 (pixels with number of neighbours having similar date of change values below 10) were assigned as “background” markers, while pixels with values above 17 were assigned as “foreground” markers. Values in between were assigned as “unknown” and assigned to background or foreground pixels by the watershed algorithm.

Once the date of change map segmented, a size filter was applied to remove clusters below 20 hectares. Then, each cluster was assigned a unique date of change corresponding to the median of the within-cluster pixels’ year of change.

3.3 OBJECT-BASED LANDSCAPE ANALYSIS APPROACH

3.3.1 Landsat-8

After the detection of MODIS pixels potentially linked to agricultural LSLAs, we performed an OBIA on Landsat 8 Operational Land Imager (OLI) imagery. Landsat is an earth observation program conducted in partnership by the U.S Geographical Survey (USGS) and NASA that creates high-resolution (30 m for spatial bands in the visible, infrared and near-infrared regions of the spectrum. The thermal-infrared is collected at 100m but resampled to 30m). The revisit period is 16 days. The Landsat program has been running since 1972 and is the longest ongoing project to collect such imagery. Its imagery has been widely used in land-use change studies (Bey et al., 2020; Graesser et al., 2017; Roy et al., 2014).

In order to determine the nature of the landscape object that underwent some land-use change (as detected by the change detection algorithms applied on MODIS time series), we used a two-year period of Landsat 8 Level-1 (Tier 1) products (available on AWS (<https://aws.amazon.com/opendata/public-datasets/>)). Spectral information from two consecutive seasons (with multiple images) in a crop-year would be sufficient to identify the irrigated crops (Ozdogan et al., 2010). Landsat Tier 1 images have the highest level of pre-processing, with geo-registration to less than or equal to 12 m root mean square error (RMSE), inter-calibration to a level deemed suitable for multi-sensor time series analysis, atmospheric correction and cloud and shadow data generated (United States Geological Survey, 2020a). Data was further rescaled to top of atmosphere (TOA) reflectance using the Python module `rio-l8qa`, which makes use of the radiometric rescaling coefficients provided in the metadata downloaded and formulas provided by USGS (United States Geological Survey, 2020b). An image selection was performed based on the cloud coverage. Only one image per month (the less cloudy image, below 20%) was kept for further analysis, resulting in temporal stacks of ~24 images per cluster.

Each image tile was spatially centred at each detected MODIS cluster and had a spatial extent of 0.08 x 0.08 degree latitude-longitude. This extent was selected as it is big enough (square tile inner circle of approximately ~ 6km radius) in order to avoid central objects of interest to touch the image boundaries. Because this study is based in part on the shape of the retrieved objects, it is important that the objects of interest are not situated at the corner areas of the image as they would end with simpler geometrical (rectangular) shapes. The two-year period starting date was dependent of the median date of change assigned to each cluster. Because Landsat 8 imagery is available on AWS as from 2015, 2015 was chosen as the starting year for clusters which change year detected is prior to 2015. For detected changes posterior to 2015, the detected year of change was used as the starting year.

3.3.2 Object-based extracted features: vegetation indices, landscape and textural metrics

Landsat 8 images were used to extract different vegetation indices (VIs) and landscape/textural metrics at the landscape object level (the methodology used to extract the objects is explained in the next section). The landscape object is here defined as homogeneous areas or “patches” detectable from earth observation images (e.g. agricultural fields). VIs were selected in order to be spectrally complementary. Four VIs were computed namely NDVI, NGI, NDWI and NDBal. For each one the 25th, 50th and 75th quantiles over the 2-year period were computed, as well as the coefficient of variation. Details of each (except the NDVI which details are given in section 3.2) are given here below. This section also present the landscape and textural metrics that were selected and extracted from each landscape object to help in the discrimination between natural vegetation, smallholder croplands and large-scale croplands.

a) Vegetation Indices (VIs)

- The Normalized Green Index: NGI

The NGI is the product between the Normalized Difference Vegetation Index (NDVI, refer to equation 1) and the Greenness Index (GI) as indicated here below:

$$NGI = NDVI \times GI \quad (2)$$

$$GI = NIR/GREEN \quad (3)$$

Where NIR and GREEN corresponds to the near-infrared spectral band and the green spectral band respectively. NGI is an interesting VI candidate as it has shown to be effective in discriminating irrigation from non-irrigation crop fields (Pun, 2019). It is based on the NDVI, one of the most used VI for vegetation and irrigation monitoring, and GI (Gitelson et al., 2003), a less exploited VI more sensitive to chlorophyll than NDVI (Pun, 2019). Because irrigated fields often exhibit greater greenness due to the constant availability of moisture, a more sensitive index to vegetation greenness may be useful. This is particularly true in areas with multiple irrigation periods and several crop types with different schedules, where the NVI signal may not be enough to make the distinction (less spectral contrast) (Ozdogan et al., 2010). The NDVI is also very sensitive to background factors (soil brightness and colour, atmosphere scattering, cloud shadow)

- The Normalized Difference Water Index: the NDWI

The NDWI is derived from the NIR and shortwave infrared (SWIR) channels (see equation 4) and is complementary to NDVI (Gao, 1996).

$$NDWI = (NIR - SWIR) / (NIR + SWIR) \quad (4)$$

This VI is a plant moisture based index that responds to changes in both the water content (absorption of SWIR radiation) and spongy mesophyll (reflectance of NIR radiation) in vegetation canopies. Compared to NDVI it does not have any saturation issue. However, it is sensitive to surface wetness.

- The Normalized Difference Bareness Index: NDBal

$$NDBal = (TIR - NIR) / (TIR + NIR) \quad (5)$$

The NDBal (Zhao et al., 2005) is an index developed to detect bare lands, which introduces the thermal infrared band (TIR). Following Zhao et al. (2005), NDBal allows the distinction between primary bare lands (because of physiographics factors), secondary bare lands (anthropogenic factors) and cultivated lands (fallow). Because discrimination between natural vegetation and croplands may be more difficult in tropical regions, we found useful to include this index to our subset of spectral transformations indices.

b) Landscape metrics

As introduced in section 2.2.3 landscape metrics refers to indices that quantify the composition and spatial arrangement of elements across a landscape. They exist at the patch, class/patch type, and landscape levels (McGarigal, 2001). Because this study relies mostly on the shape of the patches extracted from Landsat 8 imagery (more specifically, extracted from the image resulting from the product of the computed yearly NDVI 90th percentile with the yearly NDWI 90th percentile. Refer to section 3.3.3b), we only tested two metrics related to the shape of the patches using the PyLandStats module in Python (Bosch, 2019).

The first metric computed was the “Landscape shape index”, which is a measure of shape complexity. In order to take into account the dependence of the patch shape complexity to its size (i.e. larger patches have smaller perimeter-area ratio) this metric is adjusted for a standard square shape. Its formula is given here below:

$$SHAPE = 0.25 P / \sqrt{a} \quad (6)$$

With P , the patch perimeter and a , the patch area. SHAPE equals 1 when the patch is maximally compact, and increases without limit as patch shape becomes more regular.

Another similar metric tested was the “Landscape fractal dimension”, which has the following formula:

$$FRAC = 2 \ln (0.25 P) / \ln(a) \quad (7)$$

With P , the patch perimeter and a , the patch area. FRAC approaches 1 for very simple shapes such as squares, and approaches 2 for complex plane-filling shapes.

c) Textural features

Textural features, as introduced in section 2.2.3., describe the spatial arrangement of reflectance values of a contiguous set of pixels in a local neighbourhood of an image (Hall-Beyer, 2017; Haralick et al., 1973; Kupidura, 2019). In this study, the 13 second-order textural metrics as defined by Haralick et al. (1973), were computed on the 2-year period NDVI 75th quantile images. For this, the Mahotas library in Python was used (Coelho, 2012). These metrics are: 1) the Angular Second Moment (ASM), 2) the Contrast, 3) the Correlation, 4) the Variance, 5) the Inverse Difference Moment, 6) the Sum Average, 7) the Sum Variance, 8) the Sum Entropy, 9) the Entropy, 10) the Difference Variance, 11) the Difference Entropy 12-13) the Information Measures of Correlation 1 and 2, which are two versions of non-parametric correlation coefficients (Linfoot, 1957).

Because many of the textural measures are highly correlated one with another, a first filtering was performed based on the Pearson correlation matrix between the thirteen different textural metrics. Were only kept metrics with a value <0.7 . Then, a second selection was performed in order to keep a maximum of 3 textural metrics. This selection was based on the complementarity between textural metrics. Following Hall-Beyer (2017), textures may be divided into 'edge' and 'interior' textures. 'Edge' textures yield high values when the neighbourhood contain visual edges, such as the Contrast (which measure the amount of local variations). It is also the case of the Variance, which however also yield high values in areas of incoherent high variability (without edges). The Entropy yield high values in case of irregular edges or incoherent contrast, and lower values in presence of straight-line edges. 'Interior' textures refer to textures able to characterize areas "away from coherent edges" such as the ASM, which measures the homogeneity of an image (presence of dominant gray-tone transitions) or correlation, which measures gray-tone linear dependency in the image (Hall-Beyer, 2017; Haralick et al., 1973). In this study, the final set of textures used is formed by: the Entropy (Ent), the Sum of Variance (sVar) and the Information Measure of Correlation 2 (infCorr2).

Because textures are highly dependent on the window size used to compute them, three different sliding windows were tested: 5x5 pixels, 10x10 pixels and 15x15 pixels. The window size is important because if too small (e.g. 3x3) it may be less robust to within-class variability, and thus less useful for classification purposes. On the other hand, if window sizes are too big (e.g. $>50 \times 50$), then the metrics may be affected by the so-called edge-effect problem (texture variation caused by the between-class texture and not by the within-class texture) (Ferro et al., 2002). However, because we are computing textures on segmented objects that present a certain level of homogeneity, we should be less concerned by the edge effect problem. This is why we tested a range of medium window sizes (5x5, 10x10, 15x15).

3.3.3 Image segmentation using the Watershed algorithm

The segmentation algorithm (marker-controlled watershed) introduced in subsection 3.2.4 was also applied to Landsat 8 images in order to obtain objects with a higher spatial resolution

than MODIS. However, the processes to delineate object contours (edge extraction) and to create markers for the watershed algorithm were different. Those two automatic processes are detailed in the following sub-sections.

a) Edge detection

For delineating crop fields' boundaries, multiple Landsat 8 images (2-year period, representing ~5 to 24 images with cloud coverage <20%) were acquired for each cluster of MODIS pixels detected (refer to section 3.2.4b). As we aimed to implement a generic methodology, no selection of images within the growing season was done (as the growing season varies in function of the ecozone). Instead, we composited the full temporal stack of images using the 75th percentile for a subset of three VIs (see section 3.3.3 for more details): NGI, NDWI and NDBal. Those VIs were selected because of their spectral complementarity (inclusion of the optical bands, near-infrared band, short-wave infrared band and thermal infrared band). Prior to edge extraction, each composite image was spatially smoothed using a bilateral filtering ($d=20$, $\sigma_{\text{Color}}=30$, $\sigma_{\text{Space}}=50$), which has the property of smoothing image noise while preserving true edges (Tomasi et al., 1998), and facilitate this way the image segmentation. The three parameters introduced in the smoothing algorithm control the diameter of the pixel neighbourhood (d), the standard deviation of the filter in the colour space (σ_{Space}) and the standard deviation in the coordinate space (σ_{Space}). This filter is basically a weighted average of local pixels that considers pixel neighbours in the spatial domain but also in the colour domain. Larger values of d increase the contribution of more distant neighbouring pixels. Larger values of σ_{Color} imply that colors which are farther apart to each other will start to get mixed. Larger values of σ_{Space} smooths neighbourhoods with small variance (uniform areas) but also with large variance. The spatial parameter is proportional to the image size, and may be set to 2% of the image diagonal. The values chosen in this study were empirically selected and correspond for σ_{Color} to the interquartile range of the intensities (rescaled to 0-255), and for σ_{Space} to 7% of the image diagonal.

After the process of image smoothing, a simple standard deviation edge detection algorithm was applied to each image (NGI, NDWI, NDBal). The values were then then summed through the images to obtain one unique edge image (see **figure 7**).

b) Watershed markers creation

The input images used for segmentation are the images resulting from the product of the yearly NDVI 90th percentile image with the yearly NDWI 90th percentile image. While this product does not have any physical meaning, it allows obtaining good contrasted image useful for further segmentation. In addition, the product of those two normalized index (range: [-1 1]) allows to remove the contribution of flooded objects (containing free water) with very high NDWI values from the segmentation, as the same objects have very low NDVI values. Prior to segmentation, and in order to remove some image noise, input images were smoothed (see **figure 6**) using the bilateral filter as explained in the previous section.

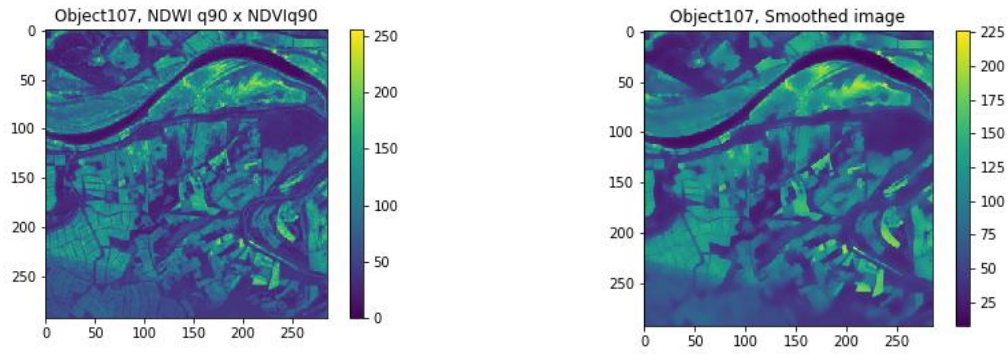


Figure 6: Example of input Landsat 8 images used for the segmentation process. Left-subplot: product of the average of the Landsat 8 2-year annual NDVI 90th quantile and the average of the 2-year annual NDWI 90th quantile. Right-subplot: Same image as the left, but smoothed using the bilateral filter. Both images were rescaled to 0–255 to store the results in unsigned 8-bit data needed for segmentation.

Binarization of the smoothed images was done by the Otsu global thresholding algorithm. Based on the input image histogram, the algorithm returns a single intensity threshold that minimizes the weighted-class within variance, and that separate pixels into two classes: foreground and background. This technique relies on the assumption that the image histogram is bimodal and that a reasonable contrast ratio exists between the background and objects of interest. Because this is not always the case, Otsu’s thresholding was mostly used in this study to identify ‘sure’ background markers that will be used as input in the marker-based watershed segmentation.

Once the background markers found, the identification of foreground markers was achieved by extracting the binary image skeleton. This process allows to reduce the foreground regions to a skeletal remnant that preserved the extent and connectivity of the original region (Fisher et al., 2020). Prior to the skeletonization, image morphological operators were used in order to minimize holes between foreground (as opposed to background) objects. The latter allows to extract meaningful *groups* of objects. Indeed, in this study we did not want to extract individual objects separated from their context (such as an agricultural parcel). Our aim was to extract meaningful groups of objects, with distinctive contours, assuming that a group of large-scale agricultural objects would be different that a group of smallholder agricultural objects.

During the skeletonization process, each pixel’s value was replaced by its distance to the nearest background pixel. Pixels above a predefined distance threshold were then used as foreground markers needed in the marker-based Watershed segmentation. The higher the threshold value, the more restrictive is the condition on foreground candidate pixels (pixels need to be at a higher distance from the predefined background pixels in order to be considered as foreground pixels). At the same time, fewer number of objects are extracted from the images as many pixels do not satisfy the threshold condition.

The final step of the segmentation consisted in “feeding” the marker-based Watershed algorithm with the previously defined markers (background and foreground) and extracted

edges. During this last process, the algorithm labelled the unknown pixels as ‘background’ or ‘foreground’ pixels.

Because distance thresholds affect the overall shape of the segmented object, two distance thresholds were tested in this study (i.e. 0.2 and 0.6, distance normalized). Refer to next section for more details.

Figure 7 here below illustrates the different outputs (edges, image binarization, image skeletonization and watershed segmentation) obtained for one Landsat image.

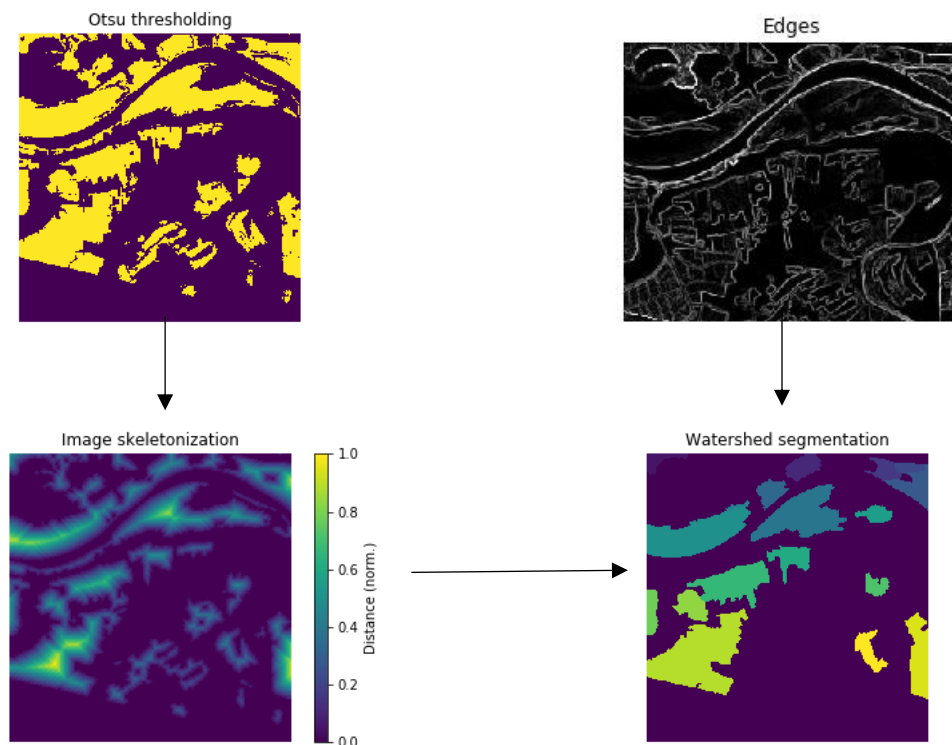


Figure 7: Image segmentation process steps applied on Landsat 8 images. The top-left subplot shows the edges extracted using the methodology detailed in subsection 3.3.2 b. Top-right image: image binarization using Otsu’s automatic thresholding. This step allows to define the background markers (pixel’s value=0, shown in dark blue) needed for the segmentation. Foreground markers are shown in yellow (pixel’s value=1). Bottom left image: binary image skeletonization, in which the values represent the distance of each pixel to the nearest 0 pixel value. Bottom-right image: after having applied a distance thresholding in order to define the watershed foreground markers (i.e. those with a distance > threshold), the original combined VI image (NDVI x NDWI) is segmented using the watershed algorithm, the edges extracted, and the markers previously defined.

3.4 UNSUPERVISED CLASSIFICATION

Unsupervised classifiers are often used as an exploratory tool to assess data internal structure. In this study our aim was twofold: 1) identify some of the most important remotely sensed features that contribute to LSLAs’ discrimination over large spatial extents and 2) obtain an accurate classifier able to discriminate agricultural LSLAs. In order to do so, the selection of a meaningful and dimensionally reduced dataset is of primordial importance.

3.4.1 Input dataset

The data used to train the unsupervised classifier consisted in the spectral and textural metrics computed for each landscape object retrieved from the Landsat 8 images. Three textural window sizes (5, 10 and 15), two distance thresholds (0.2 and 0.6) and input datasets with and without the shape metrics (in order to test their discriminative power), leading to **12 input datasets**. Those datasets comprise: the 25th, 50th, 75th quantiles and coefficient of variation of four VIs (NDVI, NGI, NDWI, NDBal), the 13 Haralick textures computed on the 2-year composite NDVI images and optionally, as aforementioned, the shape metrics. After feature selection based on the Pearson correlation matrix (only features with values below 0.7 were kept), the following 8 features made our core input datasets, allowing to achieve very low (below 0.05) Hopkins scores indicating a high clustering tendency within the data:

- NDWI: the 2-years period 75th quantile and coefficient of variation (NDWI_q75);
- NGI: the 2-years period 75th quantile (NGI_q75);
- NDBal: the 2-years period coefficient of variation (NDBal_cv);
- NDVI: the 2-years period coefficient of variation (NDVI_cv);
- The Information Measure of Correlation2, averaged over the 2-year period (infCorr2);
- The Sum of Variance 2-year average (sVar);
- The Entropy 2-year average (Ent).
- The landscape shape index (optionally)

The number of objects within the dataset constructed with the distance threshold=0.2 is 1388, and 606 in the dataset using the distance threshold=0.6.

3.4.2 The Self-Organizing Map (SOM)

A two-level unsupervised clustering approach was chosen in this study. While the first step consists in a dimensionality reduction of the input data set, the second step consists in the application of a clustering algorithm to the newly obtained and reduced data set. The idea of this two-level clustering is to perform data clustering more efficiently and to make data exploration and visualization easier (Cabanès et al., 2007). Indeed, it is better to cluster a smaller set of representative data (prototypes) than directly the original data set. By doing so, noise reduction is gained as the prototypes are local averages of the data and, therefore, less sensitive to random variations than the original data (Vesanto et al., 2000a). In addition, because high-dimensional data may be sparse and difficult for a clustering algorithm to find any structure in the data, a dimensionality reduction allows to perform clustering more efficiently and to mitigate the so-called curse of dimensionality.

In the first step of the unsupervised classification, a Self-Organizing Map (SOM) (Kohonen, 2013) was used in this study. During the analysis, the SOM projects data (vector projection) onto a lower dimensional display (i.e. a two-dimensional map formed from a grid of nodes). By doing so, it reduces the input data size by performing (input) vector quantization. The data is then replaced with a representative set of nodes (each node consist in a vector of same feature dimensions than the input data) which form the nodes of the grid. The distance between data sample pairs in feature space is preserved as good as possible during projection.

Similar multi-dimensional samples are grouped together and are organized with well-defined positions on the projection grid map. As a consequence, data cluster structure can be easily visualized and some quantitative descriptions of the dataset can be extracted grouping similar map units using a clustering algorithm (Vesanto et al., 1999).

An illustration of the process is given below, in **figure 8**. At first, the initial SOM nodes are arbitrarily positioned in the data space and low weights are assigned to each node vector. Then for each data sample (consisting in a vector of n features, and represented with a red dot in **figure 8**), its closest grid node (also consisting in a vector of n dimensions, and represented with a yellow dot) is selected based on its weights (initially very low). This closest node represents the BMU (for Best Matching Unit) of the sample. Once the BMU found, the BMU's weights are updated towards the data sample. At the same time, the BMU's neighbours' weights are also updated (but to a lesser extent, defined by a neighbouring function (usually the Gaussian function) towards the data sample. After many iterations the grid tends to approximate the data distribution in the feature dimensional space.

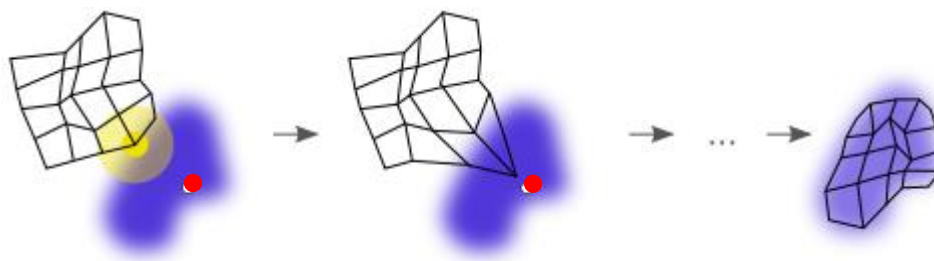


Figure 8: Self-Organizing Map (SOM) training process. The input data set is represented by a blue blob and the SOM map is represented by a black grid. 1) SOM grid initialization (figure at the left): each SOM node is given a small random weight. 2) SOM training (figure in the middle): the BMU (represented in yellow) of each input sample (represented in red dot) is updated, and while doing so each BMU (and neighbours) moves towards the input sample. 3) Trained SOM (right figure)): the SOM grid after training approximates the data distribution (Wikipedia, 2020a). Refer to section 3.4.1 for more details.

For the SOM implementation we used the MiniSom library for Python (Vettigli, 2018). Amongst the different SOM parameters that had to be defined, the first one concerned the size of the map. The number of map nodes were defined using the following heuristic formula (Vesanto et al., 2000b):

$$units = 5 \times \sqrt{N} \quad (6)$$

Where N is the number of observations.

The map size was then determined the same way as in the SOM toolbox, where the ratio of the two largest eigenvalues of the data becomes the ratio of the map length to its width. Knowing the length/width ratio, and the number of units in the map, the length and the width of the SOM map can easily be obtained (units = length x width).

Two metrics were used to assess the quality of the trained maps: the average quantization error (Qe) and the topographic error (Te). The quantization error, which measures the map resolution, is defined as the average distance between each data sample and its BMU. The topographic error, which measures topology preservation, corresponds to the proportion of all data vectors for which the first and second BMUs are not adjacent units (Vesanto et al., 2000b). Because our aim is to further cluster the SOM map, parameter settings that minimize the topographic error were selected. Those parameters consisted in the learning rate (i.e. how much weight is adjusted during each iteration) and sigma (i.e. the spread of the neighbourhood function). To select the best combination, Qe and Te were plotted against different values ranging from 0 to 1 (steps of 0.01) and the values that minimize the topographic error, while giving reasonable good quantization error, were chosen for the learning rate and sigma.

After training the SOM map, data clustering was performed by applying a clustering algorithm to the SOM data-representative nodes as explained the next subsection.

3.4.3 Hierarchical clustering

In this study a hierarchical agglomerative clustering algorithm was used to partition the SOM map. We used the *AgglomerativeClustering* algorithm available in the Scikit-learn library (Pedregosa et al., 2011). Hierarchical clustering algorithms have some advantages over partitioning techniques: 1) no assumption on data distribution is made and 2) the tree-based representation of the observations based on the dissimilarity matrix allows assessing the internal structure of the data. However, these algorithms usually do not work on data of big size.

The agglomerative clustering contains different steps. The pairwise distances (in this study: Euclidean) were first computed for all the input samples. Then a binary hierarchical tree was constructed using the 'Ward' linkage. The selection of the tree-cut level was based on the average of the silhouette coefficient (Rousseeuw, 1987) computed for partitions going from 2 to 20. The silhouette value is a measure of how similar an object is to its own cluster (cohesion) compared to other clusters (separation). The coefficient ranges from -1 to +1, with high values indicating high cohesion and separation from other clusters (Wikipedia, 2020b). The partition leading to the biggest silhouette value, but with the lowest number of clusters k , was selected. The latter avoid the creation of very small clusters. In this study if the difference between the maxima silhouette value achieved for a number k , and the silhouette value for $k-1$ is less than 0.05, then $k-1$ was chosen as number of clusters.

Once the number of clusters predefined, the different trained SOMs (where each map node represents a sample) are clustered. The data represented by the SOM nodes have the advantages to be representative of the original data, smaller, and easier to explore and analyse. After the clustering, and evaluation, because each input data sample possesses a BMU, the original data can be labelled and classified as well.

3.5 EVALUATION

3.5.1 Senegal national ground LSLA database

In order to improve transparency around LSLAs, ISRA conducted an extensive field campaign at the beginning of 2019. More than 800 records and corresponding attributes were recorded in a database. Attributes consist in all kind of information related to the identified deals, such as: name, coordinates, negotiation status, implementation status, year of transaction, size, previous land use, previous land tenure etc. As presented in **Table 2**, LSLAs are equally distributed over the northern part of the national territory (54.5%) and the southern part (45.5%). Median area of the reported LSLAs in the northern part of the country is slightly higher (36.5 hectares) with respect to the national value (30.8 hectares).

While very useful, this database is still incomplete. As illustrated in **Table 2**, less than a half of the reported LSLAs (39%) are known to be “active”, while the other half of the LSLAs (52%) have an unknown status.

The latter means that a non-negligible part of the reported LSLAs may not be active, and as a consequence, may not be detectable with a change detection algorithm. An evaluation of the methodology based on this ground field database has then to be taken carefully.

Table 2: Statistics on LSLAs in ISRA/CIRAD database within the national territory (1st column), and within our study area (2nd column). Statistics concern the LSLAs’ area and the number of LSLAs in different four different status categories: active, abandoned, not yet installed and no information provided. Proportions in red in the table second section (related to the ‘Status’) are relative to the total count of LSLAs over the national territory, and over the study area respectively.

	LSLA area (ha)	
	National territory	Northern half territory
Count	897 (100%)	492 (54,5%)
mean	1395,5	881,4
std	24974,6	10159,2
min	0,0	0,0
25%	6,5	3,4
50%	30,8	36,5
75%	108,2	143,1
max	713063,2	183727,1
<6 ha	216 (24%)	135 (27.4%)
Status		
Active	473 (52%)	192 (39%)
Abandoned/Contract end	20 (2,2%)	8 (1,6%)
Contract intention/promise	64 (7,1%)	34 (6,9%)
No information	337 (37.5%)	258 (52,4%)

3.5.2 Methods applied for evaluation

The evaluation of the methodology applied and the classification achieved, mostly relied on the ground truth database. Specifically, the evaluation consisted in:

- 1- The assessment of the number of potentially detectable LSLAs throughout the different processes applied (NDVI trend filtering, application of change detection algorithms, segmentation). The '**potentially detectable LSLAs**' is here defined as the number of reported LSLAs within the ISRA/CIRAD field database that overlap at least one of the MODIS pixels detected as candidates to LSLAs settlements by BFAST. Because this study implements an exploratory approach that aims to detect *changes* related to agricultural LSLAs, one overlapping pixel is enough for location detection. At this stage, **this study does not aim to infer areas occupied by LSLAs**. Because of a data loss, comparison of the changes detected by BFAST and BFAST01 will not be possible.
- 2- The assessment of the dataset clusterability. This was performed using the Hopkins score (Hopkins et al., 1954) as implemented in Pycluster Python Library (range of values 0-1). A score around 0.5 expresses no clusterability, while a score tending to 0 expresses a high cluster tendency.
- 3- The assessment of the different tested parameters (windows size, distance threshold...) by 1) comparing the performance achieved by the trained classifiers and 2), comparing the values of some internal metrics obtained (Silhouette coefficients), allowing to assess the cohesion and separation of the obtained clusters. The main objective is to determine how the cluster tendency of the data is real and not-random. In addition, the usefulness of landscape shape metrics will be visually assessed by inspecting the shape of different landscape objects for varying parameters.
- 4- The accuracy of the classifiers. This was only assessed for the cluster most likely linked to agricultural LSLAs. The F1 score was computed (using the ground truth database), defined as:

$$F1\ score = 2 \times \frac{(Recall \times Precision)}{(Recall + Precision)} \quad (7)$$

With:

$$Recall = True\ positives \div (True\ positives + False\ negatives) \quad (8)$$

$$Precision = True\ positives \div (True\ positives + False\ positives) \quad (9)$$

The F1 score reaches its best value at 1, indicating a perfect precision and recall. While precision attempts to answer the following question: "What proportion of positive identifications was actually correct?", recall attempts to answer: "What proportion of actual true positives was identified correctly?" (De Ponteves, 2020)

The different classes were computed the following way:

- True positives were considered the Landsat objects classified within the cluster most likely related to LSLAs, that overlap with at least one pixel one of the reported LSLAs.

- False negatives were considered the Landsat objects classified within any other cluster than the one most likely related to LSLAs, that overlap with at least one pixel one of the reported LSLAs.
 - False positives were considered the Landsat objects classified within the cluster most likely related to LSLAs, but which do not overlap any of the reported LSLAs.
- 5- As a last step, visual evaluation of the different clusters was performed using Google Earth satellite imagery.

4 RESULTS

This section is divided into three parts.

The first part of this section focus on the results aiming to solve sub-objective 1. Those are linked to the detection of potential MODIS pixels (at regional level) that may be related to agricultural LSLAs. Two principal assumptions were made here: **1) LSLAs new installations induce detectable changes in NDVI time series trend and/or seasonality and may be related with significant positive NDVI trends; 2) clusters of pixels with similar dates of change are affected by the same underlying change event.** This is how, in this study, the detection of agricultural LSLAs' relies on the detection of MODIS clusters of pixels with similar dates of change.

In the second part of this section, results aiming to solve sub-objective 2 are presented. Those are the results obtained from the Landsat8 image analysis (segmentation) performed over the clusters previously found, and allowing to extract additional spatial and spectral information at the landscape level. The assumption made here is that **3) LSLA' installations exhibit simpler geometrical shapes and are more homogeneous (less fragmented) than smallholder agriculture.** In fact, the methodology developed in this study to detect agricultural LSLAs heavily relies on this assumption.

The last subsection presents the results and evaluation of the unsupervised classifier, trained with the different metrics computed from the retrieved MODIS and Landsat8 spatial objects.

4.1 LAND USE/LAND COVER CHANGE DETECTION BASED ON MODIS

Results presented in this section are directly linked to sub-objective 1: *“Detect potential agricultural LSLAs' installation automatically at regional scale using change detection algorithms and medium resolution satellite (MODIS 250m) temporal series”*

4.1.1 MODIS NDVI pixels masking using BFAST01

The first change detection algorithm used in this study in order to restrict the number of pixels potentially linked to agricultural LSLAs was BFAST01. This algorithm was applied over the whole national territory. As explained in section 3.2.2 BFAST01 detects the biggest significant

breakpoint in temporal series. **Figure 9** shows the date of change as detected by BFAST01 within the MODIS NDVI 2000-2018 temporal series.

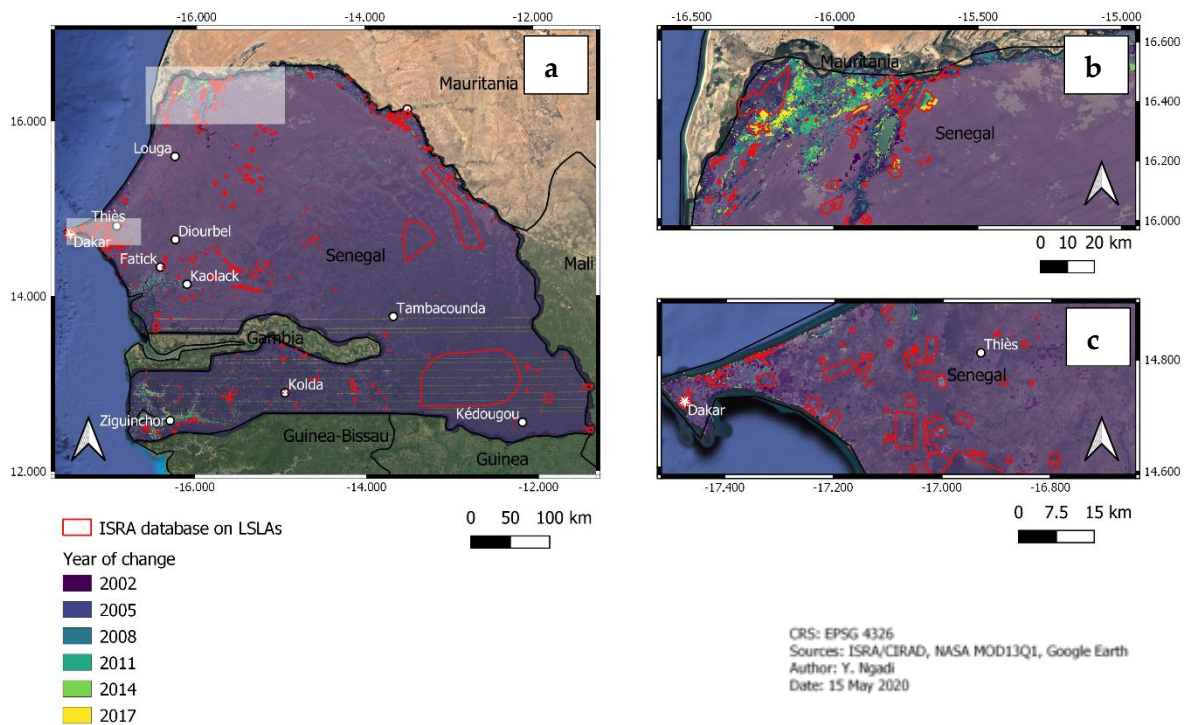


Figure 9: Date of change map as detected by BFAST01 within the MODIS 2000-2018 NDVI time series. Polygons in red represent the agricultural LSLAs defined in the ISRA/CIRAD ground truth database. a) map of the national territory, b) closer view to the north area (Lac de Guiers), c) closer view to the area around Dakar.

Two comments can be made from **figure 9**: 1) one abrupt change has been detected for all the pixels within the national territory, and 2) the year of change for almost all the pixels is the same (2004-2005). Based on the assumption that biomass productivity increases (or at least is expected to increase) after new agricultural LSLAs installations, BFAST01 was then used to detect pixels with a significant positive NDVI trend as explained in section 3.2.2. Those pixels are illustrated in black in **figure 10**.

Table 3 shows a number of statistics related to the potentially detectable LSLAs left after each pre-processing step applied (NDVI trend masking, MODIS pixels clustering and map of change segmentation). The second column of **Table 3** indicates that 57.1% of the field database LSLAs overlap at least one of the masked MODIS pixel (in black, presenting a significant positive trend in the 2nd segment of the time series after the breakpoint detected by BFAST01) in our study area. A slightly higher proportion is observed over the national territory (63.9%). The table also indicates the average area of the potentially detectable LSLAs (i.e. that overlap at least one of the masked MODIS pixels). Median areas of the LSLAs showing a significant positive NDVI trend are at least ten times higher than those not showing any significant positive trend.

Table 3: Number of potentially detectable LSLAs after each one of the processes applied in this section, namely: the MODIS pixel filtering based on the NDVI trend (column 1), the application of the change detection algorithm BFAST (column 2), and the segmentation of the date of change map (column 3). * 'Potentially detectable' LSLAs here refers to LSLAs ground-truth polygons overlapping at least one the remaining MODIS pixels after the application of each process. Metrics given in the upper section of the table are related to the LSLAs' area, while the bottom section of the table provides information on the LSLAs status distribution. ** The number after the 2nd process is higher than after the 1st one because a circular kernel of radius 3 pixels was applied to each masked pixels in order to increase the area of detection. Proportions given in red are relative to the total number of LSLAs in the study area (492). The last column refers to the potentially detectable LSLAs, when only deals installed during 2002-2017 (in order to have any change detectable by the change detection algorithm) are taken into account.

Process	NDVI trend masking (national territory n=897)	NDVI trend masking (study area, n =492)	BFAST change detection *	Change map segmentation	Settlements between 2002-2017
Count	573 (63.9%)	281 (57.1%)	312	279 (56.7 %**)	69 (13.8%)
Average LSLA area (med ha.) - <i>Potentially det.</i>	57,41	81,94	100,4	122,9	127,3
Average LSLA area (med. ha) - <i>Remaining</i>	5,29	2,7	1,5	2,4	22,4
Status					
Active	333	125	158	122,9	54
Abandoned/Contract end	15	6	8	5	3
Contract intention/promise	50	20	29	27	11
No information	172	84	117	103	0
Potentially detectable ***	505 (88.1%)	209 (42.5%)	275 (55.9%)	247 (50.2%)	54 (11%)

4.1.2 BFAST changes detection

The second change detection algorithm used in this study was BFAST. This algorithm was only run over the previously selected MODIS pixels. As detailed in section 3.2.2, it was used in the purpose of detecting NDVI changes that may relate to agricultural LSLAs. In order to do so, a methodology was developed to select what could be the most suitable breakpoint (refer to section 3.2.3). **Figure 10** shows the date of change map obtained over our study area using that technique. The breakpoint selected was the one related to the biggest change in the median of the annual 16-day mean NDVI (refer to section 3.2.3 for more details). **Figures 11(a-b)** allow to compare the date of change maps obtained when using different breakpoint selection methods. While **figure 11a** presents the date of change map obtained when selecting the breakpoint detected by BFAST associated to the biggest trend change, **figure 11b** shows the date of change map obtained when using the method based on the median of the annual 16-day mean NDVI. From those maps, one can observe that the map shown in **figure 11b** is more heterogeneous than the one in **figure 11a**, with a higher number of pixels presenting changes after 2005. At the same time, one can see that visually detectable clusters in **figure 11b** are also represented in **figure 11a**. As a result, a change map based on changes of the median of the annual 16-day mean NDVI may be spatially more interesting for a further map segmentation based on the dates of change.

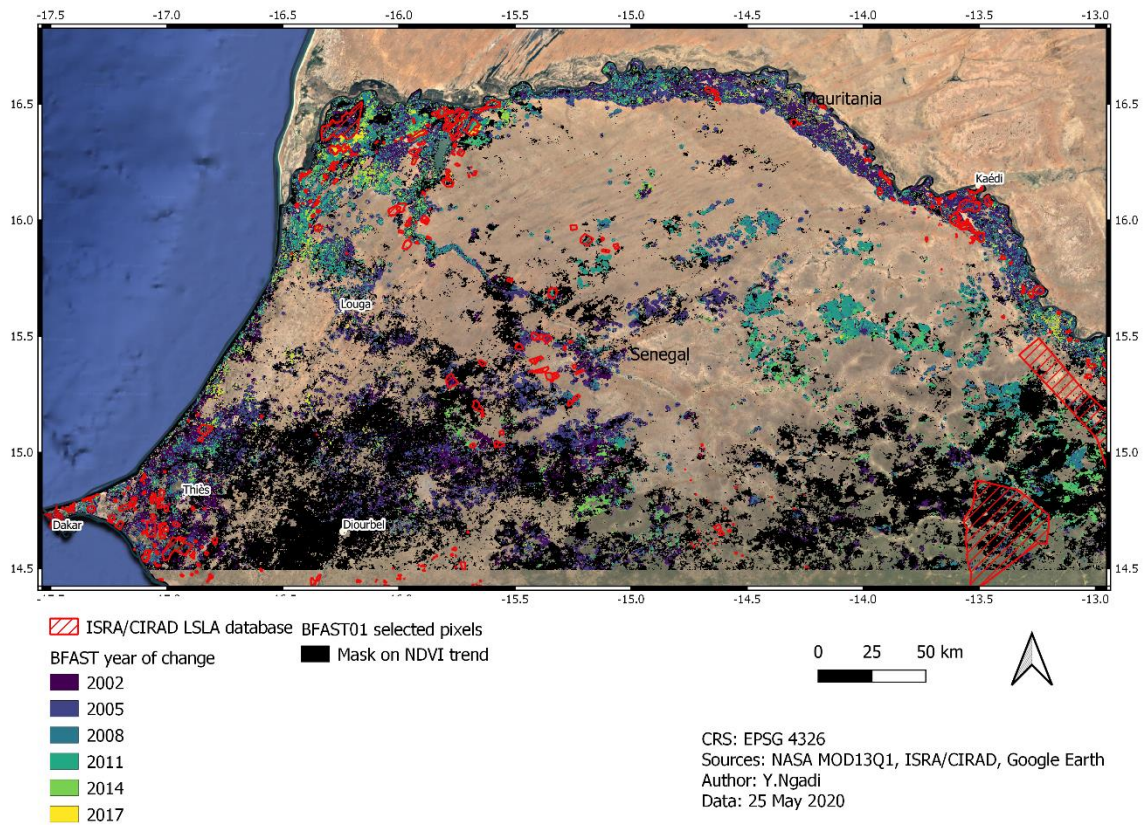


Figure 10: BFAST date of change map for the northern half of Senegal (coloured pixels). Breakpoints chosen are those related to the biggest change in the median of the 16-day mean NDVI per year. BFAST was only applied over pixels in black, presenting a significant positive NDVI trend in their second segment after the breakpoint detected by BFAST01. Polygons in red represent the LSLAs defined in the ISRA/CIRAD ground truth DB.

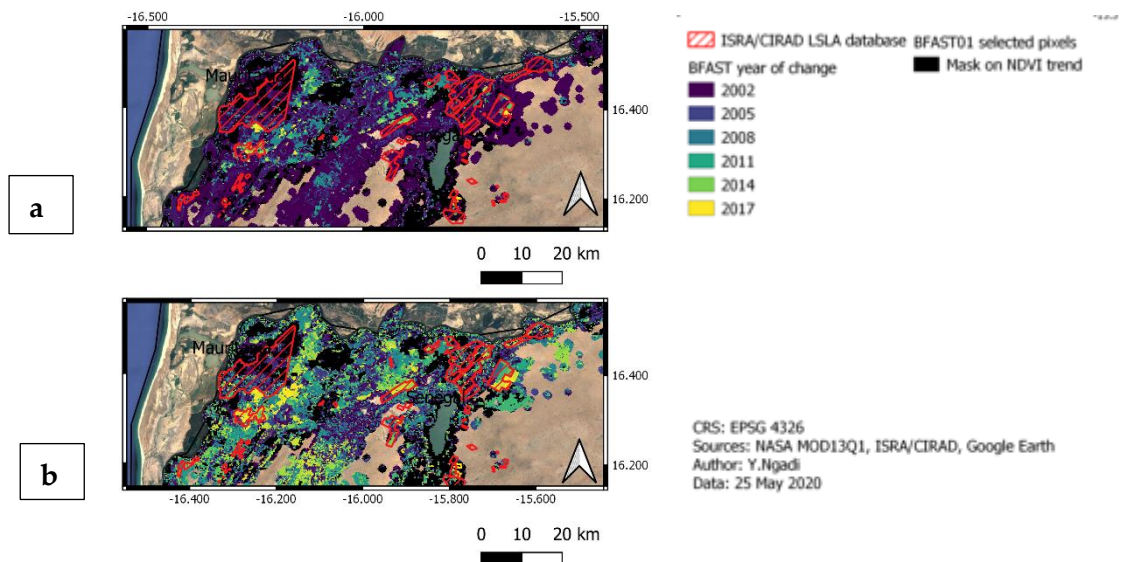


Figure 11: Closer views on the BFAST date of change map (Northern Senegal). a) Date of change map with selection of the biggest breakpoint in the NDVI time series trend component. b) Date of change map with selection of the breakpoint related to the biggest change of the median of the annual 16-day mean NDVI. Polygons in red represent the agricultural LSLAs defined in the ISRA/CIRAD ground truth DB. Pixels in black represent the pixels showing a significant positive NDVI trend in their second segment after the breakpoint detected by BFAST01.

While BFAST did not automatically detect a change for each one of the pixels for which BFAST01 did (see pixels in black in **figure 11**), the number of potentially detectable LSLAs after the application of BFAST did not decrease (see 3rd column of **Table 3**). At this stage, and following **Table 3**, 312 of the field database reported LSLAs are potentially detectable. The latter corresponds to 63% of the total number of LSLAs (492) comprised in the study area.

4.1.3 MODIS-based date of change map segmentation

The date of change map was further segmented following the method described in section 3.3.2. The latter allows to take into account the spatial context of the pixels for which a change was detected, and to extract groups of pixels with similar dates of change. Closer views of the results over the north area are shown in **figures 12a and 12b**. **Figure 12a** indicates the number of neighbors, per pixel and in a window size of 5x5, that have an absolute change date difference below 4 years. Larger clusters of similar pixels are easily observable in yellow, while cluster edges are represented by pixels in blue/black. Because bigger clusters have central pixels with higher values, this segmentation introduce a bias towards bigger clusters. The latter is observed in **Table 3** with the increase of the median area of the potentially detectable LSLAs (4th column).

Figure 11b presents the clusters obtained after the change map segmentation, using the marker-based watershed algorithm and the MODIS clusters' inferred edges. At this stage, a total of 1190 MODIS clusters were extracted over the study area, that overlap with at least one pixel 57% of the reported LSLAs (279) (see **Table 3**). The proportion is reduced to 50.2% if we discard the abandoned/cancelled or not yet active LSLAs. And the proportion is even lower (11%) if we just consider the settlements between 2002 and 2017 (period of time in which a change may be detected by the change detection algorithms).

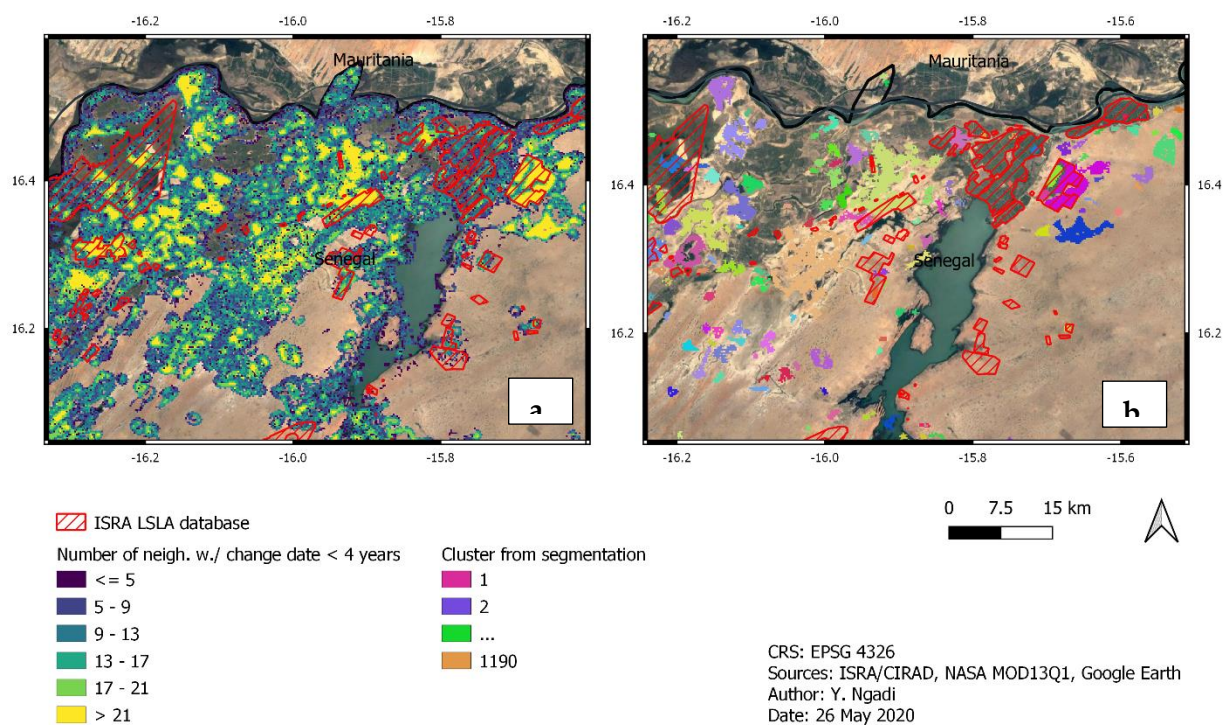


Figure 12: Delineation of MODIS date of change map clusters and map segmentation (a) Per pixel, number of neighbours in a 5x5 sliding window with a similar date of change (less than 4 years of difference). The sliding window applied allows to infer MODIS clusters' edges, needed for further image segmentation (Refer to section 3.2.4 for more details). (b) MODIS pixel clusters obtained when applying the Watershed segmentation to the image shown in subplot a).

Around 5% of the LSLAs were 'lost' during the process of segmentation (i.e. do not overlap any pixel of the newly formed clusters). After the whole process of detection and segmentation, and as mentioned above, only the largest LSLAs remained for detection with a median area of 123 ha (see **Table 3**). An additional aspect analysed, was the distribution of the extracted clusters along the latitude coordinates in order to see if BFAST introduced any bias with respect to climatic conditions. From **Table 4**, one can note that no bias with respect to the coordinates was introduced.

Table 4: Spatial statistics on the clusters extracted from the MODIS-based date of change map

	MODIS extracted clusters (n=1190)				Study area			
	mean	std	min	max	mean	std	min	max
Latitude (°)	15.65	0.59	14.50	16.69	15.54	0.65	14.495	16.639
Longitude (°)	-14.98	1.16	-17.36	-12.44	-15.13	1.45	-17.473	-12.226
Area (ha)	419.04	1006.36	62.5	13856.25				

4.1.4 Key findings of the processes including MODIS NDVI change detection and image segmentation

So far, we identified a total of 1190 clusters of MODIS pixels that present an abrupt change within their NDVI temporal series, and for which the NDVI trend is significantly positive. We found that 279 LSLAs out of 492 (56.7 %) overlap at least one of the extracted MODIS cluster. In addition, we found that the remaining LSLAs potentially detectable (i.e. that overlap at least one of the clusters pixels) have an estimated median area of 123 ha, which is significantly larger than those which do not overlap any of the detected clusters (2.4 ha). Amongst the different processes (NDVI trend filtering, BFAST change detection and change map segmentation) the most decisive one was the MODIS pixels masking based on the NDVI trend, as seen in the first column of **Table 3**. During this first process, 42.9% of the total number of deals (492) present in the study were not retained for further analysis.

4.2 LANDSCAPE FEATURES EXTRACTION BASED ON LANDSAT8 IMAGES

Results presented in this section are directly related to sub-objective 2: *“Discriminate detected potential agricultural LSLAs from other spatial processes (e.g.: agglomerated smallholder farms, LSLAs for conservation purposes...) using higher resolution satellite imagery (Landsat 8 - 30m)”*

4.2.1 Landsat8 images segmentation

The next step consisted in performing an object-based image analysis (OBIA) using Landsat 8 higher spatial resolution imagery (refer to section 3.3.2.). The aim pursued was the extraction of meaningful *groups* of landscape objects (e.g. parcels of fields instead of individual fields) from Landsat 8 imagery. The major drawback of this approach is its sensitivity to some of the different segmentation's parameters.

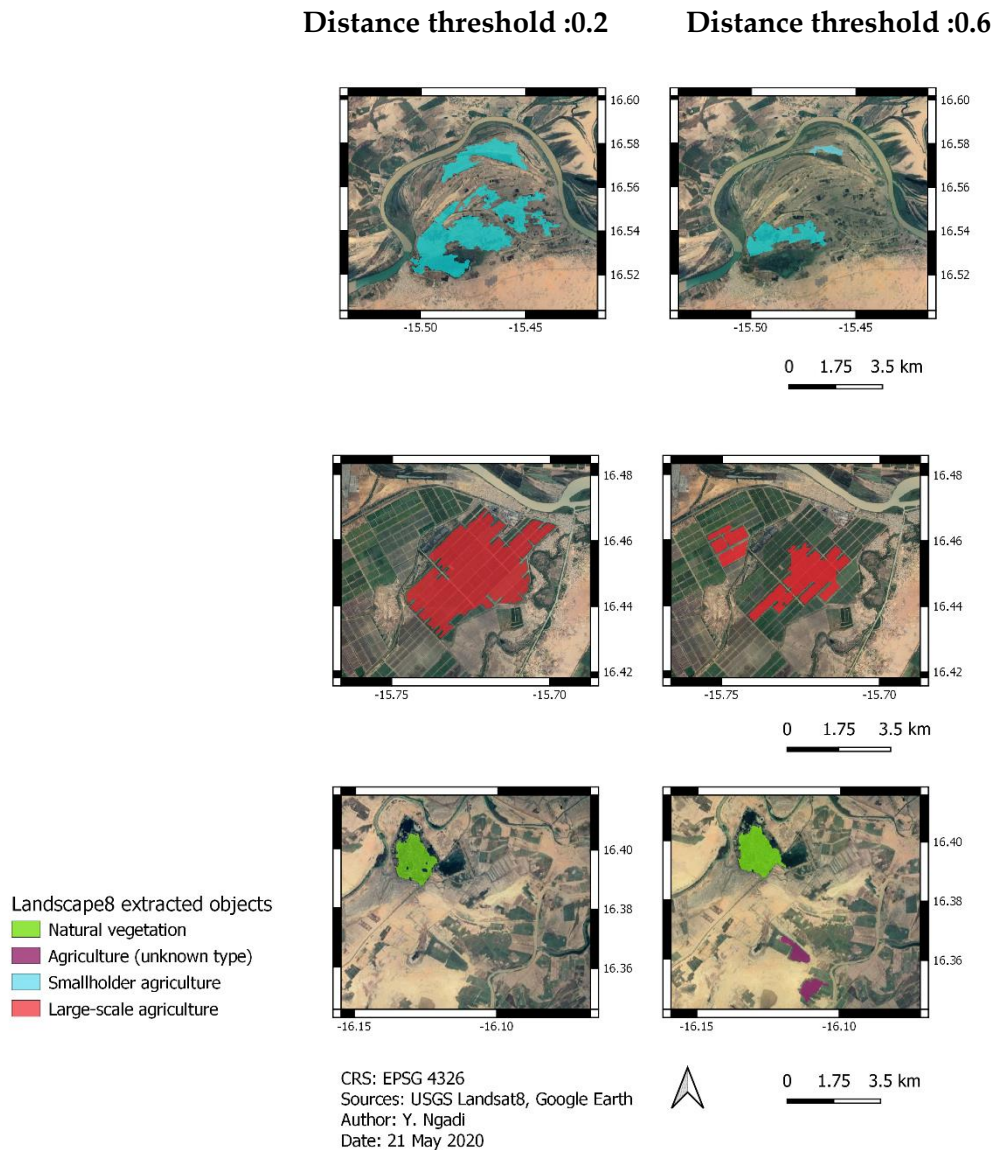


Figure 13: Example of extracted landscape objects from Landsat 8 images using two different distance thresholds: 0.2 (first column), and 0.6 (second column) for three study cases. Here Landsat object's labelling was visually performed using Google Earth imagery, the field database metadata, and one study related to land cover in Senegal (*Tappan et al., 2004*). Objects in blue are related to smallholder agriculture. Objects in red are related to large-scale agriculture. Objects in green are related to natural vegetation. Objects in purple are related to agriculture of undefined type. From this figure, we assessed the impact of distance threshold on the shape and size of the extracted objects.

From **figure 13** one can see that the distance thresholding (refer to section 3.3.2) chosen for the segmentation has a great impact on the size and shape of the objects extracted. As an example, the shape complexity of the objects that by visual inspection (refer to the legend of **figure 13** for more details) may be related to smallholder agriculture (in blue) is lower when using a higher distance threshold (0.6 instead of 0.2). At the opposite, with a higher distance threshold,

the shape complexity of agricultural LSLAs (illustrated in red) increases. By contrast, the shape of natural vegetation's object (in green) and individual parcels (in purple) does not seem to change much.

In the next section, the unsupervised classifications of the Landsat object-based extracted features (see subsection 3.3.3) are presented.

4.3 UNSUPERVISED CLASSIFICATION

4.3.1 SOM training

A total of 12 SOM maps were trained, resulting from the combination of different distance thresholds [0.2, 0.6], different windows sizes for the textures [5x5, 10x10, 15x15] and including or not the landscape shape index. The different parameters used (SOM size, learning rate, sigma), and the quantification errors (Qe) and topological errors (Te) achieved for the different trained maps are presented in **Table 5**. The Hopkins score for each dataset is given, estimating the randomness of the data (the lower, the less random) (refer to section 3.5.2 for more details).

Table 5: SOMs parameter settings

Distance threshold	Without landscape shape index						With landscape shape index					
	0.2 (n= 1388)			0.6 (n=606)			0.2 (n= 1388)			0.6 (n=606)		
	5	10	15	5	10	15	5	10	15	5	10	15
Window size												
Hopkins score	0.02	0.020	0.021	0.04	0.04	0.04	0.027	0.027	0.028	0.054	0.053	0.054
SOM size	14 x 13	15x12	16x11	12x10	11x10	12x10	14x13	14x13	14x12	14x8	11x10	11x10
learning rate (l)	0.38	0.36	0.46	0.46	0.46	0.36	0.54	0.36	0.44	0.34	0.38	0.36
Sigma (s)	1.1	1.12	1.16	1.02	1.0	1.06	1.12	1.18	1.16	0.98	1.08	1.14
Qe	0.24	0.2	0.21	0.15	0.17	0.21	0.21	0.26	0.29	0.17	0.22	0.22
Te	0.07	0.05	0.07	0.08	0.09	0.06	0.1	0.08	0.09	0.05	0.07	0.06

At a first sight, the parametrization and errors achieved are robust to the different input dataset used as no biggest variation may be observed. The differences in the SOM training performance between one dataset and the other are very small. The distance threshold seems to have a slightly higher impact than the window's size on the internal data structure (as seen by the slightly higher Hopkins scores and lower Qe). The topological errors achieved are small enough, indicating data topology preservation (less than 1% of the samples have their 1st and 2nd BMU not adjacent in the map).

Illustration of the SOM maps are presented in the next section, achieved on the dataset with a distance threshold of 0.2, a window size of 15x15 and including the Landscape shape index. The SOM maps obtained with the other datasets are presented in Appendices B to M.

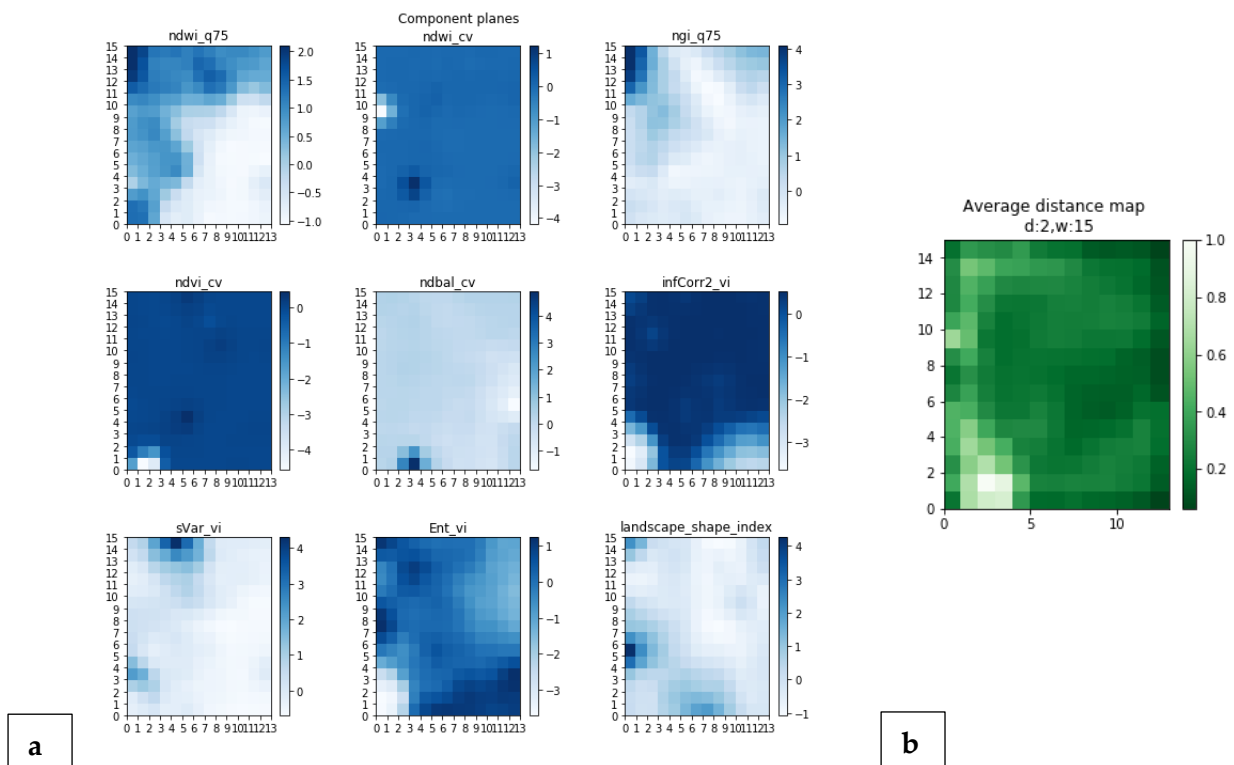


Figure 14: Illustration of the SOM maps obtained with the following input dataset: {distance=0.2, window size=15x15, shape_index included}. a) The component planes illustrate the relative distribution of each scaled feature over the map b) The average distance map indicates the average distance between the SOM nodes in the feature dimensional space.

Figure 14a shows the component planes, which represent the relative distribution of each scaled feature over the SOM grid. They can be thought of as a sliced version of the SOM. Dark blue values represent relatively high values of the (scaled) feature while white values represent low values. The numbers in the x and y axis represent the SOM nodes indexing. By comparing different component planes, correlations can be inferred. In addition, these maps allow to assess the variability of each feature, and its contribution to the distance map presented in **figure 14b** and explained below. A complementary map to the component planes allowing to visualize the cluster tendency of our data is the average distance map presented in **figure 14b**. It represents the (normalized) average distance of the nodes' weights in the input data dimension space. The whiter the colour is, the farther apart are the grid nodes from their neighbours. At the opposite, areas of high density will appear darker in the average distance map. Different compacted regions of the map, separated by whiter map units, will then likely represent natural clusters of the data. By comparing this map to the component planes, it is possible to assess which features contribute the most to the cluster tendency of the data.

In this specific case, one can see that the features with the greatest variability across the map (and more useful as they convey more information) are the VIs quantiles (particularly the NDWI), the entropy and the information measure of correlation 2. The shape index did not have a great impact on the average distance map. The VIs coefficient of variation was mostly homogeneous and had only very specific local contribution to the map. Around four homogeneous regions can be discerned in **figure 14b**. The region in the top left corner, mostly shaped by very high VIs values, is possibly linked to agricultural LSLAs, and will be visually evaluated in section 4.4.3. Indeed, and as noted in section 2.1.2, agricultural LSLAs often practice an intensive agriculture which translates into a higher biomass productivity. We can then expect the cluster related to agricultural LSLAs to contain very high VIs values.

4.3.2 SOM hierarchical clustering

In this study, the number of clusters was selected based on the Silhouette average value computed for different number of cluster k between 2 and 20 (see section 3.4.3).

Using the same input set as the previous section, the highest Silhouette average value was achieved for $k=8$ (see **figure 15**). The trained SOM map was then clustered into 8 partitions using an agglomerative clustering algorithm. The partition achieved is presented in **figure 16b**.

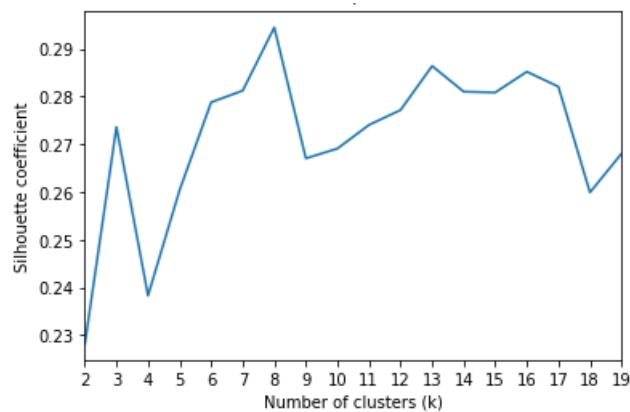


Figure 15: Plot of the Silhouette average values for different SOM partitions ($k = \{2, 3, \dots, 20\}$). Maximum was achieved for $k=8$.

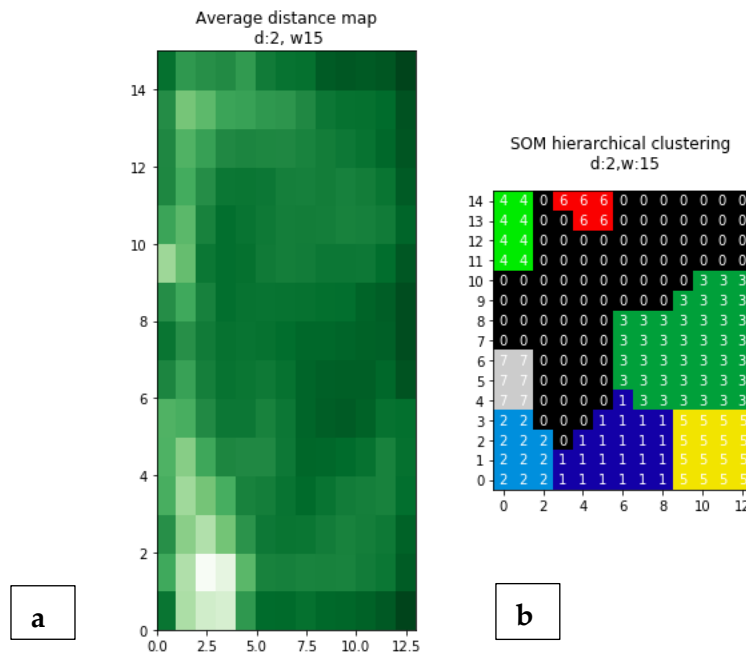


Figure 16: Clustered SOM a) SOM average distance map (refer to previous section. b): Partitionning of the SOM map using an agglomerative clustering algorithm (k=8)

In **figure 16b** each coloured area of the map represents a cluster of SOM nodes. As expected, the different clusters follow the density map presented in **figure 16a** (same as 14(b)). Combined with the information presented in the component planes of **figure 14a**, one can infer the most contributing features to the clustering. Most contributing features are here: the NDWI 75th quantile, the entropy and the information measure of correlation 2.

Cluster 4 is mostly defined by the very high VIs values, which as indicated above may be indicative of agricultural LSLAs. **Indeed, and making the same assumptions that other authors did (Yan et al., 2014), we expected LSLAs intensive agriculture to translate into high biomass productivity (i.e. high VIs values).** Cluster 0 is mainly defined by medium to high VIs quantiles, but also medium entropy values. Very low NDWI values, associated to dry environmental conditions, define clusters 1, 3 and 5. The only cluster highly influenced by the shape index is cluster 7, which represents objects with the highest shape complexity. Finally, cluster 2, represents the only area in the map in which NDWI and NGI are negatively correlated.

4.4 EVALUATION

4.4.1 Inter and intra-cluster variability

Besides the Silhouette average, the separation and cohesion of each cluster were individually assessed using a silhouette analysis presented in **figure 17**. The plot displays a measure of how close each sample in one cluster is to samples in the neighbouring cluster. Silhouette coefficients near +1 indicate that the sample is far away from the neighbouring clusters. A

value of 0 indicates that the sample is on or very close to the decision boundary between two neighbouring clusters and negative values indicate that those samples might have been assigned to the wrong cluster.

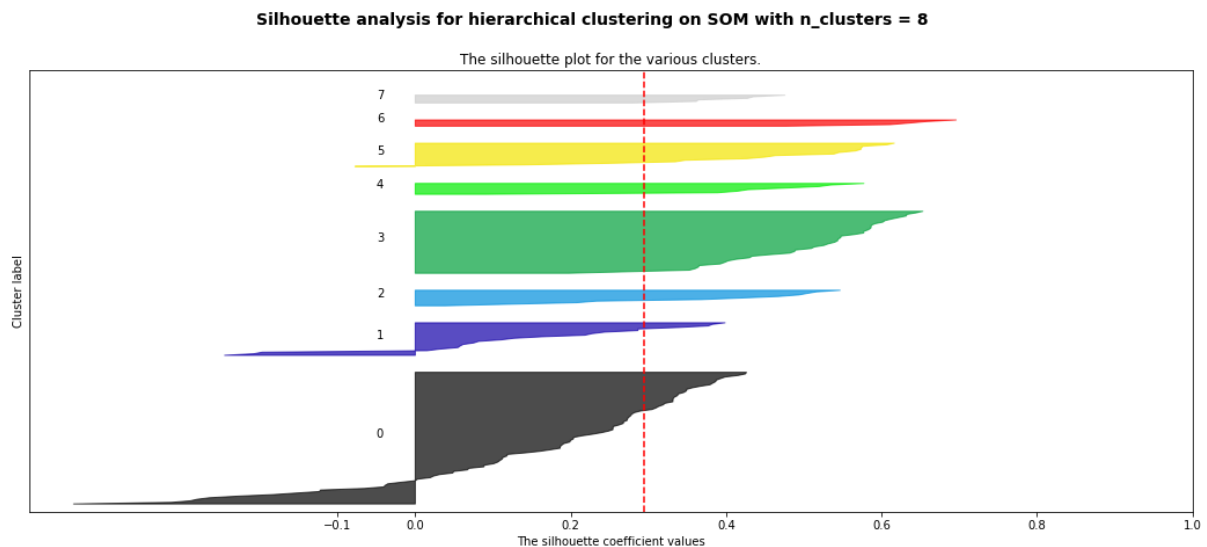


Figure 17: Clustered SOM Silhouette analysis for the partition of figure 16b. Each cluster of the partition is represented by a different color. The x-axis indicates the Silhouette coefficient value, allowing to assess the cohesion and separation of each cluster. The vertical red dashed line indicates the average achieved for all the partition.

In addition, the width of each cluster indicates the number of samples (SOM nodes) in within. From **figure 17**, one can see that the bulk of the SOM nodes belong to clusters 0 and 3. Cluster 0, which is the biggest is also the less well defined in terms of cohesion and separation (silhouette average <0.2). This cluster is mainly defined by medium VIs and entropy values. Cluster 3 is on another hand better defined that cluster 0 (coefficient average value >0.4). This cluster is representative of medium entropy values and low VIs values. The other clusters, with exception of cluster 1, achieve good Silhouette average values (>0.4) and are clusters 3,4-7. While well defined, those clusters are however very ‘thin’, indicating they are highly specific to a certain type of landscape element.

4.4.2 Accuracy, precision and recall

In this section, external evaluation metrics (against reference LSLAs) are presented. As a reminder, the SOM nodes were clustered within eight clusters. Knowing the BMU of each input data sample (Landsat pixel), it was possible to assign one cluster to each input data sample. Because the pixels belonging to one object are spectrally similar, the cluster assigned to each pixel of one object was almost all the time the same. There was no need to perform any majority filter in order to determine the Landsat object cluster.

The true positives, true negatives and false negatives were computed following the formulas given in section 3.5.2 and always relative to cluster 4 (possibly linked to agricultural LSLAs,

refer to section 4.3.2). A true positive was considered when one pixel minimum of the Landsat object (raster), classified as belonging to cluster 4, overlapped with at least one pixel one reference LSLA. A true negative was considered when no pixel overlapped any reference LSLA. And false negatives were considered when Landsat objects classified within any other cluster than cluster 4, overlapped with at least one pixel a reference LSLA.

Table 6 presents the accuracy (F1-score, refer to section 3.5.2), precision, recall of achieved by the different trained classifiers and relative to cluster 4 only.

Table 6: Unsupervised classifiers overall performance. The F1-score, Precision and Recall are relative to cluster 4 (the most possibly linked to agricultural LSLAs, see section 4.3.2)

Distance threshold Window size	Without landscape shape metrics						With landscape shape_index					
	0.2 (n= 1388)			0.6 (n=606)			0.2 (n= 1388)			0.6 (n=606)		
	5	10	15	5	10	15	5	10	15	5	10	15
Best silhouette average (k=[2,...,10])	0.35	0.32	0.31	0.32	0.33	0.29	0.26	0.3	0.29	0.29	0.31	0.26
Optimal number of clusters (k)	10	11	7	6	6	5	14	9	8	5	12	6
F1-score	0.36	0.33	0.42	0.28	0.25	0.28	0.375	0.33	0.43	0.27	0.22	0.22
Precision	0.95	0.94	0.84	0.18	0.15	0.18	0.95	0.67	0.82	0.93	0.93	0.13
Recall	0.23	0.2	0.28	0.62	0.7	0.62	0.23	0.22	0.29	0.16	0.12	0.68

Results in **Table 6** indicate that the highest overall performance (i.e. the balance between precision and recall) is achieved for a window size of 15x15 and a distance threshold of 0.2 for both input datasets (F1=0.43, with and without the landscape metric). With this parametrization, the precision of the classifier is optimized (0.82) with respect to its robustness (recall=0.29). Recall indicates that only 29% of the true positives are actually detected. However, its high precision level indicates that 82% of the detections are correct.

Results presented in **Table 6** also indicates that the worst window size was 10x10 with respect to sizes of 5x5 and 15x 15. The distance threshold has a great impact on the classifier precision and recall: the highest recall (but low precision) are achieved with a distance threshold of 0.6.

Figure 18 here below indicates for this specific classifier the classes distribution of the Landsat objects that overlap with at least one pixel the reported LSLAs (from the ground-truth database).

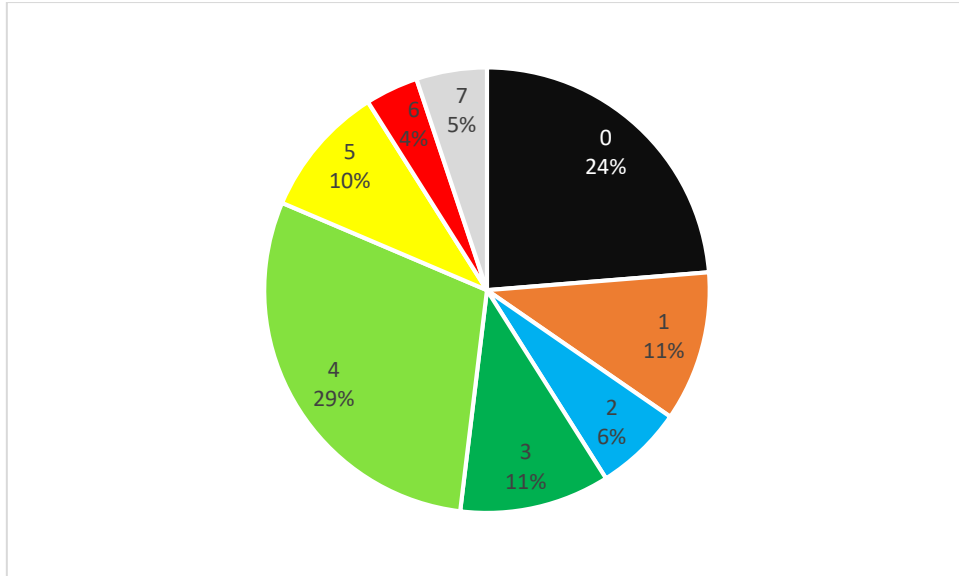


Figure 18: Distribution (%) of the classified Landsat object (raster) that overlap, with at least one pixel, one of the LSLAs reported in the ISRA/CIRAD database

As one can see in **figure 18**, around one half of the Landsat objects that overlap with at least one pixel one of the reported LSLAs, were classified as belonging to clusters 4 (29%) and 0 (24%). Those clusters are defined by medium to high VIs quantiles (refer to **figure 16b** and **figure 14a**). At the opposite, one third of the objects were classified within clusters characterized by very low VIs values but differing in their textural values (clusters 1 (11%), 3 (11%) and 5 (10%)) (refer to **figure 16b** and **figure 14a**).

4.4.3 Visual evaluation

In addition to the quantitative assessments previously performed, a qualitative assessment of the labelled Landsat objects was also performed. Objects belonging to the most relevant classes (clusters 0, 4, 6, 1 2 and 5), were inspected and are presented in **figure 19**.

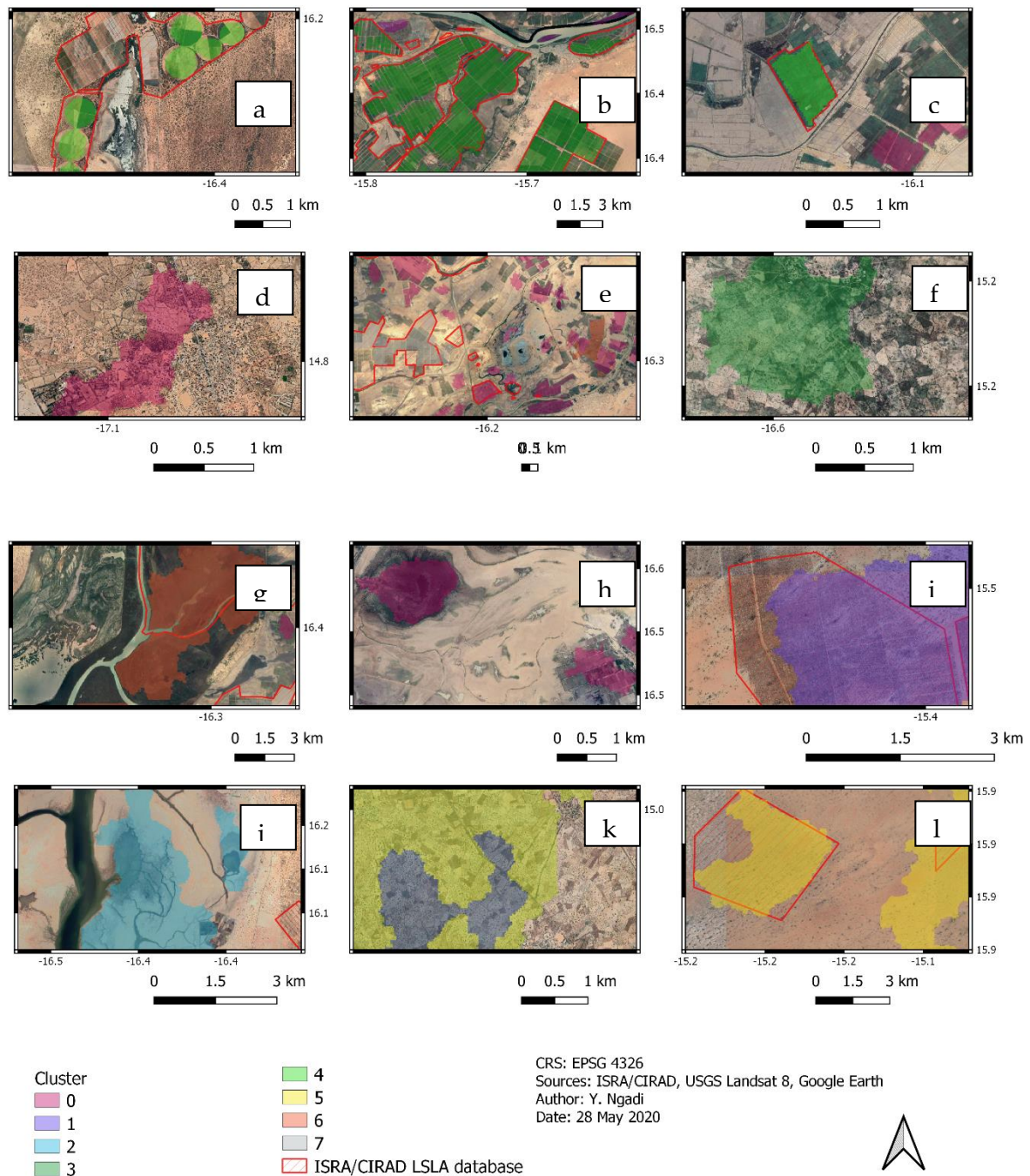


Figure 19: Closer views to different Landsat 8 classified objects (raster). a) agr. LSLA (SCL, vegetables), b) agr. LSLA (CSS, sugar cane), c) agr. LSLA (unknown production) d): smallholder agriculture (visual. determined), e) mix of smallholder agriculture (visual. determined) and LSLAs, f) fragmented agricultural landscape, g) wetlands (Djoudj Park), h) native vegetation spot and intensive agriculture (visual. determined), i) agr. LSLA (Azyla Gum, gum tree), j) Senegal River floodplain, k) fragmented arid landscape, l) agr. LSLA (Azyla Gum, gum tree)

As expected from the different quantitative results, some of the most representative of the reported LSLAs are classified as belonging to cluster number 4 (**figures 19 (a-c)**). As a reminder, 82% of the objects in cluster 4 (refer to the precision value achieved indicated in **Table 6**) were correctly labelled as LSLA. Notwithstanding false positives exist, as the one shown in **figure 19f**, still related to agricultural activities. As a reminder, only 29% of the true LSLA were detected within cluster 4 (**figures 19 (g, i, l)**). A non-negligible part (24%) was classified in cluster 0 (in red-purple, second row of figures), which is the cluster most likely related to smallholder agriculture. LSLAs characterized by low VIs values were mostly classified within cluster 1 and 5. Cluster 1 (violet) and cluster 5 (yellow) mostly differ in their textural correlation values. While objects in cluster 1 are highly correlated (gum tree plantation, **figure 19i**). Objects in cluster 5 are not correlated and are spatially independent, as illustrated by the fragmented landscapes shown in **figure 19k**, and the cluster without distinguishable objects of **figure 19l**.

5 DISCUSSION OF RESULTS

5.1.1 Land use/land cover change detection based on MODIS

The first part of this section is related to the change detection results. This study relies on two change detection algorithms, namely BFAST01 and BFAST. While being faster than BFAST (meaning more easily applicable over large spatial extents than BFAST), BFAST01 presented two main drawbacks, i.e.: over detection (one change detected for each MODIS pixel over the national territory, probably linked to the length of the temporal data) and sensitivity to climatic induced changes. In this study, the large majority of the dates of change detected by BFAST01 were comprised between 2004 and 2005 (see **figure 9**). The authors of a previous study conducted for the same study area and period of time (Ngadi et al., 2020), found a higher variability of the TRMM rainfall during the same period of time (2004-2005). As a consequence, the vast majority of breakpoints found by BFAST01 in this study are not suitable for our purpose. However, and as explained in section 3.2.2, the algorithm, which provide information on the trends observed before and after the breakpoint, was used to restrict the number of pixels for BFAST. The assumption made here is that a majority of new installations should translate in an increase of the biomass productivity and thus, should present a significant positive NDVI trend. However, while this may be true for new installations over non-cultivated/unproductive areas, such as the saline soils in the northern part of the country, or for installations in tropical areas involving land clearings, this is not always the case. This assumption restricts the number of potentially detectable LSLAs to 63.9% in the national territory, and 57.1% in our study case. Less number of LSLAs presents a significant positive NDVI trend in the northern part of the country than in the south (71%), where tropical conditions prevail. Another factor to take into account that may impact this proportion is the size of LSLAs. As retrieved from the database, an important part of the reported LSLAs (~25%) are smaller than 6ha, which is roughly the size of a MODIS pixel. As a consequence, their NDVI trend may be diluted in the pixel signal and not be detectable. The latter would in

addition explain the higher average area observed for the LSLAs with a positive NDVI trend (57 ha vs 30.8 ha, as shown in **Tables 3 and 2**).

It is also worth reminding that less than a half of the field database LSLAs in our study area are “active”, while around 9% are not active anymore or are not yet productive (see **Table 2**). The latter means that with the remaining 50% that have an unknown status, a non-negligible part of the reported LSLAs may not be detectable with a change detection algorithm.

The second processing step consisted in applying BFAST on a per-pixel basis, in order to detect relevant land use/land cover changes. The breakpoint associated to the biggest change in the median of the annual 16-day mean NDVI, as explained in section 3.2.3, was selected. This change detection, as opposed to the one detecting the biggest significant abrupt change in the time series trend component, does not include statistical significance tests. The obtained date of change map is much noisier and presents a higher variability than the one obtained using the breakpoint associated to the biggest significant trend change. The latter, similarly to BFAST01, detected a significant amount of change dates within the 2004-2005 period, likely related to climatic changes as explained above. This makes the map homogeneous, especially in the southern part of our study area, not suitable for a clustering process. At the opposite, and because of the higher spatial variability, more visual clusters were detected from the date of change map based on changes in the median of the annual 16-day mean NDVI, leading to the extraction of 1190 clusters. At this stage we suppose the presence of a high level of false-positives. But this not constitutes a problem per se as the discrimination between the different clusters is meant to be done during the unsupervised classification. However, needs for further research should definitely include the development of methods and metrics allowing to select the most suitable breakpoint. An important missing part here is the comparison of the number of potentially detectable LSLAs by BFAST (breakpoint selected using the different methods) and BFAST01. Unfortunately, time constraints imposed by a data loss incident impeded a quantitative assessment of this.

5.1.2 Landscape features extraction based on Landsat8 images

The most crucial processing step in our methodology concerns the Landsat 8 image segmentation (detailed in section 3.3.3). Indeed, the study heavily relies on the assumption that agricultural LSLAs present more geometrical shapes and less fragmented landscapes than smallholder agriculture and that shape indices could improve discrimination between those two land use systems. Two decisions had a big impact on the segmentation. The first one concerned the use of morphological operators in order to remove small holes between pixels identified as foreground pixels (markers) during the Otsu’s thresholding (example shown in **figure 7**). This was performed to enhance the extraction of *groups* of similar objects (e.g. groups of parcels). Indeed, without this image pre-processing step, small independent objects (such as individual parcels) were extracted, posing a twofold problem: 1) a loss of the object spatial context (does the parcel belong to an LSLA installation? Does it belong to a patch of smallholder agricultural parcels?), and 2) the impossibility to apply an object size filter in order to remove small objects improbably linked to agricultural LSLAs.

The second decision that had an impact on the object shape was the distance threshold level applied to the image's skeleton (illustrated in **figure 13**). The process was used to automatically extract foreground markers representative of vegetation needed by the segmentation algorithm. While lower distance thresholds allow to extract larger objects, higher distances produce smaller fragmented objects, constrained by the image edges. This parameter, however, seems to mostly impact the overall shape of complex objects such as the ones belonging to smallholder agricultural systems. Indeed, at higher threshold levels individual objects with more geometrical shapes are extracted. While this is also true for objects belonging to LSLAs, the overall shape of the group of objects stills conserve some simpler geometrical. As a consequence, in view of the overall performance of the different classifiers in **Table 6**, and the higher number of objects extracted at a lower distance threshold level (n=1308 vs n=606), lower distance thresholds are recommended. In addition, it is worthwhile to remember that the segmentation was performed on images resulting from the combination of very high VIs quantiles (90th). It is then very likely that with even low distance thresholds, identified foreground pixels are related to vegetated objects.

5.1.3 Unsupervised classification

The first aspect to consider is the composition of our input data (refer to section 3.4.1.). From our initial raw dataset containing different statistical metrics (25th, 50th, 75th quantiles and, coefficient of variation) on four VIs (NDVI, NDWI, NGI, NDBal), the thirteen Haralick textural features computed on NDVI images and two landscape shape metrics, we ended up with 9 low inter-correlated features. Indeed, high correlation (above 0.7) was found amongst the VIs features, the textural features and the two landscape shape metrics. However, the core input dataset shows a very low Hopkins index indicating a real cluster tendency. One important aspect to take into account when performing an unsupervised classification is the presence in the data of a real cluster tendency, as clustering algorithms are able to found clusters in random data as well. The VIs metrics kept include the 75th quantiles of NDWI and NGI. The NDBal, even if using a different spectral band (TIR), showed high correlation with NDWI. The latter is understandable as bare soils in the northern part of the country are mostly caused by the dry climatic conditions. However, in a tropical environment, this feature should be considered as a good candidate as it could add useful information to discriminate agricultural LSLAs.

Contribution of each feature to the clustering may be assessed by diving into the component planes and the clustered SOM map of **figures 14-15**. From **figures 14-15**, and as noted in section 4.3.1, the cluster most likely related to agricultural LSLAs (cluster 4) is almost uniquely defined by high VIs values. The latter poses a problem, as the whole agricultural LSLAs variability can difficultly be encompassed by a range of very high VIs values. As a consequence, the classifier will not have a high generalization performance in detecting agricultural LSLAs. In this study, we expected some textural metrics (more precisely "edges" textures such as the entropy) and/or the shape metric to contribute more largely to this cluster. Many authors have shown the complementarity of using textural features in addition to spectral metrics to improve separation between different image objects (Bey et al., 2020; Ferro et al., 2002; Lebourgeois et al., 2017). This is only true if the window size used to compute the

textural metrics is appropriate to the size and spacing of the texture elements within the class of interest. The window size should encompass the within-class variability, and that is a real challenge to achieve with complex land use systems such as agricultural LSLAs. However, when considering the overall performance of the different trained classifiers presented in **Table 6**, one can see that the input datasets using windows sizes of 5x5 and 15x15 achieved comparable performance, while the worst performance was achieved with a window size of 10x10. The latter suggests that instead of looking for one window size, further research may focus on finding the best combination of different windows sizes. Different window sizes may be a good solution to capture the texture variability at different scales (e.g. at the parcel level which comprises many fields, or at the LSLA installation level, which comprises many parcels). Because large window sizes gives stable measures of within-class textures (Ferro et al., 2002), and because we are working on extracted landscape objects, larger windows sizes than 15x15 could be tested in further research.

Having said that, we can see that the entropy in this study still contributes to some extent to the formation of cluster 0, the cluster most likely related to smallholder agriculture as suggested by **figures 19d-e**, and by its VIs and entropy values. This texture combined with the correlation texture allows on another hand to discriminate some natural vegetation elements, such as what seems to be flood plains and wetlands in northern Senegal (**figures 19j-g**). Amongst the textures, the variance was the less discriminative feature. It mostly determine cluster 6, which seems to be related to flooded areas, and could even include some specific crops such as flooded rice (**figure 19g**).

5.1.4 Evaluation of the classifiers discriminatory power and insights in agricultural LSLAs

The unsupervised classifier highest overall performance (F1-score=0.43) was achieved for the input sets using a distance threshold of 0.2, a window size of 15x15 and including the Landscape shape metric. More precisely, the precisions achieved for this combination of window size and distance threshold were very high (>0.9), while the recalls were very low (<0.2). This unsupervised classifier, while not robust, may however detect with high accuracy a small number of LSLAs (the ones with the highest VIs, which actually correspond to 1/3 of all the 'detected' LSLAs (i.e. the LSLAs that overlap at least one pixel of the extracted Landsat objects). The opposite is true for input datasets using a distance threshold=0.6. This contrast is particularly striking in the input dataset that does not include any shape metric. As previously mentioned, the distance threshold modifies the size and the shape of the object extracted. Because the contrasting input dataset did not include any landscape shape metric, the only parameter that could impact the classifier recall was the object's size, which in turn impacts the robustness of the textural metrics computed.

Besides the overall performance assessment, the methodology was found to be biased towards larger LSLAs. The size bias observed (well before the size filter applied at the end of the segmentation, as shown in **Table 3**) is explained by 2 processes: 1) the use of medium spatial resolution imagery (MODIS) to detect potential spatial changes and 2) the reliance of the change map segmentation process on the number of neighbouring pixels with similar dates of change. The latter favours the detection of bigger clusters of change.

Finally, despite the fact of not having enough discriminative features, evaluation of the discriminatory power of the different unsupervised classifiers against the ground truth database gave some insights in LSLAs. To begin with, the plot of **figure 18** indicates that one third of the 'detected' LSLAs are characterized by very high levels of biomass productivity, while 1/4 have an 'average' productivity. The latter does not necessarily reflect a difference in production intensity, but may just be a consequence of the type of crop cultivated. More interestingly is the fact that about one third of the reported LSLAs have very low VIs values. This may be a consequence of their inactivity, but also, as suggested by **figure 19i**, may be related to some kind of agroforestry.

5.2 SIGNIFICANCE AND REFLECTION ABOUT THE RESULTS

This study aimed to develop a generic classifier able to detect agricultural LSLAs at large spatial extents. So far, few studies have attempted to do so. Most of the studies aiming to characterize agricultural LSLAs have focused on specific agricultural crops (Hurni et al., 2017) or have based their research on different study cases (Bey et al., 2020), relying on supervised approaches most of the time (Bey et al., 2020; Graesser et al., 2017; Hurni et al., 2017). The latter does not come without limitations as the availability of a ground truth dataset for an area of interest is not always guaranteed, or is not always up to date, or may be incomplete. All of this represents important limitations to the detection of dynamic, fast and non-transparent processes such as LSLAs.

So far, and to our best knowledge, only one study used a change detection algorithm combined with a time series analysis (to estimate time series modality) to assess land use system conversions (Hentze et al., 2017). However, the study area was restricted to a specific agro-ecological zone, and a crop and land tenure masks were applied to focus on particular areas of interest. In a recent study, Bey et al. (2020) were able to detect smallholder and large-scale croplands based on Landsat spectral and textural features. Their methodology is based on a 2-level supervised approach in order to first discriminate vegetated classes from cropland, and then large-scale croplands from smallholder ones. Both studies, because supervised, are somehow restricted to the availability and quality of the ground truth labelled data, reducing this way the genericity of the methodology. Unsupervised classifiers, able to capture and analyse the full range of land use spectral and spatial signatures of the data have not yet been tested in the specific case of agricultural LSLAs' detection.

Because of its novel aspect, the data driven approach applied in the present study is worth of interest. Results obtained during this exploratory research, even if premature, are promising and provide some insights in agricultural LSLAs in the northern half of Senegal. With a very limited number of discriminative features, detection of a specific type of agricultural LSLAs was achieved with high precision. A major limitation so far is that the LSLA class is mostly defined by the high values of two VIs, compromising the robustness of the classifier, as VIs may not encompass alone the natural variability of LSLAs, and limiting the classifier performance over tropical areas. However, what is more interesting is that a significant

proportion of LSLAs were classified in a class related to smallholder agriculture, in which textural features appear to have more weight. A good selection of textural features, and more importantly of window sizes, may be very useful in improving discrimination between different land use systems. An unexpected result of this study, was the very low discriminative power of landscape shape metrics. This is very likely related to the process of image segmentation. Different parameters were found to have a great impact on the shape of the segmented objects. However, we do still believe that these metrics may greatly contribute to the discrimination of agricultural LSLAs. More research focused on the image segmentation applied to this kind of landscape elements is needed. Finally, this study shown the usefulness of using exploratory tools such as the SOMs in order to gain some insights in agricultural LSLAs.

6 CONCLUSIONS AND RECOMMENDATIONS

6.1 MAIN FINDINGS

This study presented a two-level unsupervised methodology to detect and characterize LSLAs in the northern half of Senegal. Several assumptions were made: 1) agricultural LSLAs may induce detectable changes in MODIS temporal series, and often present significant positive NDVI trends 2), spatial clusters of pixels with similar dates of change are affected by the same underlying change event, and 3) spatio-temporal spectral and textural metrics computed at the landscape level, combined with object shape metrics may allow to discriminate between natural vegetation, smallholder croplands and large-scale croplands. In order to apply the methodology, three core datasets were used: 1) a dense temporal stack (2000-2018) of MODIS 16-day composite NDVI for the change detection analysis, 2) multiple 2-year period of Landsat-8 images for the GEOBIA analysis and 3) a ground truth database on LSLAs in Senegal for the evaluation analysis.

The most important findings of the study are summarized here below:

- More than a half (63.9%) of the reported LSLAs do present a significant positive (MODIS) NDVI trend (in an undetermined fraction of their area). The proportion in the northern half part of the country is 57.1% while it represents 71% of the LSLAs reported in the south, where tropical conditions prevail.
- The BFAST algorithm is able to detect changes related to agricultural LSLAs. At the end of the process 56.7% of the reference LSLAs reported in the field database were potentially detectable. Around a third of those LSLAs are characterized by low VIs (NDWI and NGI) values. Nearly one-third are characterized by very high VIs (NDWI and NGI) values and were classified as belonging to the cluster identified as being most likely related to agricultural LSLAs.

- Two Vegetation Indices (2-year period NDWI and NGI 75th quantiles) had the biggest contribution to the cluster tendency of the dataset (with 9 features, including the landscape shape metric). Those VIs, combined with two textural features (the 2-year average Entropy and the Information Measure of Correlation 2, had the biggest discriminative power between the following identified classes: natural vegetation, smallholder croplands and large-scale croplands.
- The overall performance of the unsupervised classifiers is highly impacted by the distance threshold used during the Landsat image segmentation, and the window size used to compute textural features. The precision of the classifier towards our cluster of interest (the most possibly linked to agricultural LSLAs) was high (>0.8), but with a low recall (<0.3). More discriminative features are needed in order to retrieve more meaningful clusters.
- The shape metric did not have a big contribution to the cluster tendency of the data. The latter is in big part explained by the segmentation approach applied.
- The detection method is biased towards bigger agricultural LSLAs mostly because of the MODIS-based change detection and the change of date map segmentation approaches.
- Self-Organizing Maps (SOM) are exploratory tools that may be successfully used to gain insights in land use systems such as agricultural LSLAs.

6.2 REFERENCE TO RESEARCH QUESTIONS/OBJECTIVES

At this stage, we are now able to answer the research questions posed at the beginning of the present study, in section 1.2.3.

Sub-objective 1: Detect potential agricultural LSLAs' installation automatically at regional scale using change detection algorithms and medium resolution satellite (MODIS 250m) temporal series

- *RQ 1.1: Which method allows discriminating climate-induced breakpoints in MODIS NDVI time series from "anthropogenic" ones?*

While we were not able to specifically separate climate-induced breakpoints from "anthropogenic" ones, we were able to 'skip' the biggest breakpoints detected and related to climatic events. To do so, we implemented breakpoint selection technique allowing to detect time series pattern change. Recommendations related to this point are given in the next section.

Sub-objective 2: Discriminate detected potential agricultural LSLAs from other spatial processes (e.g.: agglomerated smallholder farms, LSLAs for conservation purposes...) using higher resolution satellite imagery (Landsat 8)

- RQ 2.1: Which spatio-temporal characteristics of agricultural LSLAs are transferrable to indicators and spatial metrics that can be derived from satellite imagery?

Some of the spatio-temporal characteristics of agricultural LSLAs transferrable to remotely-sensed indicators are: 1) the practice of intensive agriculture leading to very high VIs 75th quantiles (NDWI and NGI), 2) the specific size and distribution of the elements within LSLAs' installations (fields, parcels) enabling the use of textural features (Entropy and the Information Measure of Correlation 2) and 3), the practice of mechanized agriculture, allowing the use of landscape shape metrics (Landscape shape index).

- RQ 2.2: Do the metrics of question 2.1 allow distinction between different type of agricultural LSLAs and environments?

The exploratory approach applied in this study showed the discriminative power of the VIs and textural features in differentiating between different landscape elements: natural vegetation, smallholder agriculture and large-scale agriculture.

- RQ 2.3: Is the proposed methodology suitable for automatically discriminate agricultural LSLAs at regional scale?

The methodology, as presented in this study, is still in an exploratory phase and needs different processing steps to be 'fine-tuned'. However, with the right segmentation parametrization, and a higher set of discriminative features, the approach may be upscaled. Major limitations to the upscaling are two-fold: 1) the performance of the change detection algorithm over tropical areas is unknown. Because of the higher and more constant VIs values, change detection may be more difficult. However, worth is to note that the methodology did not show any bias towards the latitudes coordinates, while encompassing different agroecological zones. 2) The second limitation is related to the BFAST change detection computational-expensive algorithm. It is because BFAST is computational expensive that we first applied a filter based on the MODIS NDVI trend, in order to restrict the number of 'candidate' pixels. Still, this first filtering process presents a non-negligible amount of false positives. Higher computational performances (and possibility of upscaling) could then be achieved by replacing the first pre-processing step by a more selective filtering approach.

6.3 RECOMMENDATIONS

Because of the novel aspect of the present study, many gaps need to be filled. Some of the most important needs are summarized here below (from most important to less):

- There is a need of additional discriminatory features. As shown in section 4.3, the cluster possibly related to agricultural LSLAs is mainly determined by only three of

the 9 selected features (namely NDWI, NGI and Entropy). With only three features it is very difficult to encompass the natural variability existing within agricultural LSLAs. Suggestions include: 1) testing different satellite image stack compositing methods, 2) testing different textural window size combinations, and 3) selecting new features related to environmental/climatic conditions.

- Directly related to the previous point, and in order to be able to successfully make use of landscape shape metrics, is the need of more research on image segmentation techniques allowing to extract meaningful groups of landscape objects. Special attention should be paid to the shape of the extracted objects.
- The accuracy of the detected date of change is crucial in this study. As a consequence, more research is needed on metrics allowing to select the breakpoint that best fit our purpose.
- As seen in the results of this study, a MODIS pixel filtering based on the productivity trend may result in high omission error. Alternatives to reduce the number of candidate MODIS pixels are needed, such as the use of stratified MODIS time series in order to filter croplands (Vintrou et al., 2012b).

7 REFERENCES

- Abel, C., Horion, S., Tagesson, T., Brandt, M., & Fensholt, R. (2019). Towards improved remote sensing based monitoring of dryland ecosystem functioning using sequential linear regression slopes (SeRGS). *Remote Sensing of Environment*, 224(February), 317–332. <https://doi.org/10.1016/j.rse.2019.02.010>
- Almeida, A. E. (2017). *Time Series Components and Breakpoints in Remote Sensing Image Analysis* [Universidade Estadual de Campinas]. <http://repositorio.unicamp.br/jspui/handle/REPOSIP/325344>
- Angel, M., García-n, A., & Cervantes, H. (2018). *International Journal of Production Economics A survey on the Software Project Scheduling Problem*. 202(August 2017), 145–161. <https://doi.org/10.1016/j.ijpe.2018.04.020>
- Arvor, D., Meirelles, M., Dubreuil, V., Bégué, A., & Shimabukuro, Y. E. (2012). Analyzing the agricultural transition in Mato Grosso, Brazil, using satellite-derived indices. *Applied Geography*, 32(2), 702–713. <https://doi.org/10.1016/j.apgeog.2011.08.007>
- Baker-Smith, K., & Attila, S. B. M. (2016). What is land grabbing? A critical review of existing definitions. In *Eco Ruralis*.
- Batterbury, S., & Ndi, F. (2018). Land-grabbing in Africa. In J. A. Binns, K. Lynch, & E. Nel (Eds.), *The Routledge Handbook of African Development*. Routledge.
- Bégué, A., Arvor, D., Bellon, B., Betbeder, J., de Abelleira, D., Ferraz, R. P. D., Lebourgeois, V., Lelong, C., Simões, M., & Verón, S. R. (2018). Remote sensing and cropping practices: A review. *Remote Sensing*, 10(1), 1–32. <https://doi.org/10.3390/rs10010099>
- Bégué, A., Arvor, D., Lelong, C., Vintrou, E., & Simoes, M. (2015). Agricultural systems studies using remote sensing. *Land Resources Monitoring, Modeling, and Mapping with Remote Sensing*, 113–130. <https://doi.org/10.1201/b19322>
- Bellón, B., Bégué, A., Seen, D. Lo, de Almeida, C. A., & Simões, M. (2017). A remote sensing approach for regional-scale mapping of agricultural land-use systems based on NDVI time series. *Remote Sensing*, 9(6), 1–17. <https://doi.org/10.3390/rs9060600>
- Beucher, S. (1992). The watershed transformation applied to image segmentation. *Scanning Microscopy-Supplement*, 299.
- Bey, A., Jetimane, J., Lisboa, S. N., Ribeiro, N., Siteo, A., & Meyfroidt, P. (2020). Mapping smallholder and large-scale cropland dynamics with a flexible classification system and pixel-based composites in an emerging frontier of Mozambique. *Remote Sensing of Environment*, 239(October 2018), 111611. <https://doi.org/10.1016/j.rse.2019.111611>
- Bisquert, M., Bégué, A., & Deshayes, M. (2015). Object-based delineation of homogeneous landscape units at regional scale based on modis time series. *International Journal of Applied Earth Observation and Geoinformation*, 37, 72–82. <https://doi.org/10.1016/j.jag.2014.10.004>
- Blaschke, T. (2010). Object based image analysis for remote sensing. In *ISPRS Journal of Photogrammetry and Remote Sensing* (Vol. 65, Issue 1, pp. 2–16). Elsevier B.V. <https://doi.org/10.1016/j.isprsjprs.2009.06.004>
- Blaschke, T., Hay, G. J., Kelly, M., Lang, S., Hofmann, P., Addink, E., Queiroz Feitosa, R., van der Meer, F., van der Werff, H., van Coillie, F., & Tiede, D. (2014). Geographic Object-Based Image Analysis - Towards a new paradigm. *ISPRS Journal of Photogrammetry and Remote Sensing*, 87, 180–191.

<https://doi.org/10.1016/j.isprsjprs.2013.09.014>

- Bosch, M. (2019). PyLandStats: An open-source Pythonic library to compute landscape metrics. *PLoS One*, 14(12).
- Brown, J. C., Jepson, W. E., Kastens, J. H., Wardlow, B. D., Lomas, J. M., & Price, K. P. (2007). Multitemporal, Moderate-Spatial-Resolution Remote Sensing of Modern Agricultural Production and Land Modification in the Brazilian Amazon. *GIScience & Remote Sensing*, 44(2), 117–148. <https://doi.org/10.2747/1548-1603.44.2.117>
- Cabanes, G., & Bennani, Y. (2007). A simultaneous two-level clustering algorithm for automatic model selection. *Sixth International Conference on Machine Learning and Applications (ICMLA 2007)*, 316–321.
- Chen, J., Jönsson, P., Tamura, M., Gu, Z., Matsushita, B., & Eklundh, L. (2004). A simple method for reconstructing a high-quality NDVI time-series data set based on the Savitzky–Golay filter. *Remote Sensing of Environment*, 91(3–4), 332–344.
- Chen, J., Shao, H., & Hu, C. (2018a). Image Segmentation Based on Mathematical Morphological Operator. In *Colorimetry and Image Processing*. InTech. <https://doi.org/10.5772/intechopen.72603>
- Chen, Y., Lu, D., Moran, E., Batistella, M., Dutra, L. V., Sanches, I. D. A., da Silva, R. F. B., Huang, J., Luiz, A. J. B., & de Oliveira, M. A. F. (2018b). Mapping croplands, cropping patterns, and crop types using MODIS time-series data. *International Journal of Applied Earth Observation and Geoinformation*, 69(November 2017), 133–147. <https://doi.org/10.1016/j.jag.2018.03.005>
- Coelho, L. P. (2012). Mahotas: Open source software for scriptable computer vision. *ArXiv Preprint ArXiv:1211.4907*.
- Cotula, L. (2012). The international political economy of the global land rush: A critical appraisal of trends, scale, geography and drivers. *The Journal of Peasant Studies*, 39(3–4), 649–680. <https://doi.org/10.1080/03066150.2012.674940>
- De Jong, R., & De Bruin, S. (2012). Linear trends in seasonal vegetation time series and the modifiable temporal unit problem. *Biogeosciences*, 9(1), 71–77. <https://doi.org/10.5194/bg-9-71-2012>
- De Ponteves, H. (2020). *Classification: precision and recall*. <https://developers.google.com/machine-learning/crash-course/classification/precision-and-recall>
- Debats, S. R., Luo, D., Estes, L. D., Fuchs, T. J., & Caylor, K. K. (2016). Remote Sensing of Environment A generalized computer vision approach to mapping crop fields in heterogeneous agricultural landscapes. *Remote Sensing of Environment*, 179, 210–221. <https://doi.org/10.1016/j.rse.2016.03.010>
- Evans, J., & Geerken, R. (2004). Discrimination between climate and human-induced dryland degradation. *Journal of Arid Environments*, 57(4), 535–554. [https://doi.org/10.1016/S0140-1963\(03\)00121-6](https://doi.org/10.1016/S0140-1963(03)00121-6)
- Fang, X., Zhu, Q., Ren, L., Chen, H., Wang, K., & Peng, C. (2018). Large-scale detection of vegetation dynamics and their potential drivers using MODIS images and BFAST: A case study in Quebec, Canada. *Remote Sensing of Environment*, 206(March 2016), 391–402. <https://doi.org/10.1016/j.rse.2017.11.017>
- Ferro, C. J. S., & Warner, T. A. (2002). Scale and texture in digital image classification. *Photogrammetric Engineering and Remote Sensing*, 68(1), 51–63.

- FIAN, A. O. (2010). *Land Grabbing in Kenya and Mozambique. A Report on Two Research Missions—and a Human Rights Analysis of Land Grabbing*. FIAN International Secretariat Heidelberg, Germany.
- Fisher, R., Perkins, S., Walker, A., & Wolfart, E. (2020). *Skeletonization/ Medial axis transform*. Image Processing Learning Resources. <http://homepages.inf.ed.ac.uk/rbf/HIPR2/skeleton.htm>
- Forkel, M., Carvalhais, N., Verbesselt, J., Mahecha, M. D., Neigh, C. S. R., & Reichstein, M. (2013). Trend Change detection in NDVI time series: Effects of inter-annual variability and methodology. *Remote Sensing*, 5(5), 2113–2144. <https://doi.org/10.3390/rs5052113>
- Frenken, K. (2005). *Irrigation in Africa in figures: AQUASTAT Survey, 2005* (Vol. 29). Food & Agriculture Org.
- Galford, G. L., Mustard, J. F., Melillo, J., Gendrin, A., Cerri, C. C., & Cerri, C. E. P. (2008). Wavelet analysis of MODIS time series to detect expansion and intensification of row-crop agriculture in Brazil. *Remote Sensing of Environment*, 112(2), 576–587. <https://doi.org/10.1016/j.rse.2007.05.017>
- Gao, B.-C. (1996). NDWI A Normalized Difference Water Index for remote sensing of vegetation liquid water from space. *Remote Sens. Environ*, 7212(April), 257–266.
- Gillanders, S. N., Coops, N. C., Wulder, M. A., Gergel, S. E., & Nelson, T. (2008). Multitemporal remote sensing of landscape dynamics and pattern change: describing natural and anthropogenic trends. *Progress in Physical Geography*, 32(5), 503–528.
- Gitelson, A. A., Gritz, Y., & Merzlyak, M. N. (2003). Relationships between leaf chlorophyll content and spectral reflectance and algorithms for non-destructive chlorophyll assessment in higher plant leaves. *Journal of Plant Physiology*, 160(3), 271–282.
- Graesser, J., & Ramankutty, N. (2017). Remote Sensing of Environment Detection of cropland field parcels from Landsat imagery ☆, ☆☆, ☆☆☆ *Remote Sensing of Environment*, 201(July), 165–180. <https://doi.org/10.1016/j.rse.2017.08.027>
- Graesser, J., Ramankutty, N., & Coomes, O. T. (2018). Increasing expansion of large-scale crop production onto deforested land in sub-Andean South America. *Environmental Research Letters*, 13(8). <https://doi.org/10.1088/1748-9326/aad5bf>
- Hall-Beyer, M. (2017). Practical guidelines for choosing GLCM textures to use in landscape classification tasks over a range of moderate spatial scales. *International Journal of Remote Sensing*, 38(5), 1312–1338. <https://doi.org/10.1080/01431161.2016.1278314>
- Haralick, R. M., Dinstein, I., & Shanmugam, K. (1973). Textural Features for Image Classification. *IEEE Transactions on Systems, Man and Cybernetics*, SMC-3(6), 610–621. <https://doi.org/10.1109/TSMC.1973.4309314>
- Harding, A., Chamberlain, W., Anseeuw, W., Manco, G., & Niassy, S. (2016). *Land Matrix Large Scale Land Acquisition Profile: Senegal*. Land Matrix.
- Hay, G. J., & Blaschke, T. (2010). Special issue: Geographic object-based image analysis (GEOBIA). *Photogrammetric Engineering and Remote Sensing*, 76(2), 121–122.
- Hentze, K., Thonfeld, F., & Menz, G. (2017). How a modified breakpoint analysis enhances knowledge of agricultural production after Zimbabwe ' s fast track land reform. *Int J Appl Earth Obs Geoinformation*, 62(July 2016), 78–87. <https://doi.org/10.1016/j.jag.2017.05.007>
- Hopkins, B., & Skellam, J. G. (1954). A new method for determining the type of distribution of plant individuals. *Annals of Botany*, 18(2), 213–227.

- Hurni, K., Schneider, A., Heinemann, A., Nong, D. H., & Fox, J. (2017). Mapping the expansion of boom crops in Mainland Southeast Asia using dense time stacks of landsat data. *Remote Sensing*, 9(4). <https://doi.org/10.3390/rs9040320>
- Jabar, A. S. A., Ibraheem, N. K., & Ahmed, N. T. (2019). Satellite images segmentation based on histogram and active contour algorithm. *Journal of Advanced Research in Dynamical and Control Systems*, 11(2), 494–505.
- Jain, M., Mondal, P., DeFries, R. S., Small, C., & Galford, G. L. (2013). Mapping cropping intensity of smallholder farms: A comparison of methods using multiple sensors. *Remote Sensing of Environment*, 134, 210–223. <https://doi.org/https://doi.org/10.1016/j.rse.2013.02.029>
- Jamali, S., Jönsson, P., Eklundh, L., Ardö, J., & Seaquist, J. (2015). Detecting changes in vegetation trends using time series segmentation. *Remote Sensing of Environment*, 156, 182–195. <https://doi.org/10.1016/j.rse.2014.09.010>
- Jamali, S., Seaquist, J., Eklundh, L., & Ardö, J. (2014). Automated mapping of vegetation trends with polynomials using NDVI imagery over the Sahel. *Remote Sensing of Environment*, 141, 79–89. <https://doi.org/10.1016/j.rse.2013.10.019>
- Kaag, M. M. A., & Zoomers, E. B. T. A.-T. T.-. (2014). *The global land grab : beyond the hype LK - https://utrechtuniversity.on.worldcat.org/oclc/871704920* (NV-1 o). Fernwood Publishing ; <http://site.ebrary.com/id/10835461>
- Kohonen, T. (2013). Essentials of the self-organizing map. *Neural Networks*, 37, 52–65.
- Kuemmerle, T., Erb, K., Meyfroidt, P., Mu, D., Verburg, P. H., Estel, S., Haberl, H., Hostert, P., Jepsen, M. R., Kastner, T., Levers, C., Lindner, M., Plutzer, C., Verkerk, P. J., Zanden, E. H. Van Der, & Reenberg, A. (2013). *Challenges and opportunities in mapping land use intensity globally*. 484–493. <https://doi.org/10.1016/j.cosust.2013.06.002>
- Kuemmerle, T., Hostert, P., St-Louis, V., & Radeloff, V. (2009). Using image texture to map farmland field size: A case study in Eastern Europe. *Journal of Land Use Science*, 4, 85–107. <https://doi.org/10.1080/17474230802648786>
- Kupidura, P. (2019). The comparison of different methods of texture analysis for their efficacy for land use classification in satellite imagery. *Remote Sensing*, 11(10). <https://doi.org/10.3390/rs11101233>
- Lambert, J., Denux, J. P., Verbesselt, J., Balent, G., & Cheret, V. (2015). Detecting clear-cuts and decreases in forest vitality using MODIS NDVI time series. *Remote Sensing*, 7(4), 3588–3612. <https://doi.org/10.3390/rs70403588>
- Lazarus, E. D. (2014). Land grabbing as a driver of environmental change. *Area*, 46(1), 74–82. <https://doi.org/10.1111/area.12072>
- Lebourgeois, V., Dupuy, S., Vintrou, É., Ameline, M., Butler, S., & Bégué, A. (2017). A combined random forest and OBIA classification scheme for mapping smallholder agriculture at different nomenclature levels using multisource data (simulated Sentinel-2 time series, VHRS and DEM). *Remote Sensing*, 9(3), 1–20. <https://doi.org/10.3390/rs9030259>
- Leroux, L., Bégué, A., Lo Seen, D., Jolivot, A., & Kayitakire, F. (2017). Driving forces of recent vegetation changes in the Sahel: Lessons learned from regional and local level analyses. *Remote Sensing of Environment*, 191, 38–54. <https://doi.org/10.1016/j.rse.2017.01.014>
- Lesiv, M., Carlos, J., Bayas, L., See, L., Duerauer, M., Bilous, A., Dahlia, D., Durando, N., Hazarika, R., Kumar, P., Volodymyr, V., Hoyos, A. P., Gengler, S., Prestele, R., Bilous, S., Karner, M., Narzary,

- W., Sturn, T., Mccallum, I., & Schepaschenko, D. (2019). *Estimating the global distribution of field size using crowdsourcing*. September 2018, 174–186. <https://doi.org/10.1111/gcb.14492>
- Li, R., Pun, M., & Mutiibwa, D. (2016). Classification of irrigated and non-irrigated cropland using object-based image analysis: A case study in south-central Nebraska. *2016 Fifth International Conference on Agro-Geoinformatics (Agro-Geoinformatics)*, 1–4. <https://doi.org/10.1109/Agro-Geoinformatics.2016.7577619>
- Linfoot, E. H. (1957). An informational measure of correlation. *Information and Control*, 1(1), 85–89. [https://doi.org/https://doi.org/10.1016/S0019-9958\(57\)90116-X](https://doi.org/https://doi.org/10.1016/S0019-9958(57)90116-X)
- Liu, Y., Li, Y., Li, S., & Motesharrei, S. (2015). Spatial and temporal patterns of global NDVI trends: Correlations with climate and human factors. *Remote Sensing*, 7(10), 13233–13250. <https://doi.org/10.3390/rs71013233>
- McGarigal, K. (2001). *Landscape Metrics for Categorical Map Patterns*. 2001(Chapter 5), 1–77.
- Messerli, P., Giger, M., Dwyer, M. B., Breu, T., & Eckert, S. (2014). The geography of large-scale land acquisitions: Analysing socio-ecological patterns of target contexts in the global South. *Applied Geography*, 53, 449–459. <https://doi.org/https://doi.org/10.1016/j.apgeog.2014.07.005>
- Ngadi, Y. (2020). *Automated processing of low resolution satellite image time series for detecting, dating & characterizing agro-industries installation in Senegal*.
- Osabuohien, E. S. (2014). Large-scale agricultural land investments and local institutions in Africa: The Nigerian case. *Land Use Policy*, 39, 155–165.
- Ozdogan, M., Yang, Y., Allez, G., & Cervantes, C. (2010). Remote sensing of irrigated agriculture: Opportunities and challenges. *Remote Sensing*, 2(9), 2274–2304.
- Pedregosa, F., Varoquaux, G., Gramfort, A., Michel, V., Thirion, B., Grisel, O., Blondel, M., Prettenhofer, P., Weiss, R., & Dubourg, V. (2011). Scikit-learn: Machine learning in Python. *The Journal of Machine Learning Research*, 12, 2825–2830.
- Petitjean, F., Kurtz, C., Passat, N., & Gançarski, P. (2012). Spatio-temporal reasoning for the classification of satellite image time series. *Pattern Recognition Letters*, 33(13), 1805–1815. <https://doi.org/10.1016/J.PATREC.2012.06.009>
- Pun, M. (2019). *Application of Remote Sensing Technology in Water Resources Management*. University of Nebraska-Lincoln. Lincoln Nebraska, USA.
- Ragetti, S., Herberz, T., & Siegfried, T. (2018). An unsupervised classification algorithm for multi-temporal irrigated area mapping in Central Asia. *Remote Sensing*, 10(11), 1–24. <https://doi.org/10.3390/rs10111823>
- Rousseeuw, P. J. (1987). Silhouettes: a graphical aid to the interpretation and validation of cluster analysis. *Journal of Computational and Applied Mathematics*, 20, 53–65.
- Roy, D. P., Wulder, M. A., Loveland, T. R., Woodcock, C. E., Allen, R. G., Anderson, M. C., Helder, D., Irons, J. R., Johnson, D. M., & Kennedy, R. (2014). Landsat-8: Science and product vision for terrestrial global change research. *Remote Sensing of Environment*, 145, 154–172. <https://doi.org/https://doi.org/10.1016/j.rse.2014.02.001>
- Schoneveld, G. C. (2011). The anatomy of large-scale farmland acquisitions in sub-Saharan Africa. *CIFOR Working Paper*, 85.
- Sparks, D. L. (2012). Large Scale Land Acquisitions In Sub-Saharan Africa: The New Scramble? *The*

International Business & Economics Research Journal (Online), 11(6), 687.

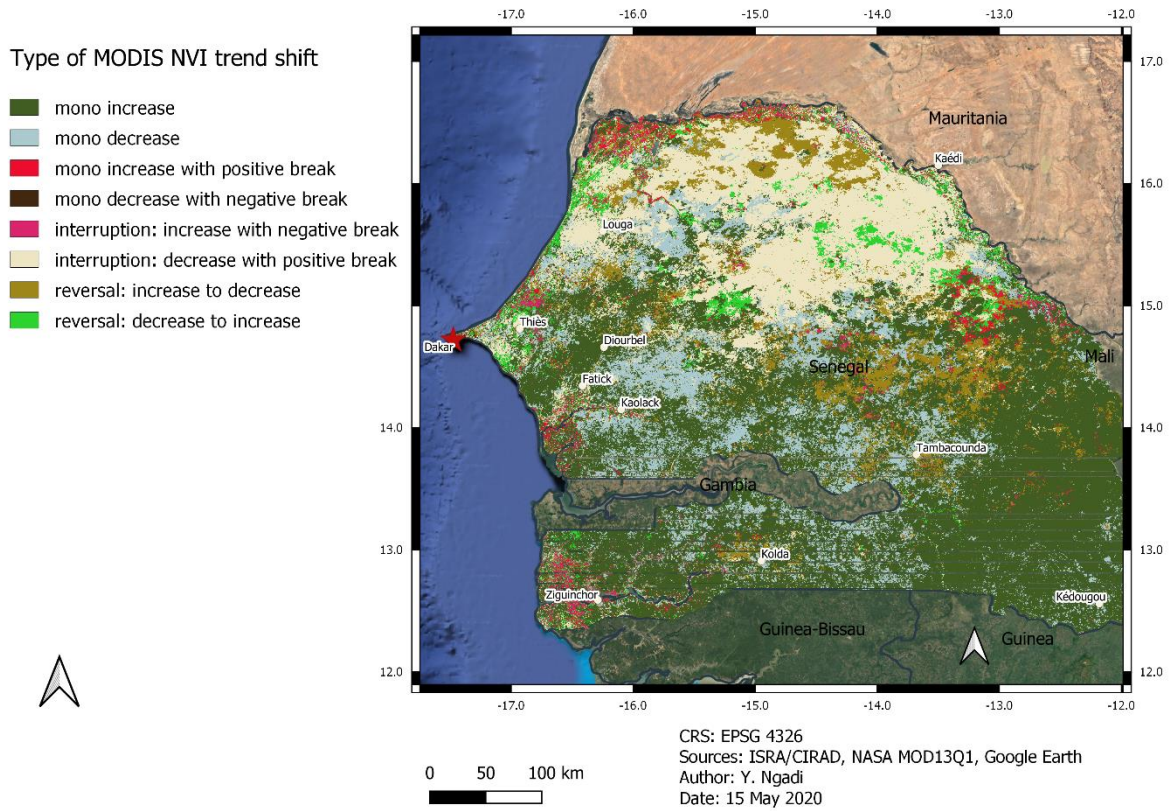
- Steege, J. A. Van De, Verburg, P. H., Baltenweck, I., & Staal, S. J. (2010). Characterization of the spatial distribution of farming systems in the Kenyan Highlands. *Applied Geography*, 30(2), 239–253. <https://doi.org/10.1016/j.apgeog.2009.05.005>
- Stefanski, J., Kuemmerle, T., Chaskovskyy, O., Griffiths, P., Havryluk, V., Knorn, J., Korol, N., Sieber, A., & Waske, B. (2014). Mapping land management regimes in western Ukraine using optical and SAR data. *Remote Sensing*, 6(6), 5279–5305. <https://doi.org/10.3390/rs6065279>
- Tappan, G. G., Sall, M., Wood, E. C., & Cushing, M. (2004). Ecoregions and land cover trends in Senegal. *Journal of Arid Environments*, 59(3), 427–462. <https://doi.org/https://doi.org/10.1016/j.jaridenv.2004.03.018>
- Thenkabail, P., GangadharaRao, P., Biggs, T., Krishna, M., & Turrall, H. (2007). Spectral matching techniques to determine historical land-use/land-cover (LULC) and irrigated areas using time-series 0.1-degree AVHRR pathfinder datasets. *Photogrammetric Engineering & Remote Sensing*, 73(10), 1029–1040.
- Timmermans, A. (2018). *Mapping cropland in smallholder farmer systems in South-Africa using Sentinel-2 imagery*. Université Catholique de Louvain (UCL). Belgium.
- Tomasi, C., & Manduchi, R. (1998). Bilateral filtering for gray and color images. *Sixth International Conference on Computer Vision (IEEE Cat. No. 98CH36271)*, 839–846.
- United States Geological Survey. (2020a). *Landsat Collection 1*. https://www.usgs.gov/land-resources/nli/landsat/landsat-collection-1?qt-science_support_page_related_con=1#qt-science_support_page_related_con
- United States Geological Survey. (2020b). *Using the USGS Landsat Level-1 data product*. <https://www.usgs.gov/land-resources/nli/landsat/using-usgs-landsat-level-1-data-product>
- Verbesselt, J., Hyndman, R., Newnham, G., & Culvenor, D. (2010a). Detecting trend and seasonal changes in satellite image time series. *Remote Sensing of Environment*, 114(1), 106–115. <https://doi.org/10.1016/j.rse.2009.08.014>
- Verbesselt, J., Hyndman, R., Newnham, G., & Culvenor, D. (2010b). Detecting trend and seasonal changes in satellite image time series. *Remote Sensing of Environment*, 114(1), 106–115. <https://doi.org/https://doi.org/10.1016/j.rse.2009.08.014>
- Verbesselt, J., Zeileis, A., & Hyndman, R. (2012). Breaks For Additive Season and Trend (BFAST). *Technical Report*. <http://bfast.r-forge.r-project.org/>
- Verburg, P. H., Steege, J. Van De, Veldkamp, A., & Willemen, L. (2009). From land cover change to land function dynamics: A major challenge to improve land characterization. *Journal of Environmental Management*, 90(3), 1327–1335. <https://doi.org/10.1016/j.jenvman.2008.08.005>
- Vesanto, J., & Alhoniemi, E. (2000a). Clustering of the self-organizing map. *IEEE Transactions on Neural Networks*, 11(3), 586–600.
- Vesanto, J., Himberg, J., Alhoniemi, E., & Parhankangas, J. (2000b). SOM toolbox for Matlab 5. *Helsinki University of Technology*, 216.
- Vesanto, J., Himberg, J., Alhoniemi, E., & Parhankangas, J. (1999). Self-organizing map in Matlab: the SOM Toolbox. *Proceedings of the Matlab DSP Conference*, 99, 16–17.

- Vettigli, G. (2018). *MiniSom: minimalistic and NumPy-based implementation of the Self Organizing Map*.(2018).
- Vintrou, E., Desbrosse, A., Bégué, A., Traoré, S., Baron, C., & Lo Seen, D. (2012a). Crop area mapping in West Africa using landscape stratification of MODIS time series and comparison with existing global land products. *International Journal of Applied Earth Observation and Geoinformation*, *14*(1), 83–93. <https://doi.org/10.1016/j.jag.2011.06.010>
- Vintrou, E., Soumaré, M., Bernard, S., Bégué, A., Baron, C., & Lo Seen, D. (2012b). Mapping fragmented agricultural systems in the sudano-sahelian environments of Africa using random forest and ensemble metrics of coarse resolution MODIS imagery. *Photogrammetric Engineering and Remote Sensing*, *78*(8), 839–848. <https://doi.org/10.14358/PERS.78.8.839>
- Vogels, M., de Jong, S., Sterk, G., & Addink, E. A. (2019a). Mapping irrigated agriculture in complex landscapes using SPOT6 imagery and object-based image analysis – A case study in the Central Rift Valley, Ethiopia –. *International Journal of Applied Earth Observation and Geoinformation*, *75*(May 2018), 118–129. <https://doi.org/10.1016/j.jag.2018.07.019>
- Vogels, M., de Jong, S., Sterk, G., Douma, H., & Addink, E. (2019b). Spatio-temporal patterns of smallholder irrigated agriculture in the horn of Africa using GEOBIA and Sentinel-2 imagery. *Remote Sensing*, *11*(2). <https://doi.org/10.3390/rs11020143>
- Waldner, F., & Diakogiannis, F. (2019). *Deep learning on edge: extracting field boundaries from satellite images with a convolutional neural network*. October.
- Wardlow, B. D., Egbert, S. L., & Kastens, J. H. (2007). Analysis of time-series MODIS 250 m vegetation index data for crop classification in the U.S. Central Great Plains. *Remote Sensing of Environment*, *108*(3), 290–310. <https://doi.org/10.1016/j.rse.2006.11.021>
- Watkins, B., & Niekerk, A. Van. (2019a). A comparison of object-based image analysis approaches for field boundary delineation using multi-temporal Sentinel-2 imagery. *Computers and Electronics in Agriculture*, *158*(February), 294–302. <https://doi.org/10.1016/j.compag.2019.02.009>
- Watkins, B., & Niekerk, A. Van. (2019b). Automating field boundary delineation with multi-temporal Sentinel-2 imagery. *Computers and Electronics in Agriculture*, *167*(October), 105078. <https://doi.org/10.1016/j.compag.2019.105078>
- Wessels, K. J., van den Bergh, F., & Scholes, R. J. (2012). Limits to detectability of land degradation by trend analysis of vegetation index data. *Remote Sensing of Environment*. <https://doi.org/10.1016/j.rse.2012.06.022>
- Wikipedia. (2020a). *Self-organizing map*. https://en.wikipedia.org/wiki/Self-organizing_map
- Wikipedia. (2020b). *Silhouette (clustering)*. [https://en.wikipedia.org/wiki/Silhouette_\(clustering\)](https://en.wikipedia.org/wiki/Silhouette_(clustering))
- Yan, L., & Roy, D. P. (2014). Remote Sensing of Environment Automated crop field extraction from multi-temporal Web Enabled Landsat Data. *Remote Sensing of Environment*, *144*, 42–64. <https://doi.org/10.1016/j.rse.2014.01.006>
- Zeileis, A. (2005). A unified approach to structural change tests based on ML scores, F statistics, and OLS residuals. *Econometric Reviews*, *24*(4), 445–466. <https://doi.org/10.1080/07474930500406053>
- Zeileis, A., Leisch, F., Hornik, K., & Kleiber, C. (2002). Strucchange: An R package for testing for structural change in linear regression models. *Journal of Statistical Software*, *7*, 1–38. <https://doi.org/10.18637/jss.v007.i02>

- Zewdie, W., Csaplovics, E., & Inostroza, L. (2017). Monitoring ecosystem dynamics in northwestern Ethiopia using NDVI and climate variables to assess long term trends in dryland vegetation variability. *Applied Geography*, 79, 167–178. <https://doi.org/10.1016/j.apgeog.2016.12.019>
- Zhao, H., & Chen, X. (2005). *Use of Normalized Difference Bareness Index in Quickly Mapping Bare Areas from TM / ETM +*. August. <https://doi.org/10.1109/IGARSS.2005.1526319>

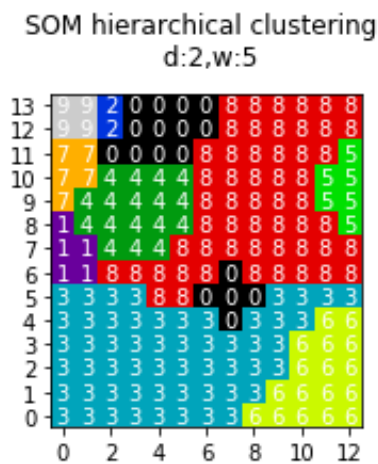
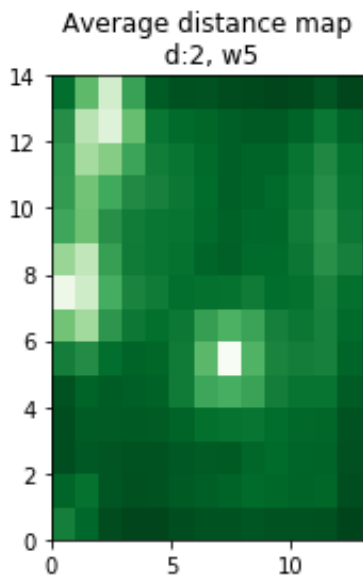
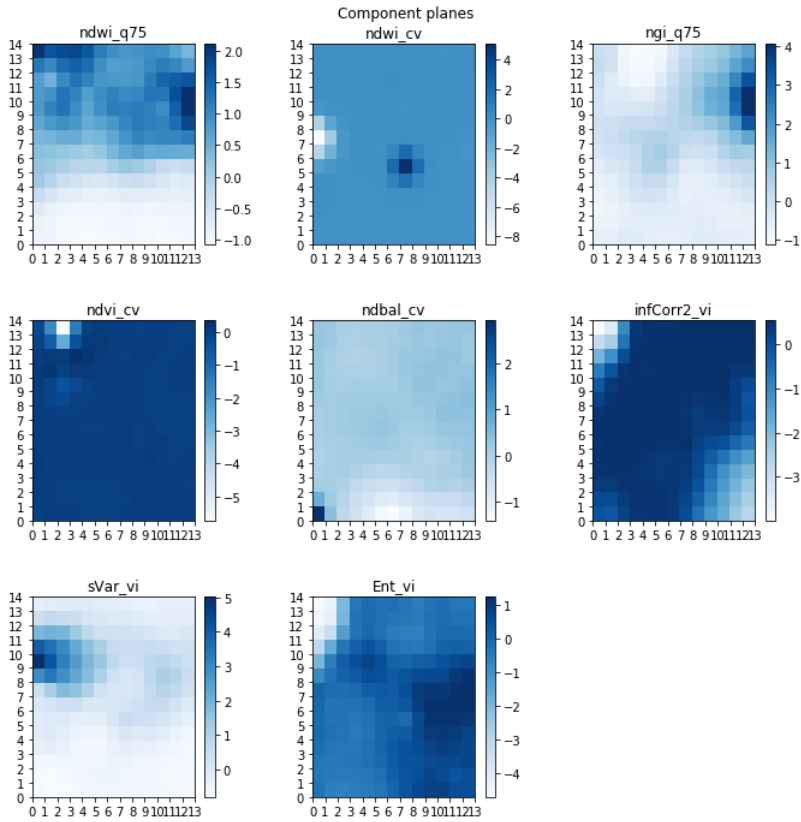
8 APPENDICES

Appendix A Type of NDVI trend shift experienced



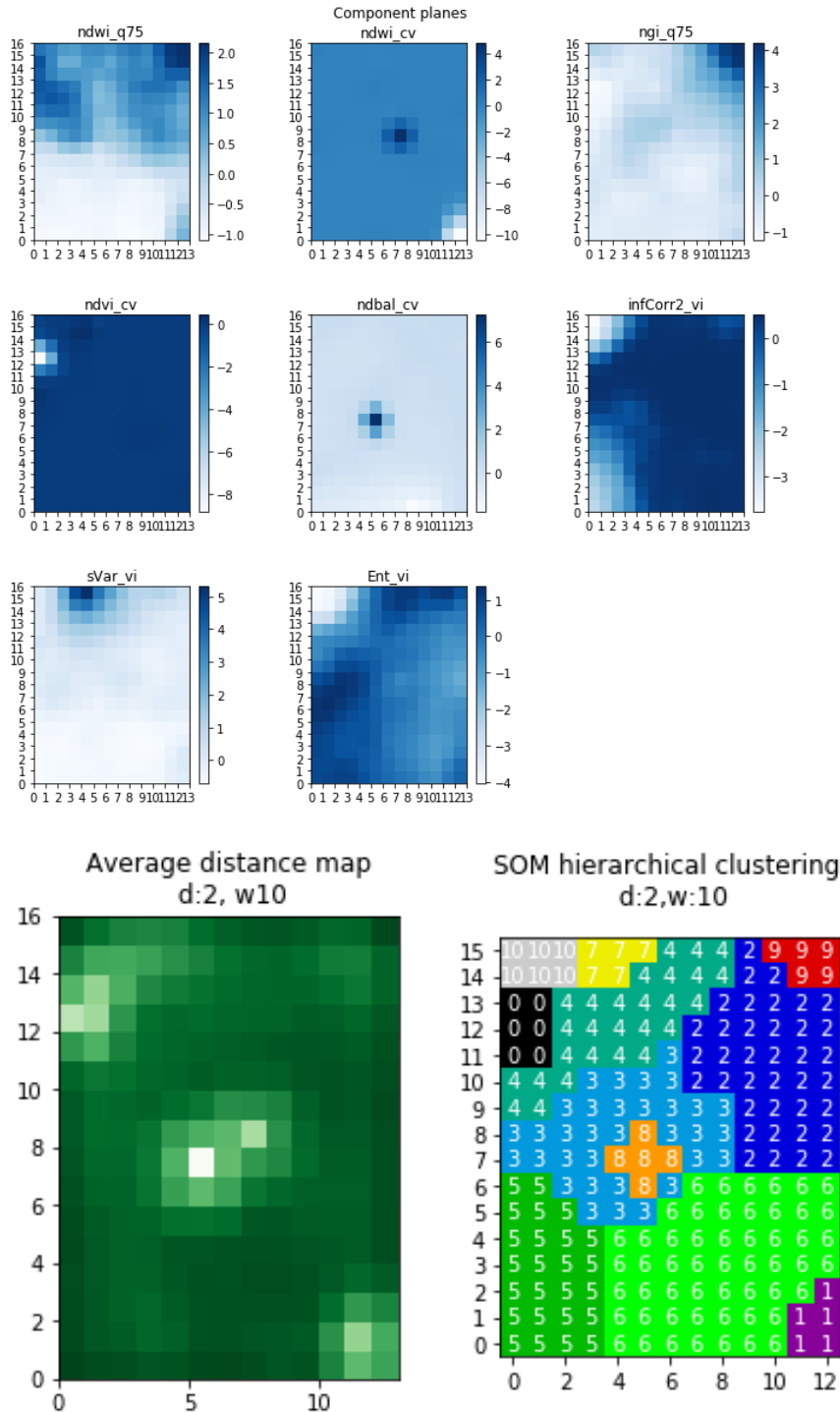
Appendix B Unsupervised classifiers: {d.= 0.2, wind.= 5x5, no shape metric}

B. 1 Component planes, distance map and clustered SOM



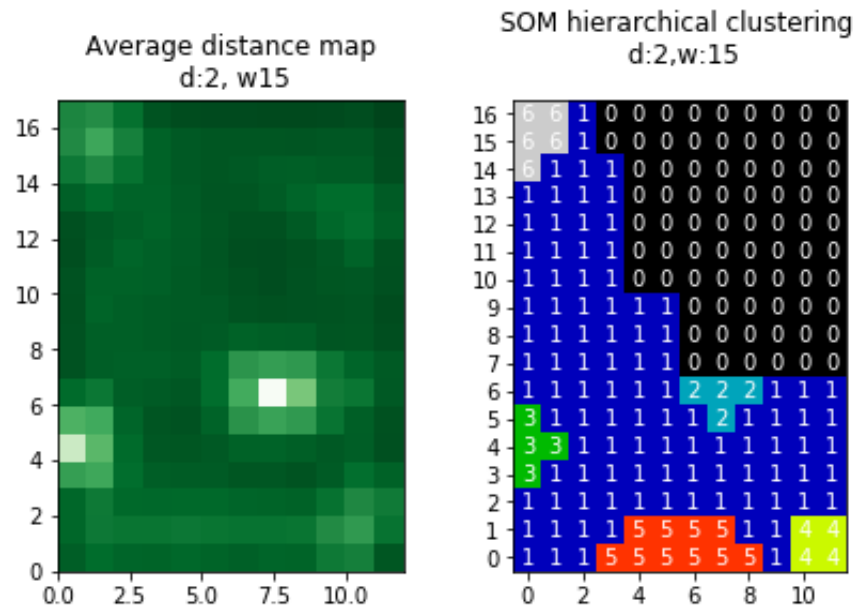
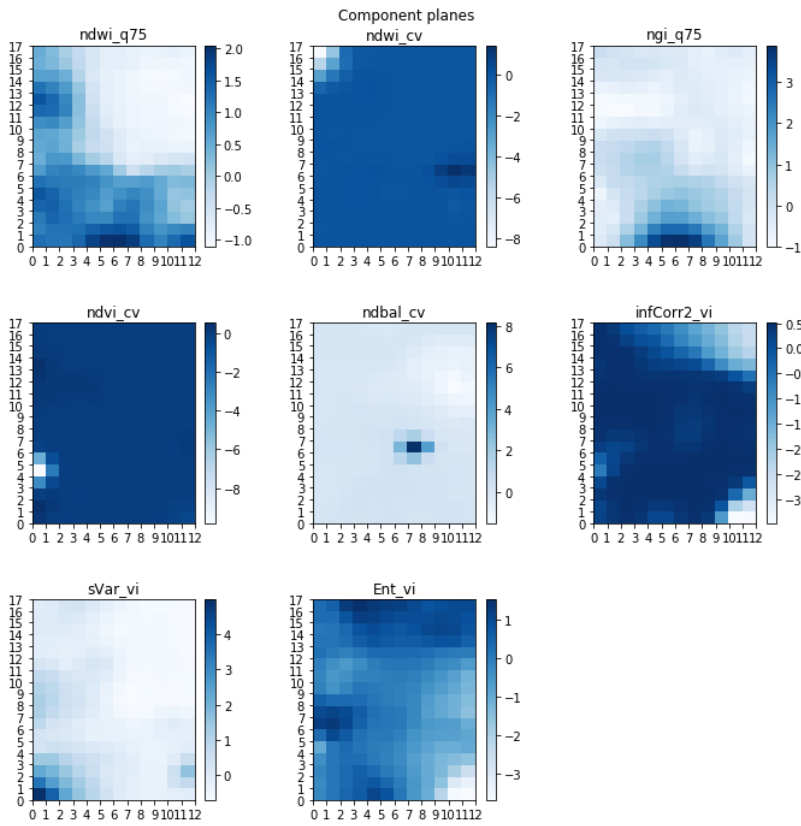
Appendix C Unsupervised classifiers: {d=0.2, wind.= 10x10, no shape metric}

C. 1 Component planes, distance map and clustered SOM



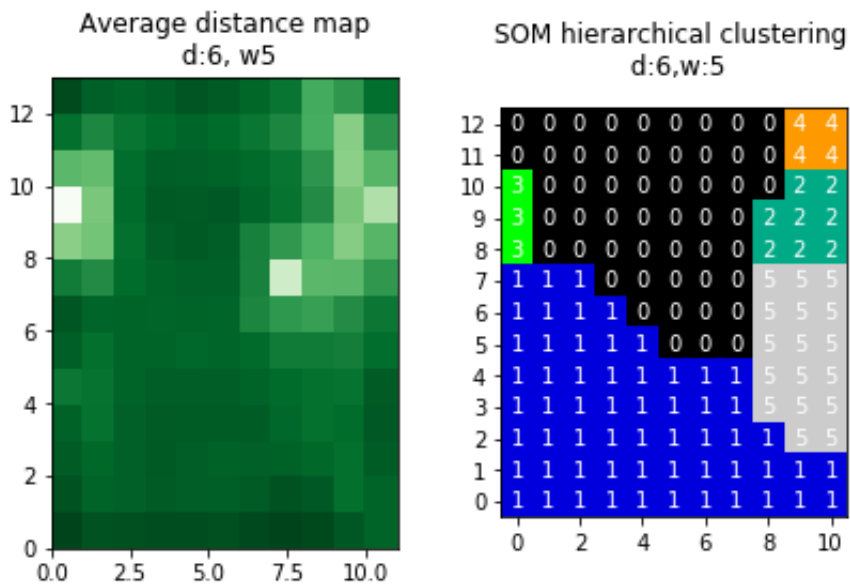
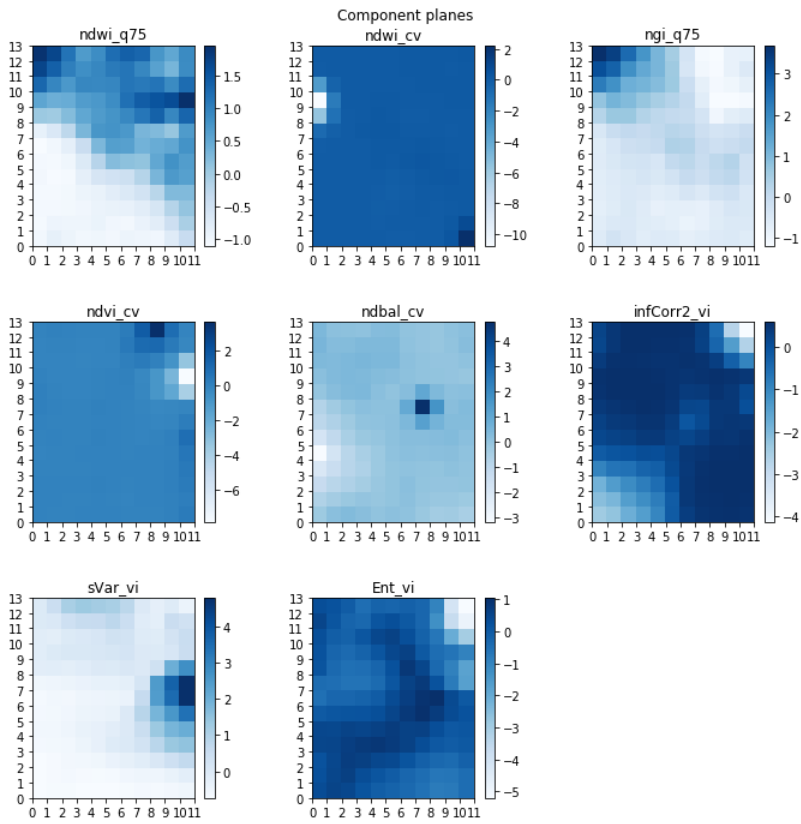
Appendix D Unsupervised classifiers: {dist.= 0.2, wind.= 15x15, no shape metric}

D. 1 Component planes, distance map and clustered SOM



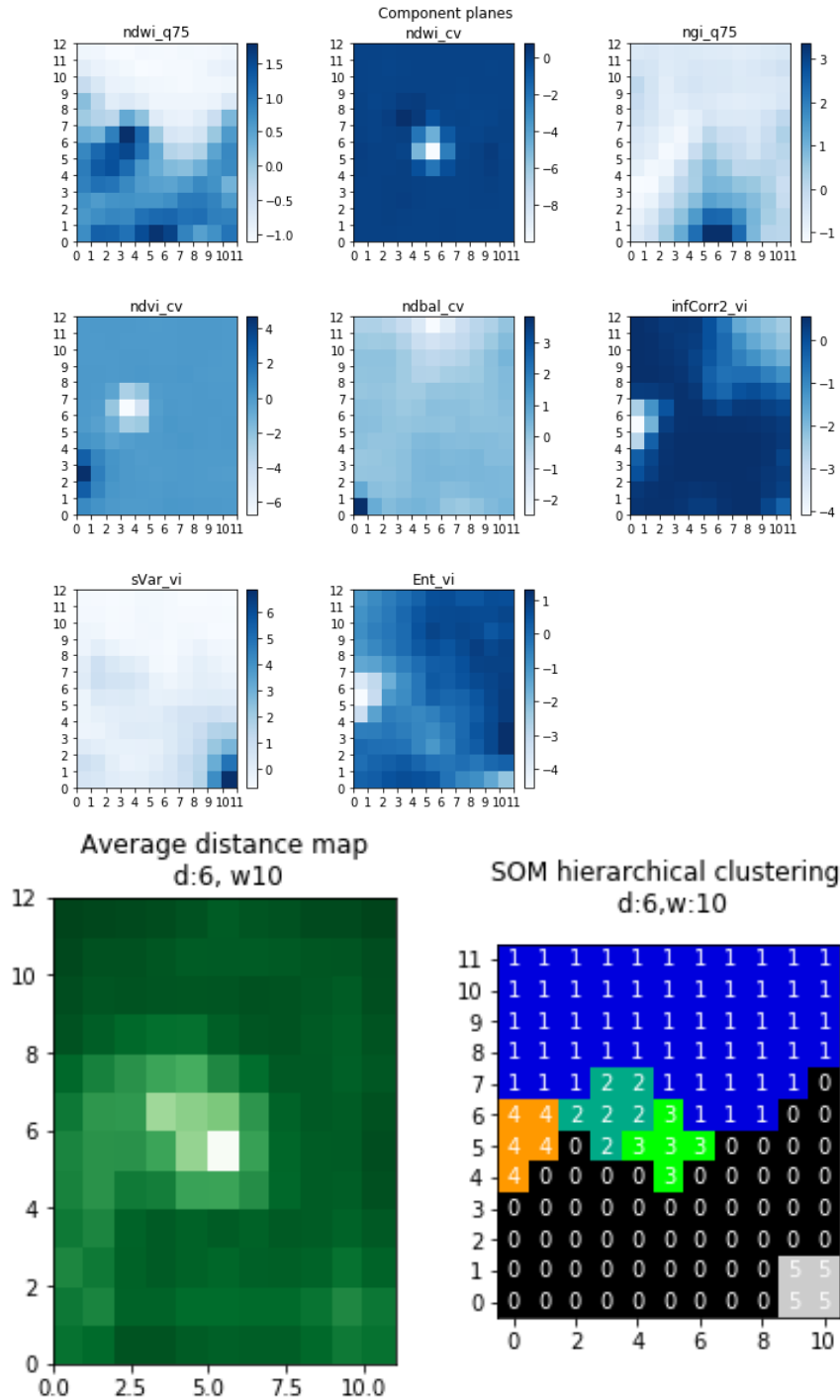
Appendix E Unsupervised classifiers: {d.=0.6, wind. =5x5, no shape metric}

E. 1 Component planes, distance map and clustered SOM



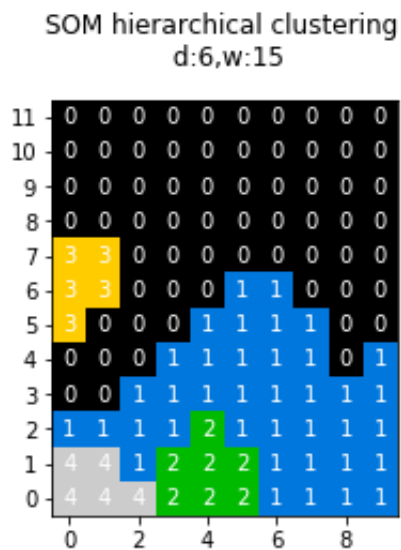
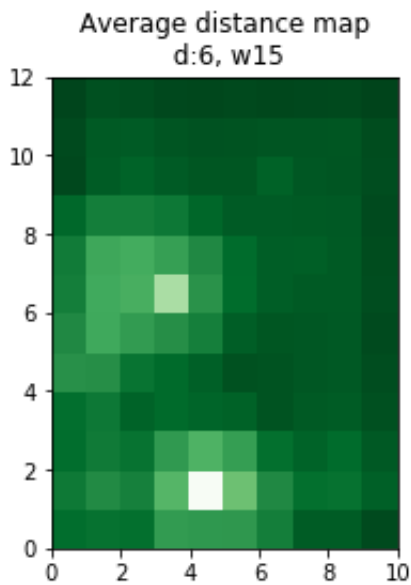
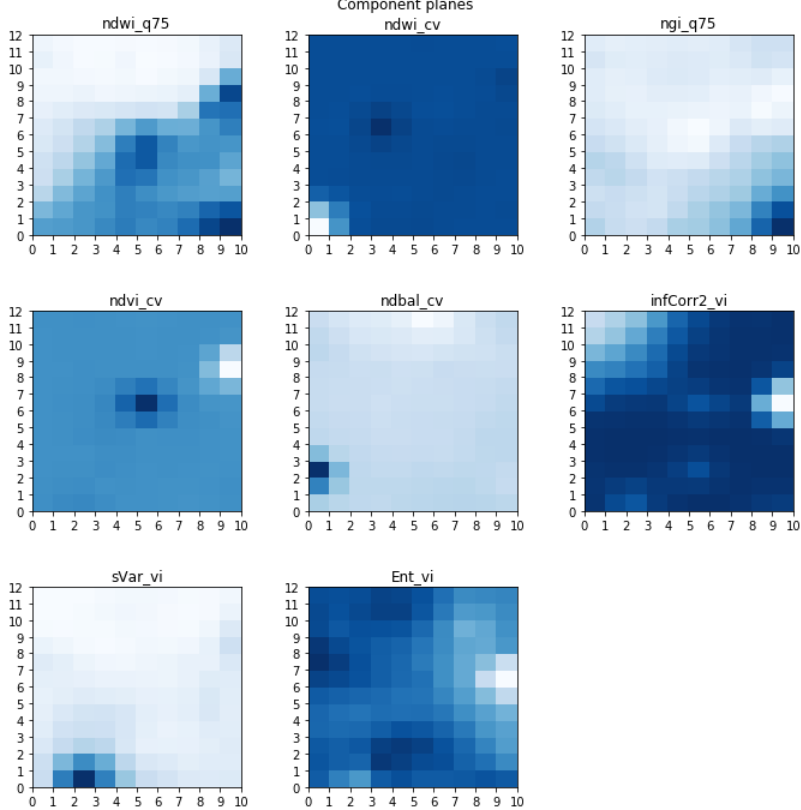
Appendix F Unsupervised classifiers: {dist.=0.6, wind. =10x10, no shape metric}

F. 1 Component planes, distance map and clustered SOM



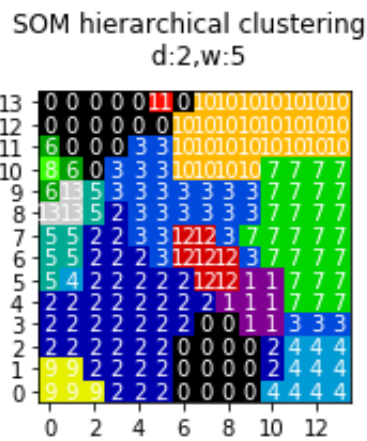
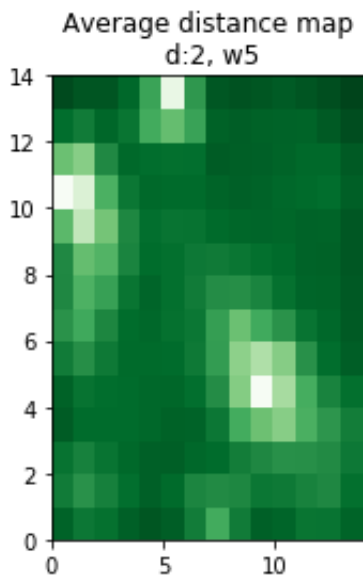
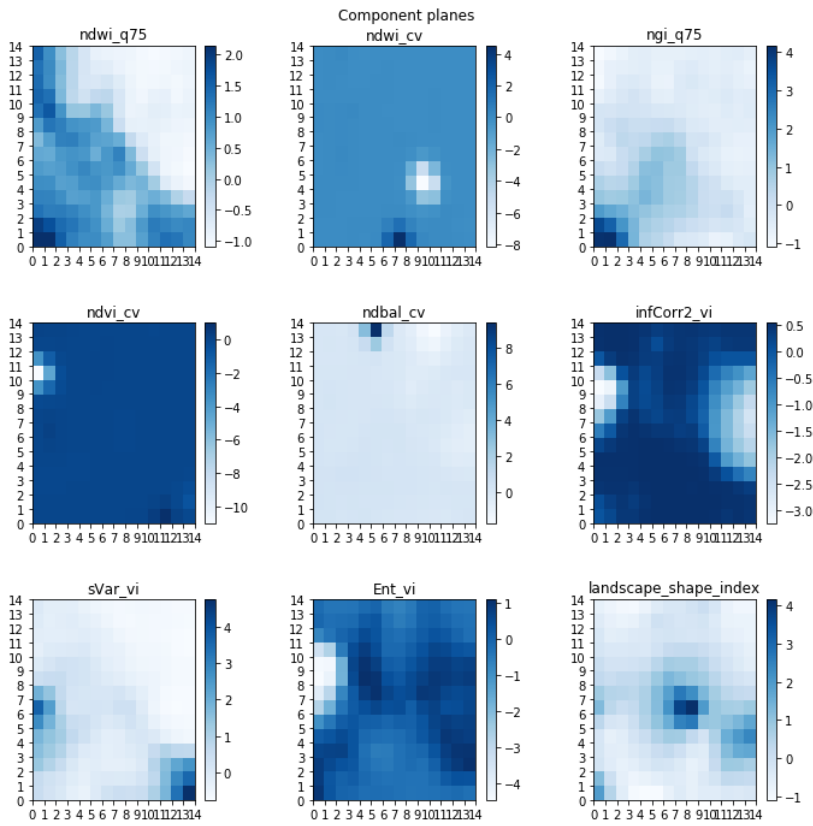
Appendix G Unsupervised classifiers: {d.=0.6, wind. =15x15, no shape metric}

G. 1 Component planes, distance map and clustered SOM



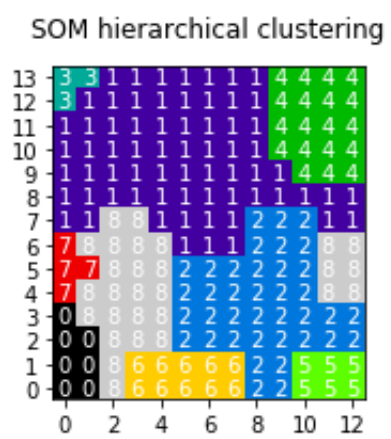
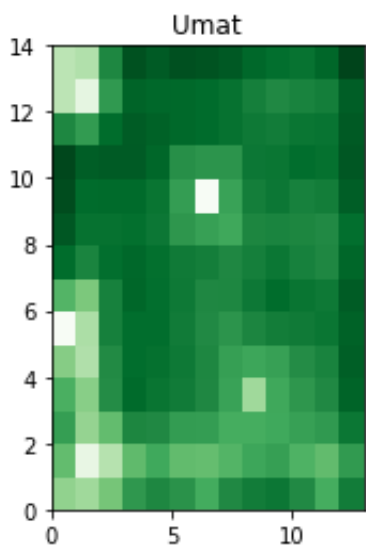
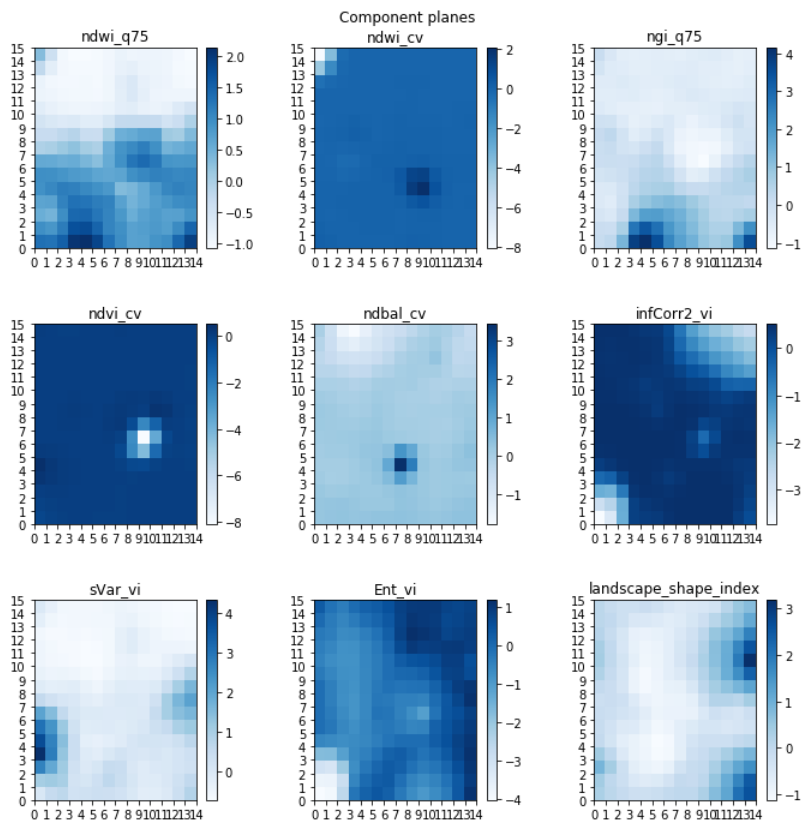
Appendix H Unsupervised classifiers: {d.=0.2, wind. =5x5, shape metric}

H. 1 Component planes, distance map and clustered SOM



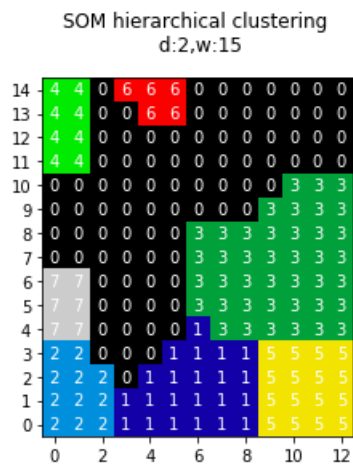
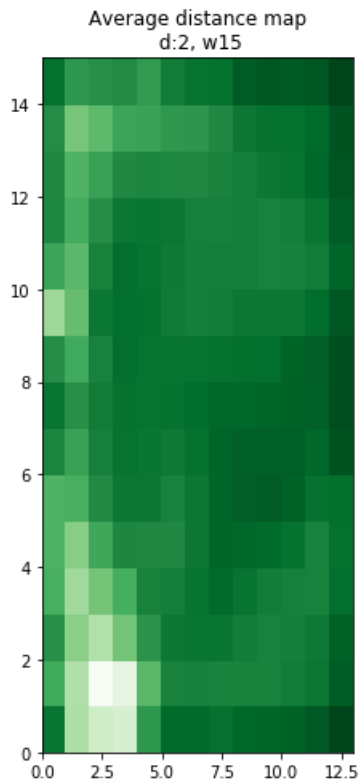
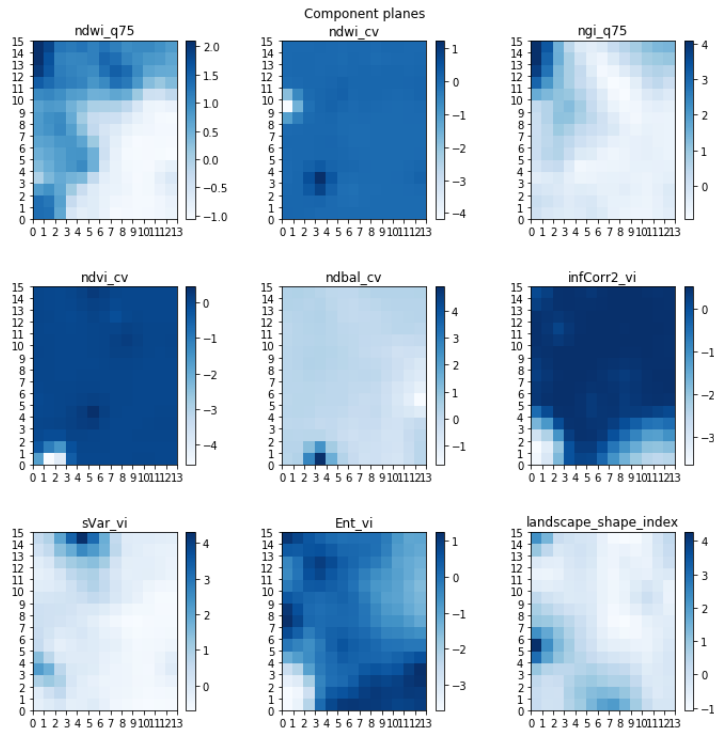
Appendix I Unsupervised classifiers: {d.=0.2, wind. =10x10, shape metric}

I. 1 Component planes, distance map and clustered SOM



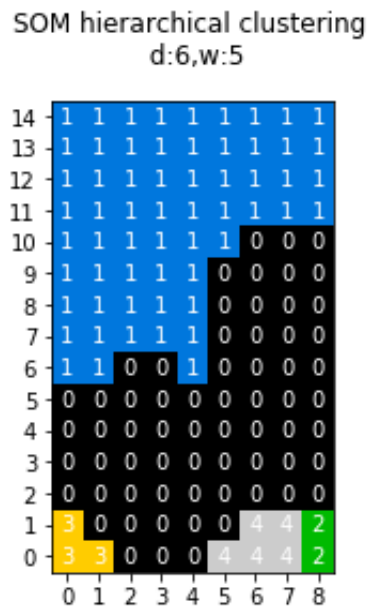
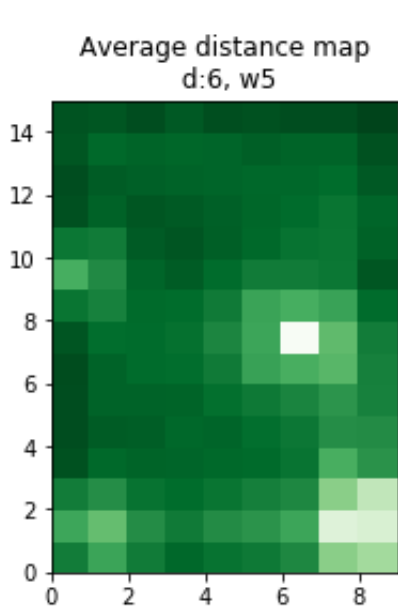
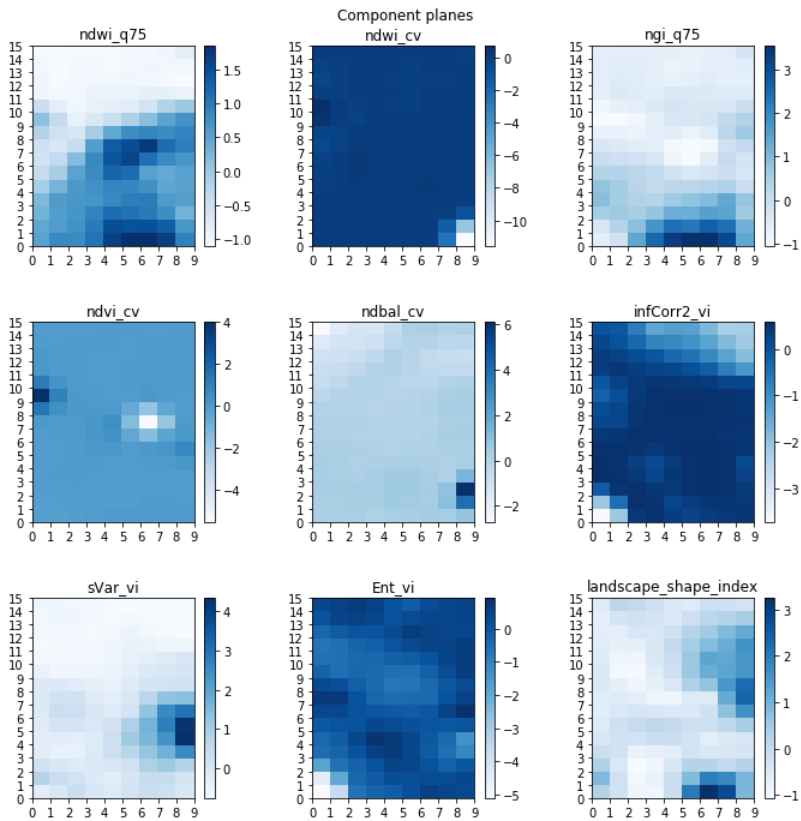
Appendix J Unsupervised classifiers: {d.=0.2, wind. =15x15, shape metric}

J. 1 Component planes, distance map and clustered SOM



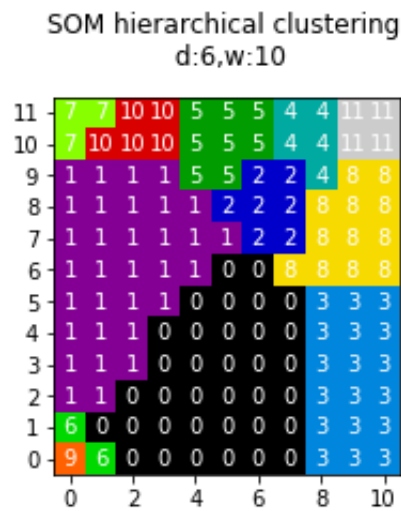
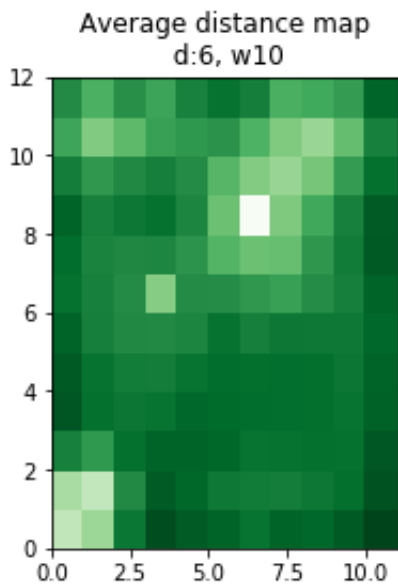
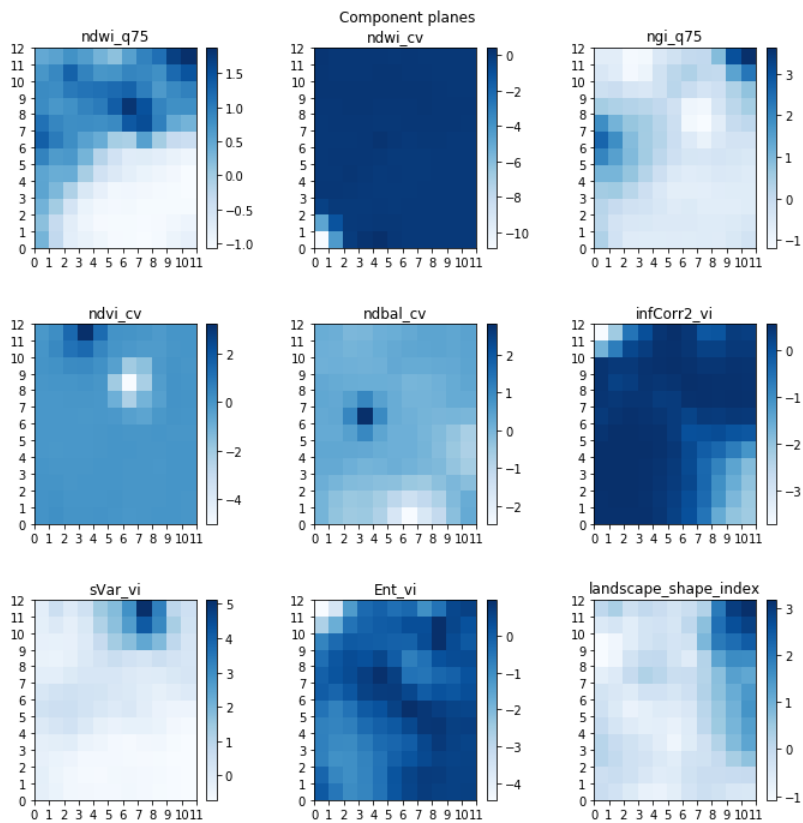
Appendix K Unsupervised classifiers: {d.=0.6, wind. =5x5, shape metric}

K. 1 Component planes, distance map and clustered SOM



Appendix L Unsupervised classifiers: {d.=0.6, wind.=10x10, shape metric}

L. 1 Component planes, distance map and clustered SOM



Appendix M Unsupervised classifiers: {d.=0.6, wind. =15x15, shape metric}

M. 1 Component planes, distance map and clustered SOM

